THE USE OF POLARIZED LIGHT FOR BIOMEDICAL APPLICATIONS

A Dissertation

by

JUSTIN SHEKWOGA BABA

Submitted to the Office of Graduate Studies of
Texas A&M University
in partial fulfillment of the requirements for the degree of

DOCTOR OF PHILOSOPHY

August 2003

Major Subject: Biomedical Engineering

THE USE OF POLARIZED LIGHT FOR BIOMEDICAL APPLICATIONS

A Dissertation

by

JUSTIN SHEKWOGA BABA

Submitted to Texas A&M University
in partial fulfillment of the requirements
for the degree of

DOCTOR OF PHILOSOPHY

Approved as to style and content by:

Gerard L. Cote´ (Chair of Committee)	Henry F. Taylor (Member)
Li Hong V. Wang (Member)	Charles S. Lessard (Member)
William A. Hyman (Head of Department)	

August 2003

Major Subject: Biomedical Engineering

ABSTRACT

The Use of Polarized Light for Biomedical Applications.

(August 2003)

Justin Shekwoga Baba, B.S., LeTourneau University

Chair of Advisory Committee: Dr. Gerard L. Coté

Polarized light has the ability to increase the specificity of the investigation of biomedical samples and is finding greater utilization in the fields of medical diagnostics, sensing, and measurement. In particular, this dissertation focuses on the application of polarized light to address a major obstacle in the development of an optical based polarimetric non-invasive glucose detector that has the potential to improve the quality of life and prolong the life expectancy of the millions of people afflicted with the disease diabetes mellitus. By achieving the mapping of the relative variations in rabbit corneal birefringence, it is hoped that the understanding of the results contained herein will facilitate the development of techniques to eliminate the effects of changing corneal birefringence on polarimetric glucose measurement through the aqueous humor of the eye.

This dissertation also focuses on the application of polarized light to address a major drawback of cardiovascular biomechanics research, which is the utilization of toxic chemicals to prepare samples for histological examination. To this end, a polarization microscopy image processing technique is applied to non-stained cardiovascular samples as a means to eliminate, for certain cardiac samples, the necessity for staining using toxic chemicals. The results from this work have the potential to encourage more investigators to join the field of cardiac biomechanics, which studies the remodeling processes responsible for cardiovascular diseases such as myocardial infarct (heart attacks) and congestive heart failure. Cardiovascular disease is epidemic, particularly amongst the population group older than 65 years, and the number of people affected by this disease is expected to increase appreciably as the baby boomer

generation transitions into this older, high risk population group. A better understanding of the responsible mechanisms for cardiac tissue remodeling will facilitate the development of better prevention and treatment regimens by improving the early detection and diagnosis of this disease.

DEDICATION

This work is dedicated to my parents Ruth and Panya Baba who instilled in me and in all of my siblings, a strong desire to always continue to learn and taught us the value of an education. You always said that your children's education was your second most important investment, second only to your investment in our eternal future. Thank you for making great personal sacrifices to make that a reality for me and for my siblings.

Well in your own words,
"Once acquired, no one can take away an education from you."
I hope you are right about this too. I have a strong sense that you are.

ACKNOWLEDGEMENTS

I would like to thank numerous people for their support and for making this work a reality. First, I would like to thank my advisor Dr. Cote who has been a friend, a colleague, and a mentor; I could not have asked for better. Then I would like to acknowledge the contributions of the members of my committee and Dr. Criscione for their constructive and useful comments, which have been incorporated into this dissertation. Secondly, I would like to thank my colleague and collaborator, Dr. Brent Cameron, who mentored me early on when I joined the Optical Biosensing Laboratory. In addition, I would like to thank my colleague Jung Rae-Chung for her help with the AMMPIS calibration and all of the members of OBSL during my tenure for their help in one form or the other. Thirdly, I would like to thank my family, friends, and church families for their constant prayers and support. I would not have made it through without you guys.

In particular, I would like to single out the following who have played a major role: George Andrews for relentlessly encouraging me to pursue a course of study in the basic sciences while I was still an undergraduate at LeTourneau: this is not quite basic science but it is about as close as applied science gets; Barry Sutton for making me critically evaluate my pursuit of an aviation career; Femi Ibitayo for encouraging biomedical engineering; Sam Weaver for teaching and demanding excellence in my engineering coursework; Anita Neeley for your constant encouragement and belief in my abilities and for the opportunities you provided for me to learn and to apply myself in service; Dr. Vincent Haby for recommending Texas A&M University; Peter Baba, Philip Baba, Vincent Dogo, Lois and Joshua Maikori, and Mom and Dad for your additional financial support; the Ibitayos, Brian and Candyce DeKruyff, Bill and Marilyn DeKruyff, Beth and Jason Daniels, the Maikoris who are now in GA, Adeyemi Adekunle, James Dixson, the Gibsons, my mother-in-law, Nancy Mathisrud, and her family, and the Cotés for opening up your home, feeding me, and providing a place for

me to occasionally hang out. Finally, I would like to thank my wife Carmen, for her love, continued support and patience with me through the constant deadlines that have been a staple of my graduate career in addition to the constant neglect that she has endured through the years as a result. Carmen, you now have your husband back.

TABLE OF CONTENTS

CHAPTER Page

CHAPTER Page

CHAPTER Page

Page

LIST OF FIGURES

FIGURE Page

FIGURE Page

FIGURE Page

LIST OF TABLES

TABLE Page

CHAPTER I
INTRODUCTION

The high cost and the widespread reach of diseases such as diabetes mellitus and cardiovascular disease is enormous. Hundreds of billions of dollars are spent annually in the US alone addressing these two health pandemics. Even more telling is the personal impact of these two diseases; few people are not somehow personally affected by at least one if not both of these two diseases. Much work is being done, in the case of diabetes mellitus, to help prevent or slow down the occurrence of secondary complications through the development of technologies that will make the monitoring of blood sugar levels a seamless procedure for diabetics.[1-22] On the other hand, recent technological advances in endoscopic procedures have improved the diagnostic, sensing and therapeutic options for people suffering from cardiovascular disease (CVD).[23-34] However for CVD, there are still many unknowns in terms of the mechanisms that result in events such as myocardial infarction, i.e. heart attack, which lead to congestive heart failure (CHF). The focus of this dissertation is the application of polarized light methods for these specific medical challenges.

1.1 Non-Invasive Glucose Detection

1.1.1 *An Overview of Diabetes Pathology*

Diabetes mellitus is a metabolic disorder that is characterized by the inability of the body to produce and or properly utilize insulin. This inability can cause both hyperglycemia: the prolonged elevation of blood glucose above the normal physiological level of 100mg/dl, or conversely hypoglycemia: the prolonged depreciation of blood glucose below the normal physiological level of 100mg/dl. In diabetics, these two conditions over time result in secondary complications. The secondary complications adversely

---

This dissertation follows the style and format of the Journal of Biomedical Optics.

impact the quality of life of a diabetic and are additionally fatal in most cases. There are two classes of diabetes based on whether or not there is a need for the patient to take supplemental insulin, namely, insulin-dependent diabetes (Type I diabetes) and non-insulin dependent diabetes (Type II diabetes) respectively. Type II diabetes can be hereditary and is typically developed by adults. Obesity is also a major factor in the development of Type II diabetes because it limits insulin effectiveness by decreasing the number of insulin receptors in the insulin target cells located throughout the body. Therefore, Type II diabetes, can be effectively managed by proper diet and exercise.[35-37]

1.1.2 *The Impact of Diabetes and the Current Monitoring Needs*

As of the year 2000, it was estimated that the disease diabetes mellitus afflicted over 120 million people worldwide. Of these, 11.1 million resided in the United States with an additional 6 million that were yet undiagnosed. In the U.S., this disorder, along with its associated complications, was ranked as the sixth leading cause of death based on 1999 death certificates; a huge human cost.[38] In terms of the monetary costs for diabetes, more recent US estimates for the year 2002 indicate a financial burden of over $132 billion for an estimated 12.1 million diagnosed diabetics.[39] Despite this increasing trend in the annual number of diagnosed diabetics, there is good news about their prospects for a normal quality of life. It has been known since the release of the findings in the NIH-Diabetes Control and Complications Trial in 1993[40] that the intensive management of blood sugars is an effective means to prevent or at least slow the progression of diabetic complications such as kidney failure, heart disease, gangrene, and blindness.[40,41] As such, self-monitoring of blood glucose is recommended for diabetic patients as the current standard of care.

However, the current methods for the self-monitoring of blood glucose require breaking the skin via a lancet or needle. Therefore, many patients find compliance with monitoring requirements difficult. The development of an optical polarimetric glucose sensor would potentially provide a means for diabetics to do this measurement non-invasively. If successful, the ability to non-invasively make measurements will hopefully

encourage patients to make more frequency assessments, thus, enabling them to achieve tighter control of blood glucose levels. Consequently, a tighter control of blood glucose will retard if not prevent the development of secondary complications, which are typically fatal.

1.1.3 *An Overview of Non-Invasive Polarimetric Glucose Measurement*

The first documented use of polarized light to determine sugar concentration dates back to the late 1800's where it was used for monitoring industrial sugar production processes.[42-44] Surprisingly, it has only been in the last two decades that the use of polarized light has been applied to the physiological measurement of glucose. This initiative began in the early 1980's when March and Rabinovich[45,46] proposed the application of this technique in the aqueous humor of the eye for the development of a non-invasive blood glucose sensor. Their idea was to use this approach to obtain aqueous humor glucose readings non-invasively as an alternative to the invasively acquired blood glucose readings. Their findings and those of prior work done by Pohjola[47] indicated that such a successful quantification of glucose concentration would correlate with actual blood glucose levels. During the same period, Gough[48] suggested that the confounding contributions of other optically active constituents in the aqueous humor would be a barrier for this technique to be viable. In the following decade, motion artifact coupled with corneal birefringence,[49,50] low signal-to-noise ratio,[51] and the potential time lag between blood and aqueous humor concentrations during rapid glucose changes[51] were also identified as problems yet to be overcome for this technique to be viable. Throughout the 1990's considerable research was conducted toward improving the stability and sensitivity of the polarimetric approach using various systems while addressing the issue of signal size and establishing the feasibility of predicting physiological glucose concentrations *in vitro*, even in the presence of optical confounders.[17,19,52-55]

To date, the issues that have been successfully addressed for this technique are the sensitivity and stability of the approach *in vitro*, the measurement of the average time

lag between blood and aqueous humor glucose levels in New Zealand White rabbits, and the confounding contributions of other chiral aqueous humor analytes *in vitro*. Consequently, this leaves one outstanding issue, namely motion artifact; specifically, how to compensate for the affect of changing corneal birefringence on the polarimetric signal. This work will present results that further the understanding of this last remaining obstacle for the development of a viable non-invasive polarimetric glucose detector for diabetics.

1.2 Non-Staining Polarization Histology of Cardiac Tissues

1.2.1 *An Overview of Cardiovascular Heart Failure Pathophysiology*

Heart failure is characterized by the inability of the heart to properly maintain adequate blood circulation to meet the metabolic needs of the body. Heart failure can develop rapidly due to myocardial infarction: this is referred to as acute heart failure, or it can develop slow and insidiously: this is termed chronic heart failure. The normal heart functions as an efficient pump that essentially pumps out all off the deoxygenated blood that flows into the inlet port: the right atrium, to the lungs for oxygenation through the output pumping port: the right ventricle, via the pulmonary vein then back to the oxygenated blood inlet port: the left atrium, through the pulmonary artery and back out to the tissues through the systemic output pumping port: the left ventricle. Chronic hear failure is characterized by the fluid congestion of tissues, which can be pulmonary edema due to the inability of the heart to pump out all of the blood that is returned to it from the lungs: i.e. left vetricular failure, thus, creating a fluid back up in the lungs or it can be peripheral edema due to lower limb retention of fluid as a result of the failure of the right ventricle which causes a back up of systemic blood flow from the vessels. Consequently, since chronic heart failure is characterized by tissue fluid congestion, hence, it is termed congestive heart failure (CHF).[35-37,56]

Cardiac pathophysiological events such as myocardial infarction initiate the cardiac remodeling process, by killing myocytes: the cells that make up the myocardium, which do not regenerate. The remodeling: elongation and hypertrophy of the remaining

myocytes, occurs in an attempt to maintain normal cardiac output. The initial remodeling process results in ventricular enlargement, which causes the slippage of myo-lamina planes: i.e. planes contianing aligned myocytes separated by collagen sheets; thus, eventually leading to a thining of the ventricular walls. This process significantly prempts the inception of CHF.[57,58]

1.2.2 *The Impact of Cardiovascular Heart Failure*

Currently about 5 million Americans suffer from congestive heart failure (CHF). In the year 2000, CHF accounted for 18.7 out of every 100,000 deaths.[59] In the US, it is estimated that annually CHF accounts for over 2 million outpatient visits and for a financial burden of over $10 billion: of which 75% is spent on patient hospitalization.[60] Since more than 75% of CHF patients in the US are older than 65 years,[36] this suggests that the increasingly aging population, due to the coming of age of the baby boomer generation, will create a crisis of sorts in terms of the increasing healthcare resource requirements and the increasing financial strain on the populace to address this growing medical need. As a result, there is an urgent need to better understand the processes that cause CHF so that more effective early prevention, detection, and treatment methods can be developed.

1.2.3 *A Look at the Current Emphasis on Studying Cardiac Remodeling Processes to Better Understand CHF*

The increasing health threat of CHF coupled with myocardial infarction has lead to much research geared toward understanding the biomechanics of the heart as it pertains to this disease.[61-63] Unfortunately, the limitations of current imaging technologies restrict the ability to study dynamic changes in cardiac tissue *in vivo* without sacrificing the subject in the process. As a result, much of the current understanding comes from post-cardiac-event biomechanical modeling of excised cardiac tissues using laboratory animal models, whereby mechano-biological measurements are taken and correlated to the experimentally induced CHF events. To this end, light and polarization microscopic

methods have been applied to stained cardiac tissues to image birefringent collagenous structures.[64,65]

In particular, one of the recent biomechanical objectives has been to measure, using light microscopy, the sheet angle of myo-lamina or cleavage planes,[66] as a means of characterizing the aberrant growth and remodeling processes[67-72] that are implicated in congestive heart failure. Currently, this procedure requires utilizing caustic chemicals to stain the tissue, which is a hindrance because it makes it difficult for the preferred mechanical stabilization method of plastic embedding for quantitative histology (paraffin embedding causes too much distortion of myofiber sheet angle) in addition to being a medical risk for investigators.[73] This dissertation presents an alternative, utilizing a polarization microscopy imaging method, which enables the determination of the sheet angle, β, of the cardiac cleavage planes, without requiring the use of caustic staining techniques. It also investigates the use of this method to provide sufficient contrast to enable the measurement of the muscle wall thickness of a non-stained cardiovascular vessel.

CHAPTER II
THEORY OF LIGHT MATTER INTERACTIONS: THE BASIS FOR LIGHT TISSUE INTERACTIONS

2.1 The Nature and Properties of Light

The duality of light: the fact that it exhibits both wave and particle nature, makes the study of light-matter interactions a complex pursuit. The particle nature of light, as put forth by Newton, explains light interactions at the macroscopic level, using geometric or ray optics, and accounts for phenomena such as shadow formation while the wave nature of light explains light interactions at the micro and sub-micro level and accounts for photon interference and diffraction phenomena.[74] In general, for studies that are primarily based on the propagation of light, Maxwell's equations: the wave representation of light, govern such investigations; while for the interaction of light with matter, which primarily involves the absorption and emission of light, the quantum theory governs such investigations.[75] In order to have a clearer understanding of the basis for the studies that are reported in the preceding sections, on the use of polarized light for biomedical applications, it will be essential to investigate both the wave and particle nature of light as it pertains to the measurements that will be necessary to enable the discrimination of the properties of matter that we are interested in.

2.2 An Overview of Light Matter Interactions

The interaction of light with matter depends primarily on the microscopic structural properties of matter. The quantity, arrangement, and interactions of electrons, nuclei, atoms, molecules, and other elementary particle constituents of matter determine these properties. In order to be able to extract all of the available information about the optical dielectric properties of matter, polarized light inputs are necessary. The reason for this is that the polarization of light has the measurable effect of increasing the discrimination ability of light interrogation of matter. This increased specificity is a direct consequence of the ordered and quantized behavior of the constituent elements of matter, and is best-

investigated using quantum mechanics. However, even a macroscopic level investigation of the effects of polarized light on matter can reveal the average information about structural bonds, electronic states, and electronic alignments, which determine the measurable optical dielectric properties of matter.

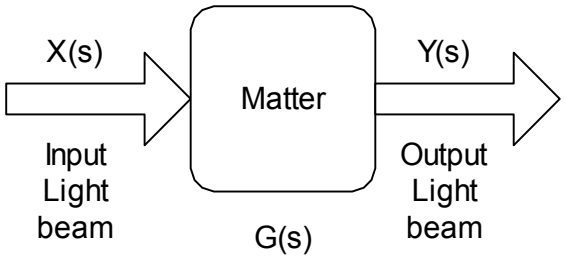

Figure 2.1: System diagram for the use of polarized light for determining the properties of matter.

Simply put, from Figure 2.1, we are interested in determining the transfer function, G(s), which contains all of the optical properties of matter, when we use polarized light inputs, X(s), to interrogate a sample of matter and measure the output effects, Y(s). The nature of the measured output response can be determined, to a degree, by using a classical approach to light matter interactions. The classical approach is limited to discerning only the optical dielectric properties of the sample and cannot account for all of the measurable output effects. All of the optical dielectric properties can be discerned from one measurable parameter of matter, the complex dielectric constant $\in$, which is proportional to the measured refractive index. A classic harmonic oscillator model will be used to investigate this approach by applying a wave model of light. In contrast, the quantum-mechanical approach, which can discern every measurable output effect, which includes the optical dielectric properties, will also be investigated. Finally, with an understanding of the underlying basis for the measurable output effects of matter, all of the optical dielectric properties, which are central to the various projects discussed in latter chapters, will be introduced.

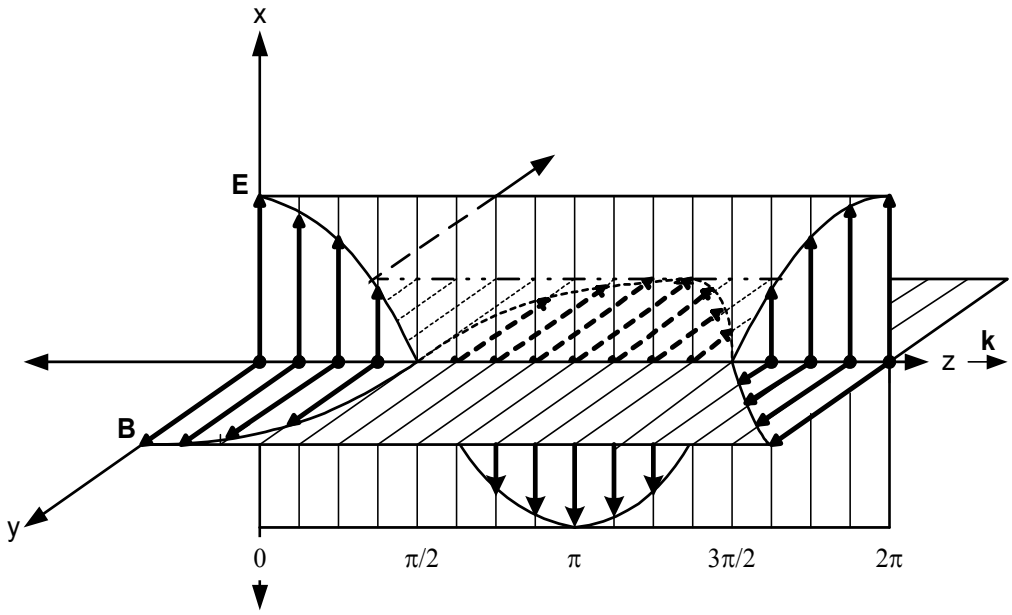

Figure 2.2: Depiction of a monochromatic electromagnetic wave propagating along the z-axis, k direction, with the electric field polarized in the x-direction and the magnetic field polarized in the y-direction.

2.3 Basic Electromagnetic (EM) Wave Theory

From Figure 2.2, the wave propagating along the z-axis, **k** vector, possessing a time varying electric field: with amplitude vibrations along the x-axis, **E**, and a time varying magnetic field with amplitude vibrations along the y-axis, **B**, can be represented by

$$\mathbf{E} = \hat{\boldsymbol{i}} E_x \cos(kz - \omega t) \text{ and } \mathbf{B} = \hat{\boldsymbol{j}} B_y \cos(kz - \omega t), \tag{2.1}$$

where E_x and B_y are scalars that represent the field amplitudes respectively. From Eqn. 2.1, the electric field has no components in the z and y directions, so

$$\frac{\partial \mathbf{E}}{\partial z} = \frac{\partial \mathbf{E}}{\partial y} = 0. \tag{2.2}$$

In addition, from Figure 2.2, as the electric field propagates along the z-axis, it is apparent that its magnitude for any given z-value is a constant. This means

$$\frac{\partial \mathbf{E}}{\partial x} = 0. \tag{2.3}$$

Now combining Eqns. 2.2 and 2.3 we get that the divergence of the propagating electric field is zero:

$$\nabla \bullet \mathbf{E} = \frac{\partial E_x}{\partial x} + \frac{\partial E_y}{\partial y} + \frac{\partial E_z}{\partial z} = 0, \tag{2.4}$$

which is Maxwell's equation for a propagating electric field in the absence of free charge and free current. Likewise, we get a similar result for the magnetic field, where the equation

$$\nabla \bullet \mathbf{B} = \frac{\partial B_x}{\partial x} + \frac{\partial B_y}{\partial y} + \frac{\partial B_z}{\partial z} = 0 \tag{2.5}$$

is Maxwell's equation for a propagating magnetic field in the absence of free charge and free current.

Equations 2.4 and 2.5 demonstrate that the propagating electromagnetic fields are space (position) invariant. Conversely, because electromagnetic waves are emitted from continuous sources in packets of discrete quanta, they are time variant.[76] Mathematically, this means that

$$\frac{\partial \mathrm{E}}{\partial t} \neq 0. \tag{2.6}$$

But a changing electric field generates a corresponding magnetic field and vice versa, which signifies that electromagnetic waves, once generated, are self-propagating. Mathematically this means:

$$c^2 \nabla \times \mathbf{B} = \frac{\partial \mathbf{E}}{\partial t} \Rightarrow \nabla \times \mathbf{B} = \mu_0 \in_0 \frac{\partial \mathbf{E}}{\partial t}$$

and

$$\nabla \times \mathbf{E} = -\frac{\partial \mathbf{B}}{\partial t}. \tag{2.7}$$

Expanding Eqn. 2.7 using vector algebra and substituting Eqns. 2.4 and 2.5 yields,

$$\nabla^2 \mathbf{E} = \mu_0 \in_0 \frac{\partial^2 \mathbf{E}}{\partial t^2} \text{ and } \nabla^2 \mathbf{B} = \mu_0 \in_0 \frac{\partial^2 \mathbf{B}}{\partial t^2}, \tag{2.8}$$

which are analogous to

$$\nabla^2 f = \frac{1}{\mathrm{v}^2}\frac{\partial^2 f}{\partial t^2}, \tag{2.9}$$

the wave equation; where *f* is a wavefunction propagating with a velocity v. Here μ_0 and $\in_0$ are the constants for permeability and permittivity of free space respectively. Thus the equations in Eqn. 2.8 indicate that electromagnetic waves travel through free space at the speed of light.[77]

2.4 Basic Electro- and Magneto-Statics

2.4.1 *Overview*

All matter consists of atoms, which are made up of charged particles. The net interaction of these charged particles with that of the incident electromagnetic radiation accounts for the complex refractive index that inherently contains all of a sample's dielectric properties. In essence, a sample's dielectric properties can be said to be the response of its constituent elementary particles to electromagnetic radiation within the visible frequency range. In order to establish this concept, an investigation of the electrostatic properties of matter will be conducted before delving into the intricate details of how matter responds to the time-varying electromagnetic fields of light waves.

2.4.2 *Basic Electro-Statics*

Matter is composed of atoms, which contain a positively charged nucleus surrounded by negatively charged electrons.[a] The charges contained within the constituent atoms interact based on Coulomb's law, which is

$$\mathbf{F} = \frac{1}{4\pi \in}\frac{|q \cdot Q|}{r^2}\hat{\boldsymbol{r}}, \tag{2.10}$$

---

[a] A Hydrogen atom possesses only one electron

where **F** is the force exerted on the test charge, q, by the point charge, Q, located at a distance, r, in the direction of the unit position vector, $\hat{\boldsymbol{r}}$ [b]: this is depicted in Figure 2.3.

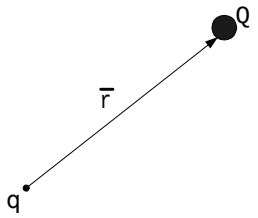

Figure 2.3: A depiction of the electrostatic force between a point charge, *q*, and a test charge, *Q*.

For multiple test charges Eqn. 2.10 becomes

$$\mathbf{F} = \mathbf{F}_1 + \mathbf{F}_2 + ... + \mathbf{F}_n = \frac{Q}{4\pi \in}\left(\frac{q_1}{r_1^2}\hat{\boldsymbol{r}}_1 + \frac{q_2}{r_2^2}\hat{\boldsymbol{r}}_2 + ... + \frac{q_n}{r_n^2}\hat{\boldsymbol{r}}_n\right), \tag{2.11}$$

where **F** is the net force exerted on the test charge, Q, by a collection of single point charges, $q_1, q_2, ..., q_n$, at the corresponding distances of $r_1, r_2, ..., r_n$, in the direction of the unit vectors $\hat{\boldsymbol{r}}_1, \hat{\boldsymbol{r}}_2, ..., \hat{\boldsymbol{r}}_n$. The net interaction force, generates an electric field, **E**, that acts along it.[c] This is possible because the affect of the test charge, q, is infinitesimally small such that the point charge, Q, does not move as a result of the generated force. Mathematically,

$$\mathbf{E} = \frac{\mathbf{F}}{q} = \frac{Q}{4\pi \in r^2}\hat{\boldsymbol{r}}, \tag{2.12}$$

for stationary charges. Analytically, Eqn. 2.12 means that the test charge, Q, possesses an electric field, **E**, that propagates radially and diminishes by the inverse square law. In

---

[b] Note that $\bar{\mathbf{r}} = r \cdot \hat{\boldsymbol{r}}$

[c] The electric field emanates at the negative charge and spreads radially outward

the Bohr model of the Hydrogen atom, the electric potential between the positively charged nucleus and the negatively charged electrons generates such an electric force which serves as a centripetal force that keeps the charged electrons revolving around the central nucleus at fixed radial distances called orbitals.

Since all matter consists of atoms, it follows that matter possesses inherent electrical properties. Though the atoms that make up matter are electrically neutral, their positively charged nuclei and negatively charged electrons can be influenced by a sufficiently strong external electric field. Under the influence of such an external field, the atomic charge distribution is realigned such that the positively charged nucleus is moved to the end closer to the incoming field while the negatively charged electrons are moved to the end further away. Therefore, the net result is that the external field, which is pulling the oppositely charged nucleus and electrons apart, and the electrostatic atomic field, which is pulling them together, attain equilibrium with a resulting change in the position of the nucleus and electrons. This new repositioning of the nucleus and the electrons is termed polarization. The atom, though still neutral, now possesses an induced electric dipole moment, $\boldsymbol{\mu}_{ind}$, which is aligned and proportional to the applied external electric field, **E**, that generated it. Essentially,

$$\boldsymbol{\mu}_{ind} = \alpha \mathbf{E}, \tag{2.13}$$

where α is a constant unique to the specific specie of atom called the atomic or molecular polarizability. In the situation where the sample of matter is composed of polar molecules which already possesses a dipole moment, the affect of the external field will be to create a torque on the molecule that realigns it with the field. Thus, for a given object, which consists of numerous aligned and polarized dipoles: whether atoms or molecules, the dipole moment per unit volume, **P**, is defined as

$$\mathbf{P} = \frac{\sum_{k=1}^{N} \boldsymbol{\mu}_{ind}}{V} = \frac{\sum_{k=1}^{N} \alpha \mathbf{E}}{V} = \frac{N \alpha \mathbf{E}}{V} = \in_0 \chi_e \mathbf{E}, \tag{2.14}$$

where N is the total number of atomic or molecular dipoles in the total volume, V, of the substance that possesses an electric susceptibility, χ_e; $\in_0$ is the permittivity of free space.

For linear materials, an applied external electric field, **E**, works with the already present dipole moment vector, **P**, to generate a net internal 'displacement' electric field within the object, **D**, which is related to the applied field by a constant, $\in$, that is based on the dielectric properties of the object. This is represented by:

$$\mathbf{D} = \in_0 \mathbf{E} + \mathbf{P} = \in_0 \mathbf{E} + \in_0 \chi_e \mathbf{E} = \in_0 (1 + \chi_e)\mathbf{E}$$
$$\therefore \mathbf{D} = \in \mathbf{E}, \tag{2.15}$$

where $\in \equiv \in_0 (1 + \chi_e)$ is the dielectric constant of the material.

2.4.3 *Basic Magneto-Statics*

In addition to rotating around the nucleus, electrons also spin around their axes, therefore, generating tiny magnetic fields. A moving: i.e. orbiting and or spinning, electron generates a current, which induces a corresponding magnetic field as described in Eqn. 2.7. For most matter in the natural state, the magnetic fields generated by the revolving and spinning electrons create magnetic dipole moments, **m**'s, that are canceling. They are canceling because the orbital dipole contributions are normally randomized and the spin dipole contributions are eliminated due to the orbital pairing of electrons with opposite spins in atoms possessing an even number of electrons: a direct result of the Pauli exclusion principle,[d] or by the randomizing local current variations that are due to thermal fluxes in atoms possessing an unpaired electron.

However, when an external magnetic field, **B**, is applied to matter, the constituent magnetic dipoles align themselves with the external field: anti-parallel to the applied field in the case of electron orbital generated dipoles (diamagnetism), and parallel to the applied field in the case of electron spin generated dipoles (paramagnetism), thus, creating an internal net magnetic displacement field, **H**. This displacement field arises from the magnetic polarization of the material due to an

---

[d] The Pauli exclusion principle is a postulate in quantum mechanics.

induced net magnetic dipole moment, $\mathbf{m}_{\text{ind}}$, which is dependent on the magnetic susceptibility, χ_m, of the material and is described by the following equations:

$$\mathbf{m}_{\text{ind}} = \chi_m \mathbf{H} \tag{2.16}$$

and

$$\mathbf{H} = \frac{1}{\mu_m}\mathbf{B} - \mathbf{M}, \tag{2.17}$$

where **M** and μ_m are the corresponding magnetic dipole moment per unit volume and the permeability of the specie.

For linear magnetic materials: paramagnetic and diamagnetic materials, once the external magnetic field, **B**, is removed, the magnetic dipole moment, **M**, disappears as the magnetic displacement vector, **H**, loses its source. From Eqn. 2.17, this means that

$$\mathbf{M} = \chi_m \mathbf{H}\,. \tag{2.18}$$

Furthermore, for $\mu_m = \mu_0(1+\chi_m)$, where μ_0 is the permeability of free space, Eqn. 2.17 becomes

$$\begin{aligned} &\mathbf{B} = \mu_0(\mathbf{H}+\mathbf{M}) = \mu_0(1+\chi_m)\mathbf{H} \\ &\therefore \mathbf{B} = \mu_m \mathbf{H}. \end{aligned} \tag{2.19}$$

This establishes that the external magnetic field is directly proportional to the internal magnetic field that it induces in the material.

Likewise, as in the case of the relationship established for the electric dipole moment in Eqn. 2.14, the magnetic dipole moment, **M**, is similarly related to the induced magnetic dipole moment, $\mathbf{m}_{\text{ind}}$, by the following expression

$$\mathbf{M} = \frac{\sum_{k=1}^{\mathrm{N}} \mathbf{m}_{ind}}{\mathrm{V}} = N \cdot \mathbf{m}_{ind}\,, \tag{2.20}$$

where N represents the total number of atomic or molecular dipoles in the material, and for a unit volume, V; N =N/V.

2.4.4 *The Classic Simple Harmonic Oscillator: A Macroscopic Model for the Complex Refractive Index*

From the discussion of electro- and magneto-statics in the previous two subsections, two intrinsic, but macroscopic, dimensionless electromagnetic parameters were introduced, which determine the polarizability of matter: namely, the dielectric constant, $\in$, and the magnetic susceptibility, χ_m. In this section, the classic harmonic oscillator model will be used to investigate the frequency dependence of these two parameters and, thus, elucidate how the dielectric properties of matter can be extracted from them, albeit, without an actual understanding of the underlying quantum-mechanical mechanisms that determine the actual light tissue interactions.

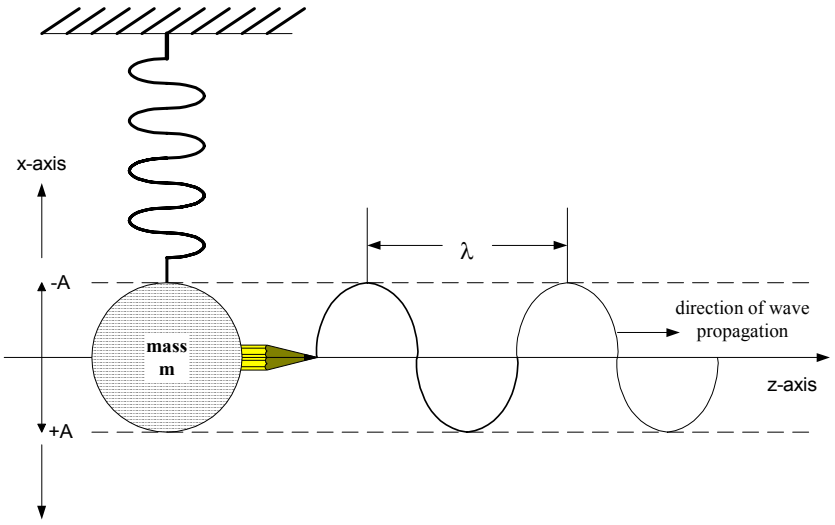

Figure 2.4: The depiction of the classic harmonic oscillator of a mass suspended by a spring.

In the classic harmonic oscillator, Figure 2.4, a suspended mass, m, oscillates along the x-axis generating a sinusoidal wave, of amplitude, A, which propagates along the z-axis with a wavelength, λ. For this investigation, we can consider the mass, m, to be an electron bond to the nucleus with a binding force, $\mathbf{F}_{\text{bind}}$ of magnitude F_{bind} in the x-

direction that is represented by the spring of force constant k that oscillates about its equilibrium position by an amount $\pm x$. Then from Newton's second law, we get

$$F_{\text{bind}} = -kx = m\frac{d^2x}{dt^2}, \tag{2.21}$$

where $\frac{d^2x}{dt^2}$ is the acceleration in the x-direction. Solving Eqn. 2.21, yields

$$x(t) = A\sin\left(\sqrt{\frac{k}{m}}\cdot t\right) \text{ based on } x = 0 \text{ for } t = 0. \tag{2.22}$$

Substituting Eqn. 2.21 into 2.22, we get

$$F_{\text{bind}} = -kx = -m\omega_0{}^2 x, \tag{2.23}$$

where $\omega_0 = \sqrt{\frac{k}{m}}$ is the natural oscillation frequency of the electron, $x(t) = A\sin(\omega_0 \cdot t)$, and $\frac{d^2x}{dt^2} = -A\omega_0{}^2\sin(\omega_0 t)$. Over time, the electron returns back to equilibrium due to a damping force, $\mathbf{F}_{\text{damp}}$ of magnitude F_{damp} that acts to oppose the displacement in the x-direction. This damping force is represented by

$$F_{\text{damp}} = -m\xi\frac{dx}{dt}, \tag{2.24}$$

where ξ is the opposing velocity generated by the damping force.

When the bond electron is introduced to an EM wave, with the E-field polarized in the x-direction, it is subjected to a sinusoidal driving force, $\mathbf{F}_{\text{drive}}$ of magnitude F_{drive} given by

$$F_{\text{drive}} = qE = qE_x\cos(\omega\cdot t), \tag{2.25}$$

where q represents the charge of the electron, E_x represents the magnitude of the x-component of the electric field, propagating with a radian frequency ω, at the electron location. Combing Eqns. 2.23, 2.24, and 2.25 using Newton's second law, yields

$$\begin{aligned} & m\frac{d^2x}{dt^2} = F_{bind} + F_{damp} + F_{drive} \\ & \Rightarrow m\frac{d^2x}{dt^2} + m\xi\frac{dx}{dt} + m\omega_0{}^2 x = qE_x\cos(\omega\cdot t). \end{aligned} \tag{2.26}$$

Rearranging Eqn. 2.26 and using exponential notation to represent the sinusoidal driving force, leads to

$$\frac{d^2x'}{dt^2} + \xi\frac{dx'}{dt} + \omega_0{}^2 x' = \frac{q}{m}E_x e^{-i\omega\cdot t}, \tag{2.27}$$

where ′ notation indicates a complex variable.

Now, considering the steady state condition of the electron, which will vibrate at the frequency of the driving field:

$$x'(t) = x'_0 e^{-i\omega\cdot t}, \tag{2.28}$$

and substituting Eqn. 2.28 into 2.27, leads to

$$x'_0 = \frac{q/m}{\omega_0{}^2 - \omega^2 - i\xi\omega}E_x. \tag{2.29}$$

Recalling Eqn. 2.13, this implies that

$$\mu'_{ind} = q\cdot x'_0(t) = \frac{q^2/m}{\omega_0{}^2 - \omega^2 - i\xi\omega}E_x e^{-i\omega\cdot t} \tag{2.30}$$

where the real part of μ'_{ind} is the magnitude of the dipole moment and the imaginary part contains information about the phase relationship between the driving electric field and the dipole response of the electron. The phase is computed using $\tan^{-1}$[Im/Re]. Given a sample of material with N molecules per unit volume that is made up of n_j electrons per molecule possessing their own unique natural frequencies, ω_j and damping coefficients, ξ_j, then the net $\boldsymbol{\mu}'_{\text{ind}}$ is given by:

$$\boldsymbol{\mu}'_{ind} = \frac{Nq^2}{m}\left(\sum_j \frac{n_j}{\omega_j{}^2 - \omega^2 - i\xi_j\omega}\right)\mathbf{E}'. \tag{2.31}$$

Recalling Eqns. 2.14, 2.15, and 2.30, we get the following relationships for the complex dielectric constant, $\in'$:

$$\boldsymbol{\mu}'_{\text{ind}} = \in_0 \chi'_e \mathbf{E}', \text{ and } \in' \equiv \in_0 (1+\chi'_e)$$
$$\Rightarrow \in' \equiv \left[1 + \frac{Nq^2}{m \in_0}\left(\sum_j \frac{n_j}{\omega_j{}^2 - \omega^2 - i\xi_j\omega}\right)\right]. \tag{2.32}$$

Similarly, we can derive the relationships for the complex magnet dipole moment, but since the electric force exerted by incident photons are much much greater than the magnetic force, making it insignificant, henceforth, the magnetic dipole moment will be ignored.

Based on the introduction of a complex dielectric constant, Eqn. 2.32, which describes the electric field, now becomes dispersive: i.e. it expresses wavelength dependence, yielding:

$$\nabla^2 \mathbf{E}' = \in' \mu_0 \frac{\partial^2 \mathbf{E}'}{\partial t^2} \tag{2.33}$$

that possesses a solution of the form:

$$\mathbf{E}' = \mathbf{E}'_0 e^{i(k'z - \omega t)}, \tag{2.34}$$

where k' is the complex wave number given by: $k' \equiv \omega\sqrt{\in' \mu_0} = k + i\kappa$; here the wave number is k=2π/λ and κ is the corresponding wave propagation attenuation factor. Now substituting for k', gives

$$\mathbf{E}' = E'_0 e^{-\kappa \cdot z} e^{i(k'z - \omega t)}. \tag{2.35}$$

By definition, the refractive index is the speed of light in a medium relative to that in a vacuum. Recalling that

$$\eta(\omega) = \frac{c}{\text{v}} = \sqrt{\frac{\in' \mu_m}{\in_0 \mu_0}} \cong \sqrt{\in'} : \text{since } \mu_m \cong \mu_0 \text{ for most materials,}$$

where v and c are the velocities of light in a medium and in a vacuum respectively,

$$\Rightarrow \eta^2(\omega) \cong \in' = \left[1 + \frac{Nq^2}{m \in_0}\left(\sum_j \frac{n_k}{\omega_j{}^2 - \omega^2 - i\xi_j\omega}\right)\right]. \tag{2.36}$$

Given that the absorption coefficient of a medium, α, is related to the wave attenuation factor by

$$\alpha \equiv 2\kappa, \tag{2.37}$$

the refractive index, η, from Eqn. 2.36, and the absorption coefficient, α, are plotted in Figure 2.5.

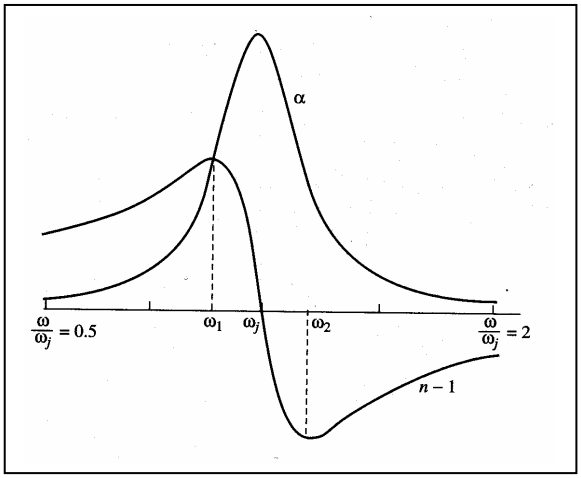

Figure 2.5: Plot of the magnitude and phase of molecular polarizability in the absorption (anomalous dispersion) region of the molecule.[e]

From Figure 2.5, the peak in the absorption curve, i.e. magnitude of α, corresponds to the zero point crossing of the refractive index component. This phenomena is termed anomalous dispersion,[f] because, typically, the refractive index varies slightly without a complete reversal from $\pm$ to $\mp$. The exception, as depicted in the figure, occurs only in the vicinity of a resonant frequency, i.e. when $\omega = \omega_0$. At resonant frequency, the driving source energy is dissipated by the damping force counteracting the electron vibrating at or near its maximum restorable amplitude: a heat generating process. Due to the dissipation of energy, it follows, therefore, that matter is opaque in the region of anomalous dispersion. Consequently, normal dispersion occurs in the regions outside the vicinity of an absorption band.

---

[e] David J. Griffiths, reference 77, Figure 9.22.
[f] Also known as the "Cotton effect" for the complete reversal in the refractive index.

From Eqn. 2.36, the damping effect is negligible in the region of normal dispersion. Using the 1st term of the binomial expansion of Eqn. 2.32, which assumes the 2nd term is very small, Eqn 2.36 becomes

$$\eta(\omega) \cong \sqrt{\epsilon'} = \left[1 + \frac{Nq^2}{2m \in_0} \left(\sum_j \frac{n_j}{\omega_j{}^2 - \omega^2} \right) \right], \tag{2.38}$$

which yields

$$\begin{aligned} \eta(\omega) &\cong 1 + \left(\frac{Nq^2}{2m \in_0} \sum_j \frac{n_j}{\omega_j{}^2} \right) + \omega^2 \left(\frac{Nq^2}{2m \in_0} \sum_j \frac{n_j}{\omega_j{}^2} \right) \\ &\Rightarrow \eta = 1 + A\left(1 + \frac{B}{\lambda^2} \right), \text{where } \lambda = 2\pi \cdot \mathrm{c}/\omega, \end{aligned} \tag{2.39}$$ [g]

i.e. when accounting for the UV absorption bands of most transparent materials, implying that $\omega < \omega_0$, and thus,

$$\frac{1}{\omega_j{}^2 - \omega^2} = \frac{1}{\omega_j{}^2} \left(1 - \frac{\omega^2}{\omega_j{}^2} \right)^{-1} \cong \frac{1}{\omega_j{}^2} \left(1 + \frac{\omega^2}{\omega_j{}^2} \right). \tag{2.40}$$

2.4.5 *Concluding Remarks on the Complex Refractive Index*

It is evident from the use of the classic harmonic oscillator to model electronic oscillations that a requirement for light matter interactions is that the polarization of the incident beam be aligned with the axis of the molecular oscillations. Essentially, considering the electric field vector, only the portion of incident EM radiation that is aligned with the molecular oscillations: the dot product of the E-vector with the molecular oscillation unit vector; will interact. This physical requirement suggests that utilizing multiple input polarization states to interrogate a sample will reveal molecular structural information, albeit gross. Therefore, the aforementioned processes is the underlying basis for the application of polarized light to probe matter for the purpose of

---

[g] This is known as Cauchy's formula, with A=coefficient of refraction and B=coefficient of dispersion.

revealing various anisotropies that are based on the structural and molecular arrangements in a representative sample.

Using the complex refractive index, information about the average absorption and the average phase relationship between the natural harmonic oscillations of the elementary constituents of matter and a driving EM-light wave can be extracted. Consequently, this establishes that the refractive index contains information about the gross molecular structure of a material, which is represented by the complex dielectric constant. In summary, at the microscopic level, the complex refractive index is an integration of all of the molecular light tissue interactions, thus revealing the absorption and phase anisotropic properties that will be discussed in the later sections of this chapter.

2.5 Basic Quantum Mechanics

2.5.1 *Overview*

The quantum theory is a modified particle theory of light put forth by Einstein, Planck, and others that deals with elementary light particles called photons. The quantum theory addresses phenomena like blackbody radiation, the Compton effect, and photoelectric effect, among others: these are not explainable by the wave theory of light;[74] such processes are best modeled by quantized, packets, of energy called photons.

Though the dual application of the wave and particle natures of light to explain physical phenomena still appears to be a quandary, de Broglie resolved this issue long ago, when he postulated that light exhibits both properties always but its apparent nature is determined by the constituents of matter that it interacts with. An analysis of the physical dimensions of the objects that produce the measured spectroscopic signals for the investigations addressed in this dissertation indicate that the wavelength of light is orders of magnitude larger than the objects of interaction, as summarized in Table 2.1. From Table 2.1, the size disparity between the wavelengths of the probing light beam and the interaction particles is evident. The great size disparity enables the use of a plane wave propagation theory where the incident electric field appears to arrive in planes of

equal phase, perpendicular to the direction of light propagation, that vary in amplitude, spatially, as sinusoidal functions of time with rates corresponding to the light frequency.[74,78] It also makes it possible to apply the classic wave theory of light to explain absorption and emission processes, which are quantum-mechanical atomic and electronic processes, without accounting for changes in state due to spontaneous emission.[74] Furthermore the sinusoidal wave representation lends itself to the power expansion of the probing EM radiation, thereby, enabling an analysis of the contributions of various field components to the measured interactions.[74]

Table 2.1: An overview of the dimensions of UV-VIS light as compared to the size of the light interaction constituents of matter.[h]

TRANSITION	SIZE OF ABSORBER [nm]	RADIATION SOURCE	WAVELENGTH OF LIGHT [nm]
Molecular vibration	~1	IR	~1000
Molecular electronic	~1	VIS, UV	~100

2.5.2 *Quantum Mechanical Formulations*

In classical physics, matter is treated as being composed of harmonic oscillators, therefore, all light matter interactions are explained as wave phenomena. The absorption and emission of light by matter are based primarily on the interactions, at the atomic and molecular level, between valence electrons and the photons that make up the light wave. Planck discovered, based on classic harmonic oscillators, that the physical harmonic oscillators (electrons, atoms, molecules, etc.) all absorb and emit light in discrete amounts governed by the following relationship.[79]

$$E = h\nu, \tag{2.41}$$

[h] Adopted from David S. Kilger, et al., reference 74, Table 1-1.

where E is the quantized energy [J], h is Planck's constant[i] [J·s], and v is the harmonic oscillator frequency [s^{-1}]. Figure 2.6 illustrates the allowed energy states of an electron, which are integer multiples of the lowest, i.e. ground, energy state.

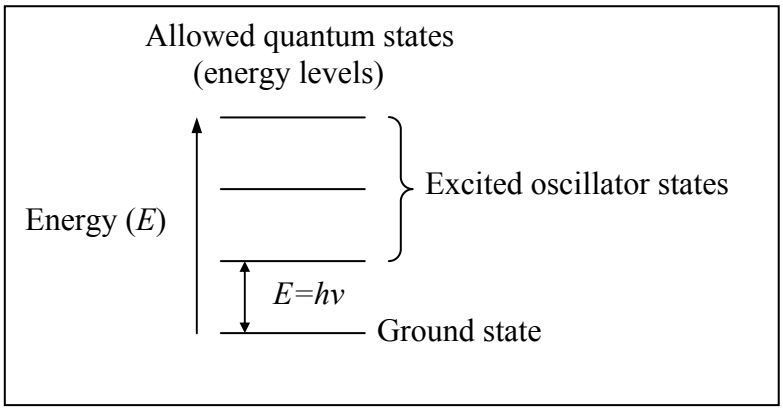

Figure 2.6: Energy diagram depicting the quantized energy levels for a harmonic oscillator.[j]

Building on this concept, Bohr proposed that the ability of electrons to absorb and emit (scatter) photons is governed by the quantum model for electron angular momentum, which states that the angular momentum of an electron is quantized, therefore, restricting an electron to certain quantum energy states. He utilized this idea to deal with the discrete line spectra emitted by hot Hydrogen atoms reported by Rydberg. His assumption that the angular momentum of the electron was quantized explained the inexplicable lack of collapse of the negatively charged electron of Hydrogen into the positively charged nucleus as predicted by electrostatic charge attraction. It turns out that the lowest energy orbit for an electron is given by

$$a_o = \frac{n^2h^2}{4\pi^2me^2}[\text{cgs}] = \frac{\epsilon_o n^2h^2}{4\pi^2me^2}\ [\text{MKS}] \tag{2.42}$$

[i] $h = 6.626\times10^{-34}$[J·s]
[j] This figure was adopted and modified from David S. Eisenberg, et al., reference 79, Figure10-4.

where n=1 is the lowest energy level for an electron to exist in an atom; h=6.626×10^{-27}[erg] (Planck's constant); m_e=9.10939×10^{-28}[g] (resting mass of electron); e=4.80×10^{-10}[esu] (charge of electron);

$$\Rightarrow a_o = \frac{h^2}{4\pi^2 me^2} = \frac{\left(6.626\times10^{-27}\right)^2}{4\pi^2 \cdot 9.10939\times10^{-28}\cdot\left(4.80\times10^{-10}\right)^2} = 5.29\times10^{-9}[cm] = 0.0529[nm]$$

Based on these discoveries, de Broglie proposed that all of matter exhibits both wave and particle character dependent on the following relationship

$$\lambda = \frac{h}{p} = \frac{h}{mv}$$

where h=Planck's constant (6.626 × 10^{-34} [Js]), m=mass of particle, ν=velocity of particle, $p = m\nu$ (the particle momentum), and λ is called the de Broglie wavelength. For macroscopic objects, the mass is exceedingly large compared to Planck's constant, therefore, the de Broglie wavelength is very small and the object displays no detectable wave character. Electrons, on the other hand, have an extremely small mass compared to Planck's constant (m_e=9.1094×10^{-34} [kg]), therefore, they exhibit noticeable wave character and even though they are modeled (or described) primarily by quantum mechanical methods, they can also be modeled using EM wave theory. For illustrative purposes, the following example is presented:

Given: h = 6.626×10^{-34} [J·s]; m_e= 9.10939×10^{-34} [kg] (moving mass of electron); m_t = 50x10^{-3}[kg]; v_e =2.9979E8 [m/s]; v_t =120 [mi/h]; where: t = tennis ball served at 120[mi/h]. Calculating the de Broglie wavelength for the moving electron and the tennis ball yields:

$$\lambda_e = \frac{6.626\times10^{-34}\,[\mathrm{J}\cdot\mathrm{s}]}{9.10939\times10^{-34}[kg]\times2.9979\times10^{8}[m/s]} = 2.4263\times10^{-9}\,m$$

$$\lambda_t = \frac{6.626\times10^{-34}\,[\mathrm{J}\cdot\mathrm{s}]\times3600\,[\mathrm{s/\ hr}]}{50\times10^{-3}[kg]\times120\,[mi/h]\times1609\,[m/mi]} = 2.4709\times10^{-34}\,m$$

Essentially, the answers indicate that an electron will exhibit wave nature if acted upon by visible light, which has a wavelength comparable to its de Broglie wavelength, but a served tennis ball will not exhibit any notable wave nature. So interactions of visible light and electrons will be explainable using the wave nature of light whereas the interactions of light with the served tennis ball will only be explainable by Newtonian geometric optics.

2.5.3 *Schrödinger's Wave Equation: The Underlying Basis of Quantum Mechanics*

Since all of the investigations conducted for this dissertation utilized polarized light, it is important to understand how the polarization of light creates interactions at the quantum-mechanical level that result in the measured signals, which are indicative of the sample dielectric properties. It turns out that the previously modeled simple harmonic oscillator from classic physics (Figure 2.4) is also a useful tool for understanding the quantum-mechanical formulations.[79]

Schrödinger's wave equation is the basis of quantum mechanics. Inherent in this equation are both the wave and particle nature (quantization) of energy in matter. Therefore, any solution of his equation contains concurrent information about both aspects. Furthermore, a basic postulate of quantum mechanics is that the solutions of a wave function must provide all of the measurable quantities of matter when it interacts with a light wave.[80] For any particle, the solution of the equation is a wave function ψ, which depicts the amplitude of the particle's de Broglie wave: presented in Eqn. 2.43.

The wave function describes the probability of the spatial (position) and energy (momentum) information of the particle. The properties of ψ, the wave function have no physical meaning, but $|\psi|^2=\psi\bullet\psi^*$, where * denotes the complex conjugate is proportional to the probability density of the particle, ρ. It follows, therefore, that $\psi\bullet\psi^*$ is both real and positive. Since the wave functions ψ_n*'s* completely describe a particle quantum-mechanically, they must be well behaved, i.e. they must posses certain mathematical properties: 1. be continuous 2. be finite 3. be single-valued and 4. be integrate over all of space to equal unity: i.e. $\int\psi\bullet\psi^*d\tau = 1$, where the differential volume is $d\tau$.

It is important to note that the interpretation of wave functions is based on the Heisenberg uncertainty principle, simply put: "it is impossible to know definitively both the position and velocity of a particle at the same time." Therefore, this limits the analysis to the probability that a particle will exist in some finite element of volume. This means that for a given particle location (x,y,z), the probability that the particle exists in some finite differential volume given by $dx \cdot dy \cdot dz$ is determined by $\rho\, dx \cdot dy \cdot dz$. For the particle to exist, then the probability of locating it somewhere in all of space is unity, which means that

$$\int_{\text{all space}} \rho dV = 1, \tag{2.43}$$

where V is the volume element $V=dx \cdot dy \cdot dz$. This leads to the expression for the probability density function

$$\rho = \frac{\psi \cdot \psi^*}{\int \psi \cdot \psi^* dV}, \tag{2.44}$$

where the wave function is normalized if the denominator is equal to the relationship defined in Eqn 2.43 above.

The limitations on the interpretation of $\psi \bullet \psi^*$ are based on the properties of the probability density function, that is, it must be real, finite, and single valued. This means that only certain discrete values of energy will be suitable solutions for the aforementioned boundary conditions.

Simply put, Schrödinger's wave equation for the movement of a particle in the x direction under the influence of a potential field U, which is a function of x, is given by

$$\frac{d^2\psi(x)}{dx^2} + \frac{8\pi^2 m}{h^2}\left[E - U(x)\right]\psi = 0 \tag{2.45}$$

in which ψ is the particle, time-independent, wave function, m is the particle mass, $U(x)$ is the particle potential energy as a function of its position, E is the total system energy. This equation becomes

$$\frac{\partial^2\psi(x)}{\partial x^2} + \frac{\partial^2\psi(y)}{\partial y^2} + \frac{\partial^2\psi(z)}{\partial z^2} + \frac{8\pi^2 m}{h^2}\left[E - U(x,y,z)\right]\psi = 0 \tag{2.46}$$

for a three-dimensional motion of a particle where U is a function of x, y, and z. When we rearrange Eqn. (2.46) we get

$$-\frac{1}{\psi}\frac{h^2}{8\pi^2 m}\nabla^2\psi + U = E \tag{2.47}$$

where the kinetic energy of the particle is given by

$$E_k = -\frac{1}{\psi}\frac{h^2}{8\pi^2 m}\nabla^2\psi. \tag{2.48}$$

Rearranging Eqn 2.47 and expressing in terms of the Hamilton, energy operator, we get

$$\left[-\frac{h^2}{8\pi^2 m}\nabla^2 + U\right]\psi = E\psi, \tag{2.49}$$

and recalling that the Hamilton operator in quantum mechanics is defined by

$$\mathcal{H} = \left[-\frac{h^2}{8\pi^2 m}\nabla^2 + U\right], \tag{2.50}$$

which yields the following relationship when substituted into Eqn 2.49

$$\Rightarrow \mathcal{H}\psi = E\psi. \tag{2.51}$$

This essentially means that applying the Hamilton of any system on a wave function describing the state of the system will yield the same function multiplied by the associated energy of the state. This expression in Eqn. 2.51 is an example of an eigenvalue equation of a linear operator. In this case, the energy operator, namely, the Hamilton ($\mathcal{H}$) operates on a vector function, the wave function (ψ), yielding a scaled version of the original wave function (ψ), by a factor E, termed the eigenvalue of the eigenvector (ψ). In summary, the quantum-mechanic energy operator, the Hamilton ($\mathcal{H}$), has a set of eigenvalues (E_n) for each particular wavefunction (ψ), which are discrete values corresponding to the allowed energy levels. Though there are more concise methods for deriving quantum-mechanical formulations using advanced matrix algebra methods, in the interest of understanding the underlying physics, a brute derivation of the concepts is the method of choice here.

Recalling the classical harmonic oscillator in Figure 2.3, it has oscillations along the x-axis; therefore, the potential energy function of the particle is given by

$$U = \frac{1}{2}kx^2. \tag{2.52}$$

Substituting into Eqn. 2.45, Schrödinger's wave function, yields

$$\frac{d^2\psi(x)}{dx^2} + \frac{8\pi^2 m}{h^2}\left[E - \frac{1}{2}kx^2\right]\psi = 0, \tag{2.53}$$

which by rearranging variables and several steps later leads to

$$\left[-\frac{h^2}{8\pi^2 m}\nabla^2 + \frac{1}{2}kx^2\right]\psi = E\psi. \tag{2.54}$$

The solution of the harmonic oscillator model, of Eqn. 2.54 could have more easily been obtained by simply applying the Hamilton operator as shown below by direct inspection of Eqn. 2.51.

$$\mathcal{H}\psi = E\psi$$

$$\Rightarrow \left[-\frac{h^2}{8\pi^2 m}\nabla^2 + \frac{1}{2}kx^2\right]\psi = E\psi.$$

The solutions for Eqn. 2.54 are of the form[79]

$$E_n = \left(n + \frac{1}{2}\right)\frac{h\nu}{2\pi}, \tag{2.55}$$

where in this case, n is an integer that represents the vibrational quantum number and not the lowest quantum level as n is sometimes used. It is important to note that this solution is based on the requirement for the existence of a particle that the lowest quantum level be n=1 where the particle possess a residual, *zero-point*, energy. Essentially, for the harmonic oscillator to have zero energy would violate the Heisenberg uncertainty principle; because both the momentum and position would have to be simultaneous known to be equal to zero.[81] Therefore, in agreement with this condition, when n=0 in equation (10), the particle has residual vibrational energy $E=h\nu/2$ termed the *zero-point energy*.

2.5.4 *Modeling Molecular Systems Using a Semi-Classical Approach*

Here, light will be described as a classic EM wave while matter will be described quantum-mechanically using the tools already established in the preceding section. Molecules will be represented by wavefunctions that are eigenfunctions of the energy Hamilton operator with energy states defined by the eigenvalues. The energy states will represent different stable molecular configurations, consisting of a system of charged particles in the absence of applied external EM fields. In this context, the spectral transitions responsible for measured dielectric phenomena, due to the action of the time varying EM field of the probing light wave, will account for the transformation of the molecular system from one stable state to another.

The time-dependent Schrödinger equation describes the wave function, (ψ), of a molecular system and is represented by the following relationship

$$\left[-\frac{h^2}{8\pi^2 m}\nabla^2 + U \right]\psi(t) = i\frac{h}{2\pi}\frac{\partial\psi(t)}{\partial t} \tag{2.56}$$

$$\text{Note : more common is the use of } \hbar \text{ instead of } \frac{h}{2\pi}$$

which, in terms of the Hamilton operator, reduces to

$$\mathcal{H}(t)\cdot\psi(t) = i\hbar\frac{\partial\psi(t)}{\partial t} \tag{2.57}$$

and has a solution of the form

$$\psi(t) = \phi_n e^{-(i\cdot E_n\cdot t/\hbar)}. \tag{2.58}$$

Here $\mathcal{H}(t)$ denotes the time-dependent Hamilton operator. The stable, unperturbed molecular system, is defined by the wave function, $\psi(t)$, operated on by the Hamilton operator $\mathcal{H}_0$. Therefore, when the system is perturbed, then the overall system is defined by

$$\left(\mathcal{H}_0 + \mathcal{H}(t)\right)\psi(t) = i\hbar\frac{\partial\psi(t)}{\partial t}, \tag{2.59}$$

now expanding the time dependent wave function into its eigenfunctions, results in

$$\psi(t) = \sum_{n=0}^{\infty} c_n(t) e^{-(i \cdot E_n \cdot t/\hbar)} \cdot \phi_n \quad \text{where} \quad c_n(t) e^{-(i \cdot E_n \cdot t/\hbar)} = \langle \phi_n | \psi(t) \rangle. \tag{2.60}$$

Substituting Eqn. 2.60 into 2.58 gives

$$\sum_n \left(\mathcal{H}_0 + \mathcal{H}(t) \right) \cdot c_n(t) e^{-(i \cdot E_n \cdot t/\hbar)} \cdot \phi_n = i\hbar \sum_n \frac{\partial [c_n(t) e^{-(i \cdot E_n \cdot t/\hbar)}]}{\partial t} \cdot \phi_n. \tag{2.61}$$

Recalling that for the unperturbed state,

$$\mathcal{H}_0 \psi_n = E_n \psi_n \Rightarrow \mathcal{H}_0 = E_n$$

and inputting into Eqn. 2.61, leads to

$$\sum_n \left(E_n + \mathcal{H}(t) \right) \cdot c_n(t) e^{-(i \cdot E_n \cdot t/\hbar)} \cdot \phi_n = \sum_n \left(i\hbar \frac{\partial [c_n(t)]}{\partial t} + c_n \cdot E_n \right) e^{-(i \cdot E_n \cdot t/\hbar)} \cdot \phi_n$$

$$\left[\sum_n E_n \cdot c_n(t) e^{-(i \cdot E_n \cdot t/\hbar)} \cdot \phi_n \right] \left[\sum_n \mathcal{H}(t) \cdot c_n(t) e^{-(i \cdot E_n \cdot t/\hbar)} \cdot \phi_n \right] =$$

$$\left[\sum_n E_n \cdot c_n(t) e^{-(i \cdot E_n \cdot t/\hbar)} \cdot \phi_n \right] \left[i\hbar \frac{\partial [c_n(t)]}{\partial t} e^{-(i \cdot E_n \cdot t/\hbar)} \cdot \phi_n \right]$$

$$\Rightarrow \sum_n \mathcal{H}(t) \cdot c_n(t) e^{-(i \cdot E_n \cdot t/\hbar)} \cdot \phi_n = i\hbar \frac{\partial [c_n(t)]}{\partial t} e^{-(i \cdot E_n \cdot t/\hbar)} \cdot \phi_n. \tag{2.62}$$

Multiplying through by ϕ_m^* or dotting $\langle \phi_m |$ into Eqn. 2.61, yields the time dependence of one coefficient, i.e.

$$\sum_n \mathcal{H}_{mn}(t) \cdot c_n(t) e^{-(i \cdot E_n \cdot t/\hbar)} = i\hbar \frac{\partial [c_n(t)]}{\partial t} e^{-(i \cdot E_m \cdot t/\hbar)} \tag{2.63}$$

$$\Rightarrow \frac{\partial [c_m(t)]}{\partial t} = \frac{1}{i\hbar} \sum_n \mathcal{H}_{mn}(t) \cdot c_n(t) e^{-i(E_n - E_m)t/\hbar)} = -\frac{i}{\hbar} \sum_n \mathcal{H}_{mn}(t) \cdot c_n(t) e^{-i(E_n - E_m)t/\hbar)}.$$

In summary, for the molecular system with an original stationary state, defined by ψ_n and possessing an energy E_n we are interested in investigating the probability that a perturbation $\mathcal{H}(t)$ will create a transition to a new state ψ_m of energy E_m. Since we are

only interested in two states, we can reformulate the state of the molecular system to encompass both possibilities as such,

$$\psi = c_n(t)\psi_n + c(t)_m\psi_m. \tag{2.64}$$

By theory, the system only has two states, at t=0 when $c_n(t)$=1: requiring $c_m(t)$=0, and at t >0 when $c_m(t)$ =1: requiring $c_n(t)$=0. Mathematically, this means that

$$\frac{\partial[c_m(t)]}{\partial t} = -\frac{i}{\hbar}\left(\mathscr{H}_{mn}(t)\cdot e^{i\omega_{mn}t} + \sum_{n>1}\mathscr{H}_{mn}(t)\cdot c_n(t)e^{i\omega_{mn}t}\right) \text{ where } \omega_{\text{mn}} = E_m - E_n. \tag{2.65}$$

Since we have limited our investigation to only two states of the system, this means that all other coefficients $c_{n>1}(t)$=0, therefore, leaving us with only one non zero term,

$$\frac{\partial[c_m(t)]}{\partial t} = -\frac{i}{\hbar}\left(\mathscr{H}_{mn}(t)\cdot e^{i\omega_{mn}t}\right), \tag{2.66}$$

which is the first order term, yielding

$$c_m(t) = -\frac{i}{\hbar}\int_0^t\left(\mathscr{H}_{mn}(\tau)\cdot e^{i\omega_{mn}\tau}\right)\mathrm{d}\tau \tag{2.67}$$

This integral represents the probability of the m^{th} state as a function of time based on the system originally existing at the n^{th} state for t = 0. This approximation means that the probability of the m^{th} state is dependent only on the strength of its interaction with the initial state, n, and with no other states.

Now, since we are aware that the perturbation is due to a time varying EM field, we can introduce this into the perturbation Hamilton, $\mathscr{H}(t)$, to arrive at a solution for Eqn. 2.67. Considering only the Electric field contribution to the perturbation, since achiral absorption due to magnetic induced dipoles is extremely small,[80]

$$\mathbf{E} = A_0\hat{\boldsymbol{e}}\left\{e^{i\bar{\boldsymbol{k}}\cdot\bar{r}}\left(e^{i\omega t} + e^{-i\omega t}\right)\right\}, \text{ let } \gamma = e^{i\bar{\boldsymbol{k}}\cdot\bar{r}} \tag{2.68}$$

where: $\hat{\boldsymbol{e}}$ = unit vector defining polarization direction of light;
$\bar{\boldsymbol{k}} = 2\pi\hat{k}/\lambda$; A_0 = wave amplitude; $\omega = 1/\mathrm{f}$; $\mathrm{f}_{\text{optical}} \approx 1\text{x}10^{-14}$[Hz].

By setting the center of gravity of the molecule as the origin of the coordinate system, γ can be expanded as the power series

$$\gamma = e^{i\bar{k}\cdot\bar{r}} = 1 + i\bar{k}\cdot\bar{r} - (\bar{k}\cdot\bar{r})^2 + \ldots \tag{2.69}$$

$$\text{For } |\mathrm{r}| \approx 0.1\text{-}1\,[\mathrm{nm}]\,(\text{molecular size}) \text{ and } |\mathrm{k}| = 2\pi\pi\lambda, \text{ for } \lambda \approx 100\text{-}10^3\,[\mathrm{nm}]\,(\mathrm{UV}\text{-}\mathrm{NIR})$$

$$|\bar{k}\cdot\bar{r}| \approx 10^{-3}[\mathrm{nm}] \Rightarrow \gamma = e^{i\bar{k}\cdot\bar{r}} \to 1,$$

and applying the preceding approximation, Eqn. 2.69: termed the electric dipole approximation, to Eqn. 2.67, yields

$$\mathbf{E} = A_0\hat{e}\left(e^{i\omega t} + e^{-i\omega t}\right). \tag{2.70}$$

This polarized electric field applies a perturbation creating a dipole moment such that the perturbation Hamilton is a dot product of the dipole moment and the Electric field

$$\mathcal{H}_{mn}(t) = -\bar{\mu}_{mn}\cdot\left(e^{i\omega t} + e^{-i\omega t}\right) \tag{2.71}$$

Substituting into Eqn. 2.67, yields

$$c_m(t) = \frac{i\bar{\mu}_{mn}}{\hbar}\int_0^t\left[e^{i\omega_{mn}\tau}\left(e^{i\omega\tau} + e^{-i\omega\tau}\right)\right]\mathrm{d}\tau = \frac{\bar{\mu}_{mn}}{\hbar}\left[\frac{e^{i(\omega_{mn}+\omega)\tau}}{\omega_{mn}+\omega} + \frac{e^{i(\omega_{mn}-\omega)\tau}}{\omega_{mn}-\omega}\right]_0^t$$

$$c_m(t) = \frac{\bar{\mu}_{mn}}{\hbar}\left[\frac{e^{i(\omega_{mn}+\omega)t}-1}{\omega_{mn}+\omega} + \frac{e^{i(\omega_{mn}-\omega)t}-1}{\omega_{mn}-\omega}\right] \tag{2.72}$$

Here, $\omega_{mn} \approx \omega$ in order for the original perturbation assumption to hold. This implies that the first fraction in the denominator is negligible with respect to the second term which is considerable larger. Therefore the expression reduces to

$$c_m(t) = \frac{\bar{\mu}_{mn}}{\hbar}\left[\frac{e^{i(\omega_{mn}-\omega)t}-1}{\omega_{mn}-\omega}\right]. \tag{2.73}$$

In order to determine the probability that the system is in the m^{th} state at time t, we square $|c_m(t)|$ leading to

$$\left|c_m(t)\right|^2 = \frac{\left|\overline{\mu}_{mn}\right|^2}{\hbar^2}\left[\frac{2-(e^{i(\omega_{mn}-\omega)t}+e^{-i(\omega_{mn}-\omega)t})}{(\omega_{mn}-\omega)^2}\right] = \frac{\left|\overline{\mu}_{mn}\right|^2}{\hbar^2}\left(\frac{\sin^2\left[\frac{1}{2}(\omega_{mn}-\omega)\cdot t\right]}{\left[\frac{1}{2}(\omega_{mn}-\omega)\right]^2}\right) \tag{2.74}$$

From Eqn. 2.74 and recalling Eqn. 2.13, it is clear that the probability of a transition due to an Electric field generated perturbation depends on the alignment of the polarization vector of the incident electric field with $\boldsymbol{\mu}$: the electric dipole moment, and is proportional to $|\boldsymbol{\mu}|^2$: the square of the dipole moment. Further note that as t→0, the system transition rate equation tends toward a delta function, leading to the following relation:

$$\frac{\left|c_m(t)\right|^2}{t} = \frac{2\pi\left|\overline{\mu}_{mn}\right|^2}{\hbar^2}\left(\frac{\sin^2\left[\frac{1}{2}(\omega_{mn}-\omega)\cdot t\right]}{2\pi t\left[\frac{1}{2}(\omega_{mn}-\omega)\right]^2}\right) \rightarrow R_{mn} = \frac{2\pi}{\hbar^2}\left|\langle\psi_m|\mu|\psi_n\rangle\right|^2\delta(\omega_{mn}-\omega) \tag{2.75}$$

Where, R_{mn} is the probability per unit time that a system transition is induced from the n^{th} to the m^{th} state, with a net result of absorption when $E_m=E_n+\omega$, and of emission when $E_m=E_n-\omega$; this was derived by applying Eqn 2.41 for an extremely tiny perturbation at optical frequency.

Note: a more direct method utilizing normalized wavefunctions would have readily arrived at the same solution by applying the properties of normality, and orthogonality to generate the same orthonormal eigenstates.

2.5.5 *Concluding Remarks on the Quantum-Mechanical Approach to Light Matter Interactions versus the Classic Approach*

With the quantum-mechanical approach the probability of light photons interacting with matter, can be determined *a priori*: i.e. without having a physical model already built to guide the investigation, whereas a physical model is necessary for the classic approach. In the case of the harmonic oscillator, having a working knowledge of the physical

model made it easier to make sense of the physical significance of the quantum-mechanical formulations but was not necessary to determine the processes of the absorption and emission of light, which account for all of the measurable output effects that yield all of the measurable physical parameters when polarized light is used to interrogate a sample of matter. Put more concisely, the final solution of the wave function indicates that the absorption and emission of light, the only two cases possible from the solution, are the only two measurable parameters that tell us everything we need to know about the interaction of light with matter. Therefore, all of the measurable output effects when light interacts with matter, which includes the optical dielectric properties of matter, can be determined from just two parameter measurements, namely, the absorption and emission of light. This was not apparent in the classic model because it did not determine the emission of light that accounts for such optical phenomena as fluorescence and phosphorescence, but was limited to the emission of light that accounts for transmission and dispersion. In conclusion, the absorption and reemission of photons by electrons is primarily responsible for the observable measurable output effects of light interaction with matter, which reveals the optical dielectric properties of matter, albeit bulk optical properties.

2.6 Dielectric Properties of Matter

2.6.1 *General Overview*

In the preceding sections it was established that all of the dielectric properties of matter are determinable from the measurement of two optical parameters, namely, the absorption and emission of light intensity. It follows, therefore, that all of the optical dielectric properties will be a direct consequence of anisotropies in the absorption and emission of light. Jones in his landmark paper, "A New Calculus for the treatment of optical systems VII,[82] identified eight independent optical dielectric properties; he termed "differential matrices" that are all based on the absorption and reemission of light of varying polarizations. The following sections are an investigation of the mathematical

descriptions of polarized light and how they pertain to the eight measurable differential dielectric properties of matter.

2.6.2 *Polarized Light*

As in classical Mathematics in which the geometric shapes such as the straight line, circle, parabola, and hyperbola are all special cases derived from the application of certain constraints to an ellipse, similarly in the field of polarization, all possible polarization states of a light wave are derivable by instituting constraints on the fundamental elliptical polarization state,

$$\frac{E_y{}^2}{E_{0y}{}^2} + \frac{E_x{}^2}{E_{0x}{}^2} - 2\frac{E_y}{E_{0y}}\frac{E_x}{E_{0x}}\cos\varepsilon = \sin^2\varepsilon, \tag{2.76}$$

where

$$\tan 2\alpha = \frac{2E_{0y}E_{0x}\cos\varepsilon}{E_{0x}{}^2 - E_{0y}{}^2}, \tag{2.77}$$

and E_{ox} and E_{oy} represent the magnitudes of the electric field vector along the orthogonal E_x and E_y axes as the light wave propagates along the z-axis with a phase difference of $\varepsilon = \varepsilon_y - \varepsilon_x$ between the E_x and E_y components. The necessary constraints on Eqn 2.76 to drive all of the basic polarization states are presented in Table 2.2. Figure 2.7, is a pictorial depiction of the polarization ellipse and its parameters as the electric vector is seen to subscribe an ellipse, with a major axis angled at α with respect to the horizontal x-axis, as the light wave propagates out of the page towards the reader. Finally, a pictorial representation of the basic polarization states is presented in Figure 2.8.

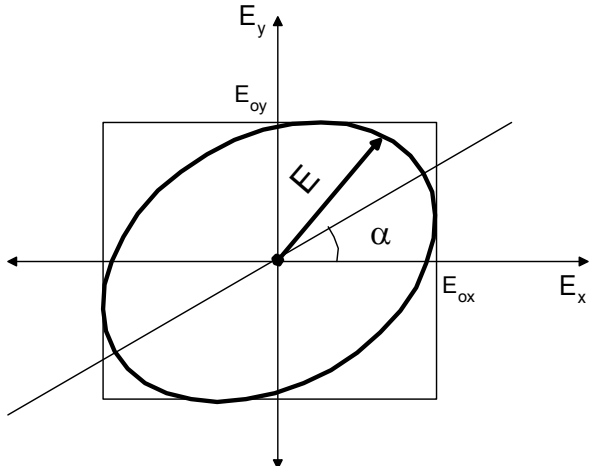

Figure 2.7: An ellipse demonstrating the parameters for a polarized light wave.

Table 2.2: Summary of the derivation of the standard polarization states from the general elliptical polarization.[k]

***POLARIZATION STATE* [Symbol]**	***CONSTRAINT***		***EQUATION***
	Phase	***Amplitude***	
***Horizontal* [H]**	$\varepsilon = \pm n\pi$ $n=0, 1,...$	$E_y = 0$ $E_o = E_{ox}$	$\mathbf{E} = \mathbf{E_x} + \mathbf{E_y} = \mathbf{E_x}$ $\mathbf{E_x}(z,t) = \hat{\imath}\, E_o \cos(kz-\omega t)$
***Vertical* [V]**	$\varepsilon = \pm n\pi$ $n=0, 1,...$	$E_{ox} = 0$ $E_o = E_{oy}$	$\mathbf{E} = \mathbf{E_x} + \mathbf{E_y} = \mathbf{E_y}$ $\mathbf{E_y}(z,t) = \hat{\jmath}\, E_o \cos(kz-\omega t)$
***Plus 45 deg.* [P]**	$\varepsilon = \pm n\pi$ $n=0, 1,...$	$E_{oy} = E_{ox}$ $= E_o$	$\mathbf{E} = \mathbf{E_x} + \mathbf{E_y}$ $\mathbf{E}(z,t) = (\hat{\imath} + \hat{\jmath})\, E_o \cos(kz-\omega t)$
***Minus 45 deg.* [M]**	$\varepsilon = \pm n\pi$ $n=0, 1,...$	$E_{oy} = E_{ox}$ $= E_o$	$\mathbf{E} = \mathbf{E_x} + \mathbf{E_y}$ $\boldsymbol{E}(z,t) = (\hat{\imath} - \hat{\jmath})\, E_o \cos(kz-\omega t)$
***Right Circular* [R]**	$\varepsilon = \pm n\pi/2$ $n=1, 2,...$	$E_{oy} = E_{ox}$	$\boldsymbol{E} = Eo[\hat{\imath}\, E_o \cos(kz-\omega t) + \hat{\jmath}\, E_o \sin(kz-\omega t)]$
***Left Circular* [L]**	$\varepsilon = \pm n\pi/2$ $n=1, 2,...$	$E_{oy} = E_{ox}$	$\boldsymbol{E} = Eo[\hat{\imath}\, E_o \cos(kz-\omega t) - \hat{\jmath}\, E_o \sin(kz-\omega t)]$

[k] Summarized from Eugene Hecht, reference 78, chapter 8.

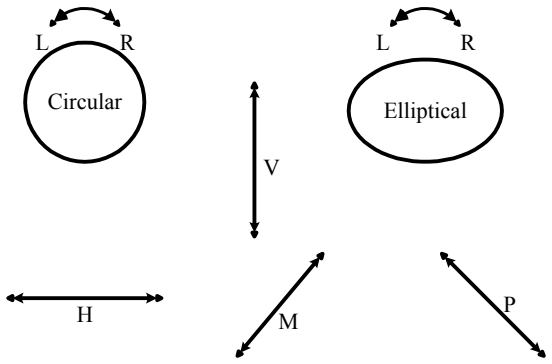

Figure 2.8: Pictorial representation of the pattern subscribed by the vibration of the E-field of a polarized light wave that is propagating out of the page toward the reader.

2.6.3 *The Measurement of the Intensity of a Light Wave*

The intensity of the a light wave is calculated by the time averaged value of the Poynting vector, given by

$$I \equiv \langle S \rangle_T = c^2 \in_0 \left| \mathbf{E_0} \times \mathbf{B_0} \right| \left\langle \cos^2(\mathbf{k} \bullet \mathbf{r} - \omega t) \right\rangle = \frac{c \in_0}{2} E_0{}^2 = c \in_0 \langle E^2 \rangle_T, \qquad (2.78)$$

i.e. the intensity of an EM wave is proportional to the square of the E-field vector, where $\langle \ \rangle_T$ denotes the time averaged value, and × denotes the vector cross product.

2.6.4 *The Stokes Vector Representation of Light*

The intensity of the polarization vector of a light beam can be completely described using the 4×1 Stokes vector:[78]

$$\begin{bmatrix} S_0 \\ S_1 \\ S_2 \\ S_3 \end{bmatrix} = \begin{bmatrix} \langle E_{0x}{}^2 \rangle_T + \langle E_{0y}{}^2 \rangle_T \\ \langle E_{0x}{}^2 \rangle_T - \langle E_{0y}{}^2 \rangle_T \\ \langle 2E_{0x}E_{0y} \cos\varepsilon \rangle_T \\ \langle 2E_{0x}E_{0y} \sin\varepsilon \rangle_T \end{bmatrix} = \begin{bmatrix} I_0 \\ I_H - I_V \\ I_P - I_M \\ I_R - I_L \end{bmatrix}, \qquad (2.79)$$

where, I denotes the measured intensity value, S_0 is the total detected light intensity, of which S_1 is the portion that corresponds to the difference between the linear horizontal

$\langle E_{ox}^2 \rangle_T$ and vertical $\langle E_{oy}^2 \rangle_T$ polarization states, S_2 is the portion that corresponds to the difference between the linear +45° and –45° polarization states, and S_3 is the portion that corresponds to the difference between the right circular and left circular polarization states.[74] The Stokes vector formulation can handle both polarized and unpolarized light states, where the degree of polarization, DOP, is determined by

$$DOP = \frac{\sqrt{S_1^2 + S_2^2 + S_3^2}}{S_0}. \tag{2.80}$$

The DOP ranges from $0 \leq \text{DOP} \leq 1$, since the normalized total intensity can never exceed a value of 1, where the normalization of the Stokes vector is accomplished by dividing all of the elements by the S_0 element.

2.6.5 *Mueller Matrix Representation of Light*

The Mueller matrix is a mathematical representation, based on intensity measurements, of the dielectric polarization properties of a given sample such that the detected Stokes vector of the output beam is based on the combination of the input beam Stokes vector with the sample Mueller matrix. Thus, from Eqn. 2.81, knowing the input light polarization state, $[S]_{IN}$, and the detected light polarization state, $[S]_{OUT}$, the sample Mueller matrix, [M], can be determined from

$$\begin{bmatrix} S_0 \\ S_1 \\ S_2 \\ S_3 \end{bmatrix}_{OUT} = \begin{bmatrix} M_{11} & M_{12} & M_{13} & M_{14} \\ M_{21} & M_{22} & M_{23} & M_{24} \\ M_{31} & M_{32} & M_{33} & M_{34} \\ M_{41} & M_{42} & M_{43} & M_{44} \end{bmatrix} \begin{bmatrix} S_0 \\ S_1 \\ S_2 \\ S_3 \end{bmatrix}_{IN}, \tag{2.81}$$

using the derivations presented in Table 2.3.

Table 2.3: The Mueller matrix derivation equations (a) using 16, (b) using 36, and (c) using 49 polarization images, where the first and second terms represent the input and output polarization states respectively, which are defined as: H = Horizontal, V = Vertical, P = + 45°, M = -45°, R = Right circular, and L = Left circular, O=Open, i.e. no polarization.

M_{11} =HH+HV+VH+VV	M_{12} =HH+HV-VH-VV	M_{13} =2PH+2PV-M_{11}	M_{14} =2RH+2RV-M_{11}
M_{21} =HH-HV+VH-VV	M_{22} =HH-HV-VH+VV	M_{23} =2PH-2PV-M_{21}	M_{24} =2RH-2RV-M_{21}
M_{31} =2HP+2VP-M_{11}	M_{32} =2HP-2VP-M_{12}	M_{33} =4PP-2PH-2PV-M_{31}	M_{34} =4RP-2RH-2RV-M_{31}
M_{41} =2HR+2VR-M_{11}	M_{42} =2HR-2VR-M_{12}	M_{43} =4PR-2PH-2PV-M_{41}	M_{44} =4RR-2RH-2RV-M_{41}

(a)

M_{11} =HH+HV+VH+VV	M_{12} =HH+HV-VH-VV	M_{13} =PH+PV-MH-MV	M_{14} =RH+RV-LH-LV
M_{21} =HH-HV+VH-VV	M_{22} =HH-HV-VH+VV	M_{23} =PH-PV-MH+MV	M_{24} =RH-RV-LH+LV
M_{31} =HP-HM+VP-VM	M_{32} =HP-HM-VP+VM	M_{33} =PP-PM-MP+MM	M_{34} =RP-RM-LP+LM
M_{41} =HR-HL+VR-VL	M_{42} =HR-HL-VR+VL	M_{43} =PR-PL-MR+ML	M_{44} =RR-RL-LR+LL

(b)

M_{11} = OO	M_{12} = HO−VO	M_{13} = PO−MO	M_{14} = RO−LO
M_{21} = OH−OV	M_{22} = HH−HV−VH+VV	M_{23} = PH−PV−MH+MV	M_{24} = RH−RV−LH+LV
M_{31} = OP−OM	M_{32} = HP−HM−VP+VM	M_{33} = PP−PM−MP+MM	M_{34} = RP−RM−LP+LM
M_{41} = OR−OL	M_{42} = HR−HL−VR+VL	M_{43} = PR−PL−MR+ML	M_{44} = RR−RL−LR+LL

(c)

The requirements for a theoretical realizable Mueller matrix are

$$Tr\left(\mathbf{M}\mathbf{M}^{\mathrm{T}}\right) \geq 4\mathrm{M}_{11}{}^{2} \tag{2.82}$$

$$\mathrm{M}_{11} \geq \left|\mathrm{M}_{ij}\right| \tag{2.83}$$

$$M_{11}^{\ 2} \geq M_{12}^{\ 2} + M_{13}^{\ 2} + M_{14}^{\ 2} \tag{2.84}$$

$$\left(M_{11} - \sqrt{M_{12}^{\ 2} + M_{13}^{\ 2} M_{14}^{\ 2}}\right)^2 \geq \sum_{j=2}^{4}\left(M_{1j} - \sum_{k=2}^{4}\left(M_{j,k} \cdot \frac{M_{1j}}{\sqrt{M_{12}^{\ 2} + M_{13}^{\ 2} M_{14}^{\ 2}}}\right)\right) \tag{2.85}$$

where *Tr* is the trace of the matrix and $\mathbf{M}^{\mathrm{T}}$ is the transpose of **M**, the sample Mueller matrix. In practice, since the matrices for ideal polarizers, retarders, and other non-depolarizing components lie on the boundary for theoretical realizability, it is possible to get results that slightly exceed these requirements in an experimental system.[83]

2.6.6 *Jones Matrix Representation of Light*

The Jones matrix formulation can be used to represent all of the dielectric properties of a non-depolarizing sample, i.e. DOP=1. This is based on

$$\begin{bmatrix} E_x \\ E_y \end{bmatrix} = \begin{bmatrix} a_{11} & a_{12} \\ a_{21} & a_{22} \end{bmatrix} \begin{bmatrix} E_{ox} e^{i\phi_x} \\ E_{oy} e^{i\phi_y} \end{bmatrix}, \tag{2.86}$$

where the measured light intensity is given by

$$I \cong \left[\langle E_x \rangle_T^{\ 2} + \langle E_y \rangle_T^{\ 2}\right] = \left[\langle E_x^{\ *} \cdot E_x \rangle_T + \langle E_y^{\ *} \cdot E_y \rangle_T\right], \tag{2.87}$$

and E_x and E_y are the components of the vertical and horizontal components of the E-vector, having corresponding scalar amplitudes of E_{ox} and E_{oy}, with phase components of ϕ_x and ϕ_y.[78] Therefore, the Jones matrix formulation is based on the measurement of the amplitude and phase of the electric vector and not directly based on intensity measurements.

The Jones vector formulation for an arbitrary unknown sample has the advantage of requiring only 7 independent measurements, disregarding the absolute phase, versus a minimum of 16 independent measurements for the Mueller matrix formulations.

2.6.7 *A Comparison of Mueller and Jones Matrix Representation of Dielectric Properties*

This section outlines the eight dielectric properties and some methods for determining them using polarized light. It is clear from Table 2.4 that all of the dielectric parameters are indeed measurements of the absorption and emission of polarized light, which is the basis for the experiments that will be discussed in the coming chapters. Furthermore, the dielectric polarization properties of matter can be more clearly understood when viewed in the context of the different methods for generating polarized light using various samples of matter; this is presented in Section 2.6.8.

Table 2.4: This table is a summary of the 8 dielectric properties, their symbols as used in this text, and their experimental measurements, where A = standard absorbance, η = refractive index, *l* = sample path length, c = molar concentration, λ = wavelength of light, α = the observed polarimetric rotation, k = extinction coefficient, and the subscripts indicate the state of polarized light for the measurement.[84, 85]

$[m_i]$	Physical Parameter	Phenome-nological symbol[1]	Experimental Measurement	Jone's Formulation[82] $[\Theta_i]$ per unit length
1	Isotropic absorption	A_e *or* p	$\ln(10 \cdot \varepsilon \cdot c \cdot l)$	$\kappa = \frac{2\pi \cdot k}{\lambda}$
2	Isotropic refraction (arbitrary phase)	η	$\frac{2\pi \cdot n \cdot l}{\lambda}$	$\eta = \frac{2\pi \cdot n}{\lambda}$
3	Linear Birefringence 1	LB_0	$\frac{2\pi \cdot \Delta n_0 \cdot l}{\lambda}$	$p_0 = \frac{1}{2}(\kappa_y - \kappa_x)$
4	Linear Birefringence 2	LB_{45}	$\frac{2\pi \cdot \Delta n_{45} \cdot l}{\lambda}$	$g_{45} = \frac{1}{2}(\kappa_{-45} - \kappa_{45})$

[1] Modified from H. P. Jensen, reference 84, Table II.

Table 2.4: Continued

$[m_i]$	Physical Parameter	Phenome-nological symbol[l]	Experimental Measurement	Jones Formulation[82] $[\Theta_i]$ per unit length
5	Linear Dichroism 1	LD_0	$\ln(10 \cdot \Delta\varepsilon_0 \cdot c \cdot l/2)$	$g_0 = \frac{1}{2}(\eta_y - \eta_x)$
6	Linear Dichroism 2	LD_{45}	$\ln(10 \cdot \Delta\varepsilon_{45} \cdot c \cdot l/2)$	$g_{45} = \frac{1}{2}(\eta_{-45} - \eta_{45})$
7	Circular Birefringence	CB	$\pi \cdot \frac{\alpha}{90}$	$\omega = \frac{1}{2}(\eta_r - \eta_l)$
8	Circular Dichroism	CD	$\ln(10 \cdot \Delta\varepsilon_{lr} \cdot c \cdot l/2)$	$\delta = \frac{1}{2}(\kappa_l - \kappa_r)$

In contemporary literature, LD_0, LD_{45}, and CD are commonly referred to as diattenuations[83,86] because they are based on the asymmetrical absorption of orthogonal polarizations of light, which results in the differential attenuation of polarized light. The term dichroism refers to the earlier means of detecting asymmetrical absorption in crystals, which was based on observing two, '*di*', different colors ('*chrois*')[m] determined by the crystal axis that was used for viewing.[87] Similarly, CB, LB_0, and LB_{45} are referred to as retardances instead of birefringence[83,89] because the matrix value is the actual retardance; a function of the sample birefringence, which is a constant. The sample birefringence is based on the differential speed of propagation of two orthogonal polarization states of light, a direct result of the existence of more than one refractive index of light in a birefringent sample.

[m] English *chrois* originates from Greek *khros*

Table 2.5: Corresponding Mueller matrix formulation for the 8 dielectric properties, for a non-depolarizing anisotropic sample.[n]

M_{11} =HH+HV+VH+VV (*p*)	M_{12} =HH+HV-VH-VV -(LD_0)	M_{13} =PH+PV-MH-MV -(LD_{45})	M_{14} =RH+RV-LH-LV (CD)
M_{21} =HH-HV+VH-VV -(LD_0)	M_{22} =HH-HV-VH+VV (*p*)	M_{23} =PH-PV-MH+MV (CB)	M_{24} =RH-RV-LH+LV (LB_{45})
M_{31} =HP-HM+VP-VM -(LD_{45})	M_{32} =HP-HM-VP+VM -(CB)	M_{33} =PP-PM-MP+MM (*p*)	M_{34} =RP-RM-LP+LM -(LB_0)
M_{41} =HR-HL+VR-VL (CD)	M_{42} =HR-HL-VR+VL -(LB_{45})	M_{43} =PR-PL-MR+ML (LB_0)	M_{44} =RR-RL-LR+LL (*p*)

2.6.8 *An Investigation of Dielectric Polarization Properties from the Perspective of Polarized Light Production*

Keeping in mind that all of the dielectric properties of matter can be determined from the absorption and emission of light, this means that a sample of matter exhibiting anisotropies in the absorption and emission of light, will exhibit polarization properties. The polarization properties are depolarization: the ability to depolarize incident polarized light, diattenuation: the dependence of light transmission on the incident polarization state, polarizance: the ability to polarize unpolarized incident light, and retardance: the ability to generate a phase shift in the electric vector of the incident polarized light, therefore, possibly changing its state of polarization (SOP).

2.6.8.1 *Depolarization Property*

For a sample of matter to exhibit the property of a depolarizer, this requires a homogenous and isotropic structural arrangement of matter such that all of the incident

[n] Adopted from T. T. Tower and R. T. Tranquillo, reference 88, Eqn. 3.

polarized light is scattered and depolarized equally in all directions. Practically, this can only be determine experimentally with a transmission or backscattered light measurement scheme where the surface reflected light would not be registered, because surface light, i.e. specular reflection, still retains its polarization with a helicity flip for incident the cases M, P, R, and L.

The normalized Mueller matrix for a depolarizer sample is

$$\begin{bmatrix} 1 & 0 & 0 & 0 \\ 0 & 0 & 0 & 0 \\ 0 & 0 & 0 & 0 \\ 0 & 0 & 0 & 0 \end{bmatrix}, \tag{2.88}$$

which can be derived from Table 2.5 by setting all of the detected intensity values to the same value because a homogeneous isotropic depolarizing sample will register the same intensity regardless of the probing incident polarization state. Physically, depolarization of light by a sample of matter can be a reusult of multiple scattering of photons, or a rapid or random change in the phase or wavelength of the emitted photons that result in a scrambling of the output polarization of the emitted light beam such that it does not favor any polarization state over the others. Practically, all matter depolarizes light to a degree established by its asymmetric and inhomogeneous makeup.The depolarizance of a sample can be determined by comparing the Eucledian distance of its Mueller matrix to that of an ideal depolarizer using:

$$DPI = 1 - \frac{\sqrt{\left(\sum_{ij} M_{ij}^{\ 2}\right) - M_{11}^{\ 2}}}{M_{11} \cdot \sqrt{3}}, \tag{2.89}$$

where i and j are the index integers for the elements of the Mueller matrix sans the M_{11} element, *DPI* is the Depolarization index varying in value from 0 for a perfect polarizer or retarder to 1 for an ideal depolarizer.[83] Most matter falls somewhere between the two ideal cases, i.e. $0 < DPI < 1$. It is worth noting that the Stokes vector of the light detected from any depolarizing sample can be separated into two parts, a depolarized portion, S_D, and a 100% polarized portion, S_P, based on the *DOP,* i.e.[83]

$$S = S_D + S_P = \begin{bmatrix} S_0 \\ S_1 \\ S_2 \\ S_3 \end{bmatrix} = (1 - DOP) \cdot S_0 \begin{bmatrix} 1 \\ 0 \\ 0 \\ 0 \end{bmatrix} + S_0 \cdot DOP \begin{bmatrix} 1 \\ S_1/(S_0 \cdot DOP) \\ S_2/(S_0 \cdot DOP) \\ S_3/(S_0 \cdot DOP) \end{bmatrix}. \quad (2.90)$$

2.6.8.2 ***Diattenuation (Dichroism) Property***

For a sample to exhibit diattenuation, the structural arrangement must be one that creates differential absorption of different polarization states of light. From the sample Mueller matrix, in Table 2.5, the average transmitted light intensity $T_{avg} = M_{11}$ and the maximum and minimum transmitted light intensities T_{max} and T_{min} are given by[83]

$$T_{max} = M_{11} + \sqrt{M_{12}{}^2 + M_{13}{}^2 + M_{14}{}^2} \quad \text{and} \quad T_{min} = M_{11} - \sqrt{M_{12}{}^2 + M_{13}{}^2 + M_{14}{}^2}, \quad (2.91)$$

which yield the maximum and minimum Stokes vectors, S_{max} and S_{min},

$$S_{max} = \begin{bmatrix} \sqrt{M_{12}{}^2 + M_{13}{}^2 + M_{14}{}^2} \\ M_{12} \\ M_{13} \\ M_{14} \end{bmatrix} \quad \text{and} \quad S_{min} = \begin{bmatrix} \sqrt{M_{12}{}^2 + M_{13}{}^2 + M_{14}{}^2} \\ -M_{12} \\ -M_{13} \\ -M_{14} \end{bmatrix}. \quad (2.92)$$

The diattenuation, D, of the sample Matrix, M, is determined by

$$D(M) = \frac{T_{max} - T_{min}}{T_{max} + T_{min}} = \frac{\sqrt{M_{12}{}^2 + M_{13}{}^2 + M_{14}{}^2}}{M_{11}}, \quad (2.93)$$

where the Linear Diattenuation, LD, component is determined by

$$LD(M) = \frac{\sqrt{M_{12}{}^2 + M_{13}{}^2}}{M_{11}} \quad (2.94)$$

and the Circular Diattenuation, CD, component by

$$CD(M) = \frac{M_{14}}{M_{11}}. \quad (2.95)$$

The diattenuation, *D*, varies from a value of 1 for an ideal polarizer to 0 for an ideal retarder, ideal depolarizer, or other nonpolarizing sample.[83]

2.6.8.3 *Polarizance Property*

For a sample to exhibit polarizance, it has to have a structural arrangement that enables it to reflect, absorb and re-emit, light at oblique angles, or one that results in either the differentially absorption of orthogonal polarization components of light or in the differentially absorption of linear versus circularly polarized light. Polarizance, *P*, can be determined from a sample Mueller matrix by[83]

$$P(\mathrm{M}) = \frac{\sqrt{\mathrm{M}_{12}{}^2 + \mathrm{M}_{13}{}^2 + \mathrm{M}_{14}{}^2},}{\mathrm{M}_{11}} \tag{2.96}$$

where *P* varies from a value of 1 for an ideal polarizer to a value of 0 for a nonpolarizing sample, such as an ideal waveplate or depolarizer. Hence, the complete asymmetric absorption of a polarization state by a sample, while simultaneously passing the orthogonal polarization state, can be a practical means for generating polarized light, which is the case for wire grid and Polaroid sheet polarizers.[89, 90]

On the other hand, if the polarizance is reflection based, the maximum polarizance will occur at Brewster's angle: the 100% linear polarizing angle. Unpolarized incident light that is reflected, absorbed and reemitted, at oblique angles other than Brewster's angle will create partial linear polarized reflected and transmitted beams. For reflection at Brewster's angle, you get approximately 8% of the total incident energy reflected as 100% linear polarized reflected light with a polarization state perpendicular (per) to the plane of incidence, while the transmitted beam contains approximately 92% of the incident energy and is partially linearly polarized primarily parallel (par) to the incident plane of incidence. Thus, asymmetric reflection from the surface of a sample generates polarizance, which can be used as a means of producing polarized light as in the case of pile-of-plates polarizers.[89, 90]

Another process that generates polarizance is the asymmetric refraction of light.[o] When unpolarized light is incident on a birefringent crystal at other than along the optic axis, the beam is double refracted and separated into two observable beams propagating with two different wave velocities, which are 100% polarized with states orthogonal to each other. The polarizations produced by a birefringent crystal can be linear circular or elliptical, therefore, leading to the corresponding sample characterization of linearly, circularly, or elliptically birefringent. By blocking one of the polarized beams, using total internal reflection and or absorption, a 100% polarized beam is outputted.[89,90] Therefore, the asymmetric refraction of light generates polarizance, and this process can be applied to produce polarized light using birefringent crystals.

Asymmetrical scattering can also generate polarizance particularly that due to Rayleigh scatter. When the size of the scatters is much smaller than the wavelength of unpolarized light, the Rayliegh scattering, absorption and re-emission of light due to generated dipole oscillations, generates polarized light of varying DOP in all directions except in the forward direction, where the ensuing light beam is unpolarized.[p]

2.6.8.4 *Retardance Property*

For a sample to exhibit retardance, it has to have a structural arrangement that enables it to retard the transmission, i.e. the absorption and re-emission, of light of orthogonal polarization orientations relative to each other. Physically, Retardance can be generated by the process of reflection or by sample birefringence. In the case of reflection, the phase shift generated by dielectric samples differs for external and total internal reflections. Figures 2.9 (a) and (b) are the plots for the phase shift generated for internal and external reflections at a glass/air interface for a glass sample of refractive index 1.5,

---

[o] This was the original means used by Huygens to discover polarization due to the double refraction of light by a calcite crystal

[p] This process accounts for the polarization effects of skylight observed due to the Rayliegh scatter of the light rays from the sun by tiny atmospheric particles, such as dust particles.

which yields a critical angle for TIR of 41.8° and a polarization, Brewster's, angle of 56.3°.[91]

From Figure 2.9(a) it is evident that for a given input polarization state different states of polarized light can be produced based on the number of internal reflections of the beam before being re-emitted from the glass crystal. In fact, incident linear polarized light can be converted into circular polarized light by two internal reflection events before being re-emitted. On the other hand, from Figures 2.9(b) through (d), for incident unpolarized light only linear polarized light of varying DOP and azimuthal orientation, which are based on the percentage of the reflected light of par and per polarization orientation, can be produced from external reflection events because the phase shift between the two orthogonal components, i.e. the perpendicular and parallel to the plane of incidence components, is always 0 or pi which corresponds to a linear polarization state.[q]

Retardance changes that are a result of birefringence are a primary hindrance for the non-invasive detection of glucose using polarized light transmission through the aqueous humor of the eye in which the light beam twice traverses the birefringent cornea of the eye. As such, a more detailed treatment of the theory for the generation of retardance as a consequence of light traversing a birefringent sample is presented later in Chapter III, which deals with non-invasive polarimetric glucose detection. Nevertheless, the asymmetric retardation of orthogonal polarization states, whether due to reflection effects or inherent sample birefringence, produces retardance, which is evident in the M_{44} element of the sample Mueller matrix.

---

[q] Recalling Table 2.2 for $\varepsilon = \pm n\pi$, where n=0,1, ...

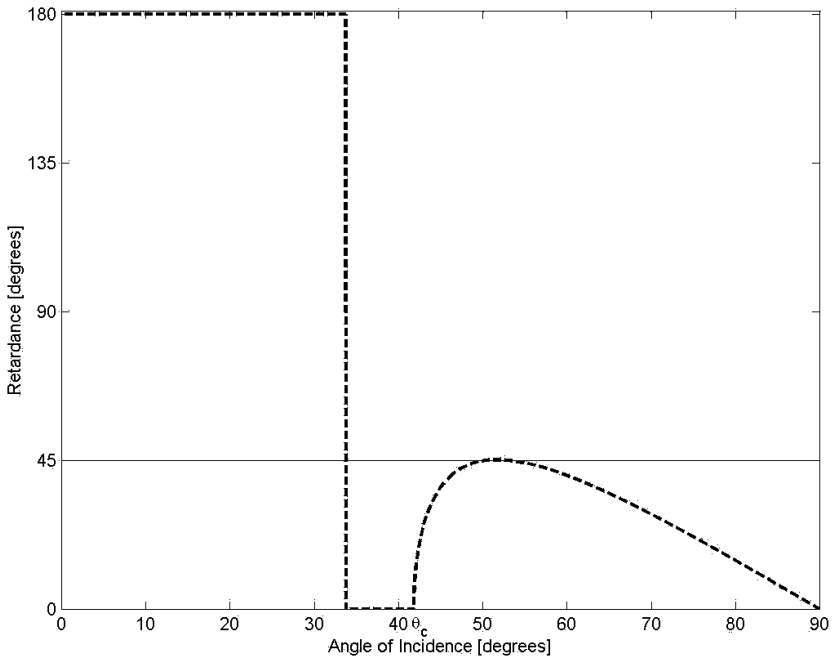

(a)

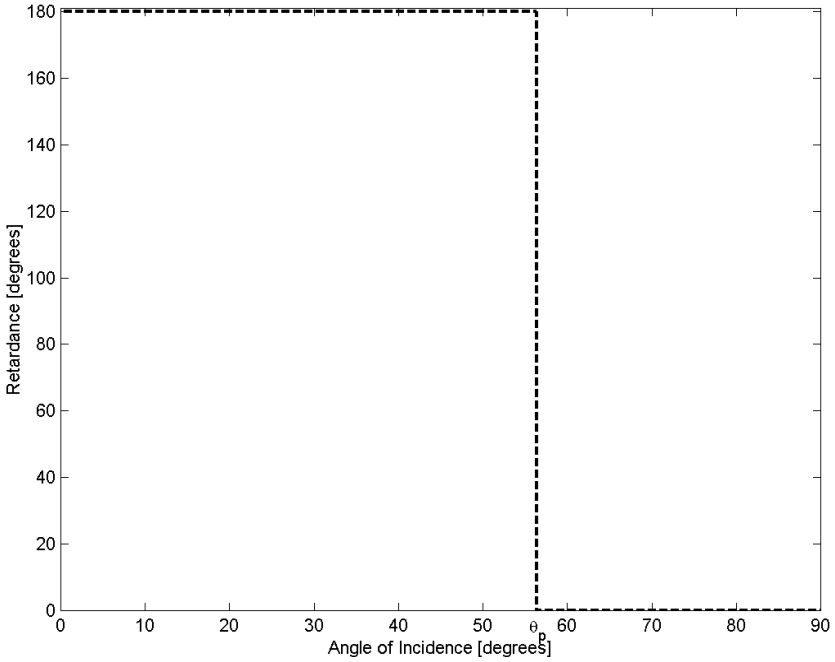

(b)

Figure 2.9: Depiction of retardance, i.e. phase difference between the Par and Per component of incident unpolarized light, for a air glass interface where η_{glass} =1.5, θ_c=41.8°, and θ_p=56.3° for (a) total-internal-reflection; (b) external reflection.

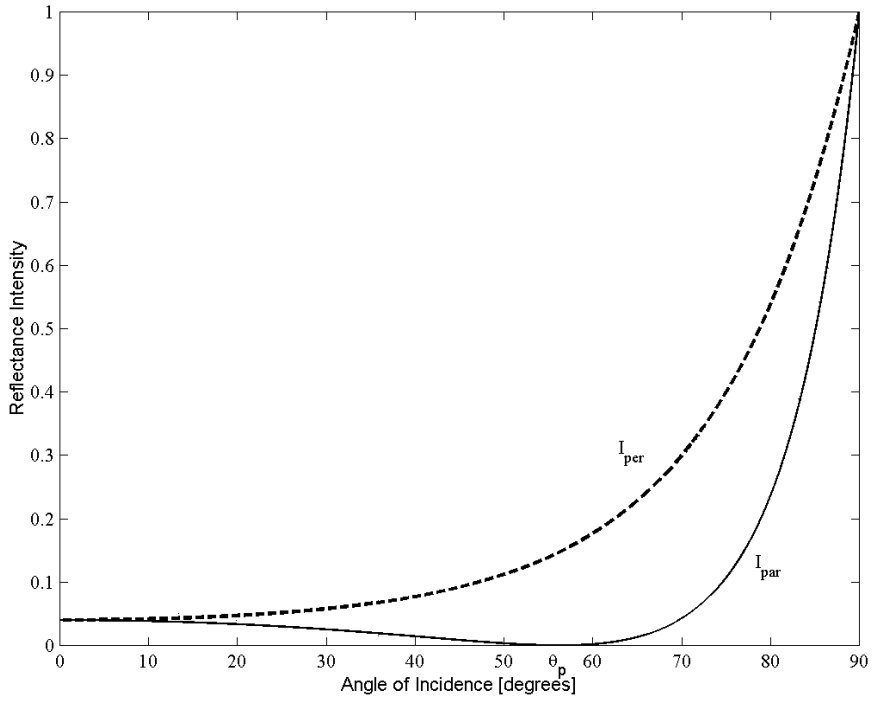

(c)

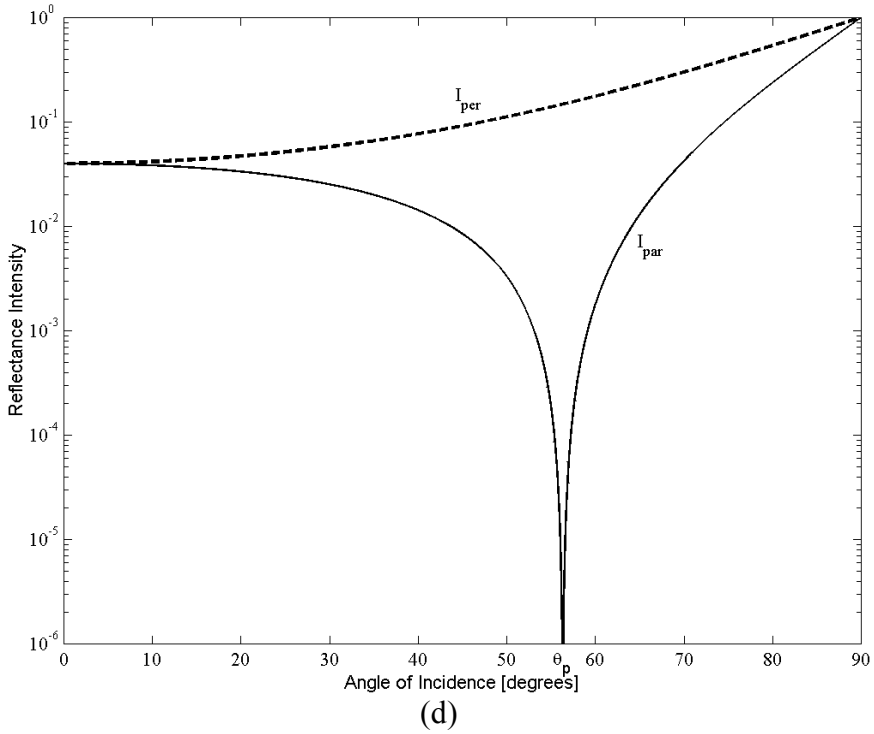

(d)

Figure 2.9: Continued; (c) normal scale and (d) log scale.

2.6.8.5 *Summary of the Dielectric Polarization Properties from the Perspective of Polarized Light Production*

In summary, a dielectric sample of matter can exhibit polarization properties due to structural asymmetries that lead to one, some, or all of the aforementioned polarization characteristics.

CHAPTER III
THE APPLICATION OF POLARIZED LIGHT FOR THE RELATIVE MEASUREMENT OF RABBIT CORNEAL BIREFRINGENCE[r]

As stated in the Chapter I, there is a need for a non-invasive blood glucose measurement device to aid diabetics. Numerous groups have investigated the polarimetric approach and several problems have been addressed.[2,16,17,19,20,45-49,52-55] However, there is still one major problem remaining to make this method a reality, namely, how to compensate for the changes in the polarimetric signal that are generated by movement of the eyeball which brings in to play the spatial variations in corneal birefringence.

This chapter will begin with a quick overview of the problems and the solutions to the polarimetric glucose sensing modality through the eye as implemented by our group. Then it will address the challenges associated with using the polarimetric system for *in vivo* studies, which is the basis for conducting the study, described in the later parts of this chapter, on the measurement of the relative rabbit corneal birefringence.

3.1 An Overview of the Problems of Polarimetric Glucose Detection through the Eye and the Investigated Solutions

3.1.1 *The Time Lag between Blood and Aqueous Humor Glucose Levels*

Determining the time delay between changes in blood glucose levels and those of the aqueous humor is fundamental to establishing the practicality of the proposed sensor. For the glucose concentration readings of the aqueous humor to be useful to a diabetic, the delay needs to be short enough to enable the patient to make the necessary

---

[r] Part of this chapter is reprinted with permission from Journal of Biomedical Optics, reference 20. J. S. Baba, B. D. Cameron, S. Theru, and G. L. Cote, "Effect of temperature, pH, and corneal birefringence on polarimetric glucose monitoring in the eye." *J Biomed Opt.* **7**(3), 321-328 (2002).

intervention to maintain their blood glucose levels within that of normal. More critically for the diabetic patient is the ability to detect the onset of a hypoglycemic condition, such that corrective actions can be taken to avoid short-term affects such as fainting or more dangerously the onset of a coma, which can be a potentially fatal condition. Hence, it is essential that the readings are accurate and attainable within a short time span.[36,37]

In 1982, a preliminary experimental study conducted by March et al.[45,46] using New Zealand White rabbits provided some insight on the time delay and the correlation between blood and aqueous humor glucose levels. Although preliminary, their study indeed demonstrated a correlation. However, because only two data points were collected from each rabbit, at two hour intervals, it could only be speculated that the order of the time delay was under two hours though it was indicated that it should be considerably less under more normal circumstances. More recently, Chou et al.[9,54] using a preliminary non-invasive single wavelength optical polarimetric technique had published that the time delay seemed to be on the order of thirty minutes. However, their results have not been duplicated and our discussions with this group identify that future studies still need to be conducted to verify that it was indeed aqueous humor glucose being measured by their system. Based on these varying published reports and on our private communications with others on the potential time delay, it became necessary to conduct a more complete and conclusive measurement of the delay.

In our recently published report, five New Zealand White (NZW) rabbits were used to directly measure the delay between the blood and aqueous humor glucose levels.[16] The average time delay from all animals was found to be within five minutes. This experiment was conducted using normal nondiabetic animals by withdrawing time corresponding aqueous humor and blood samples over a course of weeks and then using a standard bench top electrochemical approach (Yellow Springs Instruments) to determine the glucose concentrations. The elevation of glucose concentrations in the rabbit model was attained using a Ketamine/Xylazine anesthesia protocol. The time lag, T_{delay}, was determined once we fit the data and determined the peak locations for blood, T_{peak_blood}, and aqueous humor, $T_{peak\_aqueous}$, as $T_{delay} = T_{peak\_aqueous} - T_{peak\_blood}$.

A plot showing the elevated blood and aqueous humor normalized glucose concentrations, and depicting the time lag for one animal is presented in Figure 3.1.

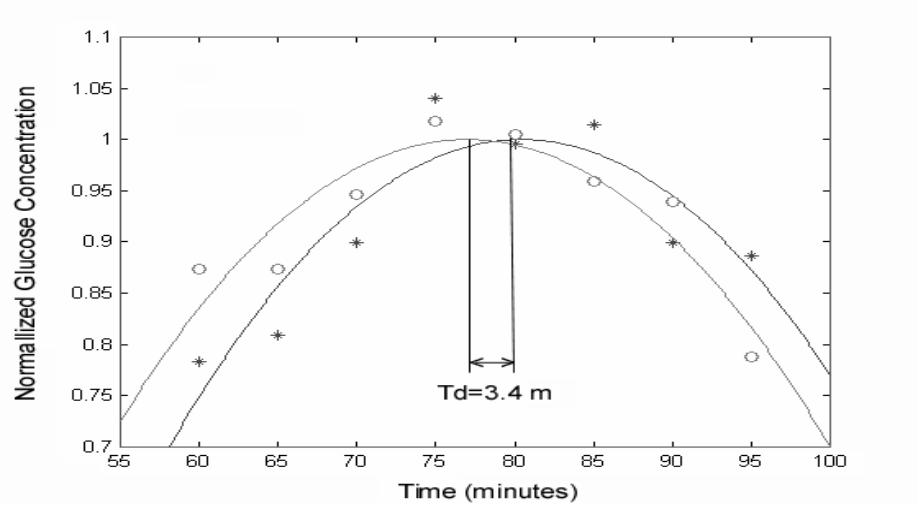

Figure 3.1: Time-delay results for a single NZW rabbit based on measurements made with an YSI glucose analyzer. The time lag determined here is less than five minutes.

3.1.2 *Low Signal-To-Noise Ratio for the Polarimetric Measurement of Physiological Concentrations of Glucose*

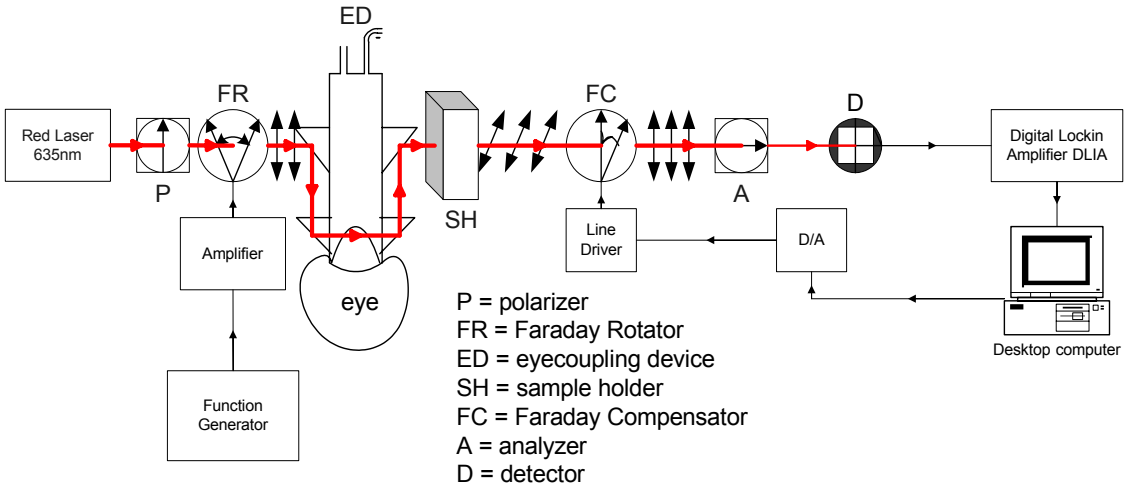

Figure 3.2: Block diagram of the designed and implemented digital closed-loop controlled polarimeter, where the sample holder is used for *in vitro* samples and the eye-coupling device, which is filled with saline, is used for *in vivo* studies.

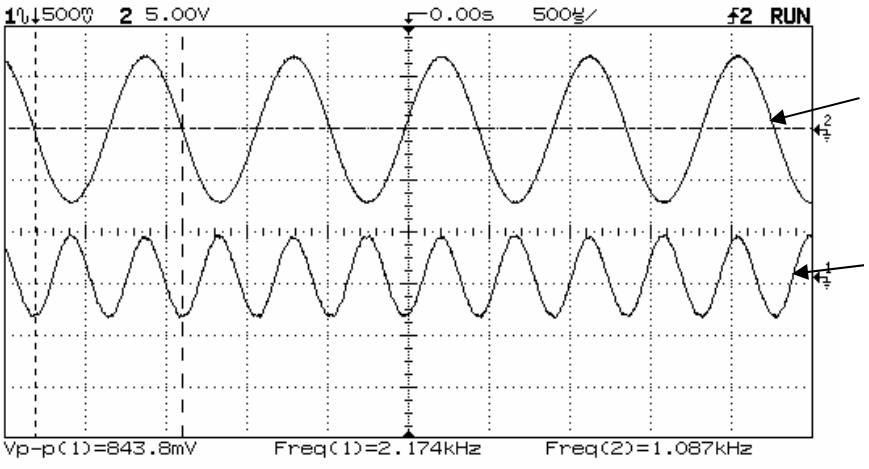

(a)

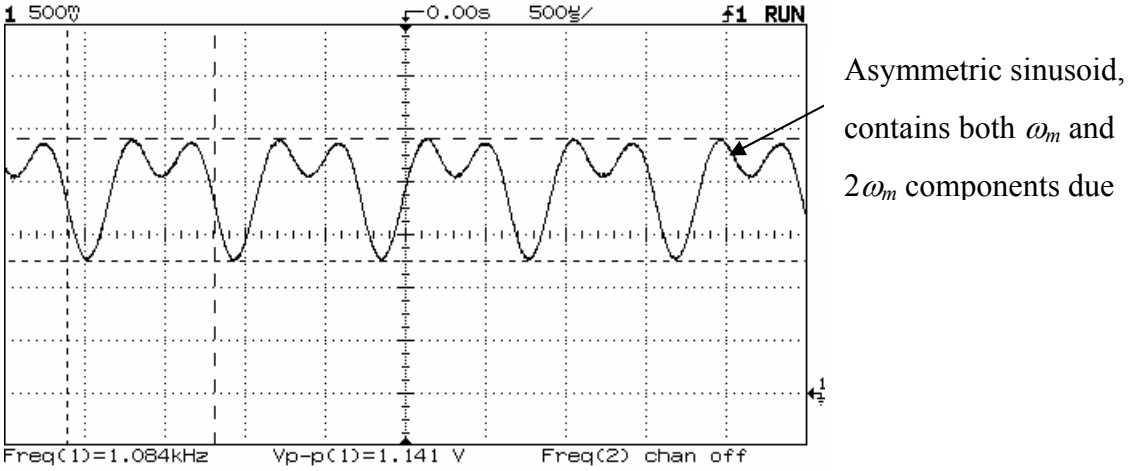

(b)

Figure 3.3: (a) The top sinusoid is the Faraday modulation signal (ω_m) used as the reference for the lock-in amplifier and the bottom sinusoid is the double modulation frequency ($2\omega_m$) signal detected for a perfectly nulled system. (b) This sinusoid is the detected signal when an optically active sample, like glucose, is present.

$$I \propto E^2 = \left(\phi^2 + \frac{\theta_m^2}{2}\right) + 2\phi\theta_m \sin(\omega_m t) - \frac{\theta_m^2}{2}\cos(2\omega_m t) \tag{3.1}$$

DC offset $\quad$ 1.09 kHz, ω_m $\quad$ 2.18 kHz, $2\omega_m$

To address this issue, in an earlier approach, depicted in Figure 3.2, we designed and implemented a single wavelength polarization modulated closed-loop polarimetric system.[53] Mathematically, the operation of the system is based on Eqn. 3.1, where θ_m is the depth of the Faraday modulation, ω_m is the modulation frequency, and ϕ represents the rotation due to the optically active sample subtracted by any feedback rotation due to the compensation Faraday rotator. From Eqn. 3.1, it is evident that, without an optically active sample and with the DC term removed, the detected signal only consists of the double modulation frequency ($2\omega_m$) term, represented by the bottom signal in Figure 3.3a. However, when an optically active sample is present, such as glucose, the detected signal then becomes an asymmetric sinusoid, represented in Figure 3.3b, which contains both the fundamental (ω_m) and the $2\omega_m$ modulation frequency terms.

The previously obtained results from the sample calibrations for four individual runs of glucose doped water are presented in Table 3.1.[53] These results demonstrate the system robustness and establish that the system has the sensitivity to accurately resolve physiological concentrations of glucose. The plots for the best results in validation (i.e. using a previously formed calibration model and an independent set of data for prediction) are shown in Figure 3.4.

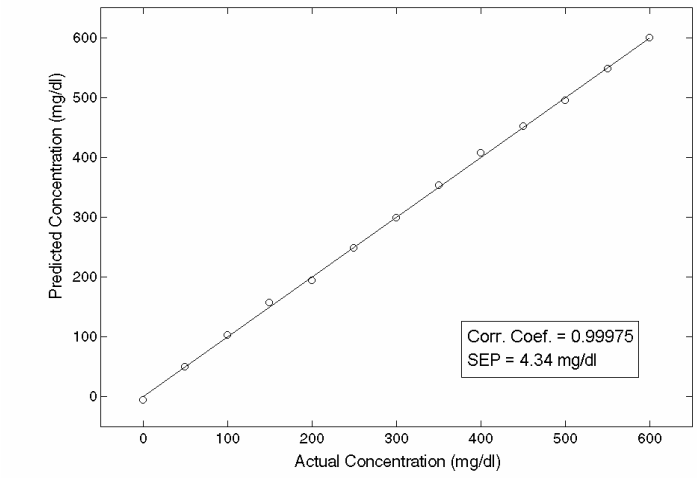

Figure 3.4: Predicted versus actual glucose concentrations for the hyperglycemic glucose doped water experiments, where the line represents the error free estimation ($y=x$).

Table 3.1: Summary statistics for four individual data sets collected for water doped glucose samples.

Medium	Run	Correlation Coefficient (r)	Standard Error of Prediction in Calibration [mg/dl]	Standard Error of Prediction in Validation [mg/dl]
Glucose and Water	1	0.99888	9.24	7.26
	2	0.99909	8.30	8.64
	3	0.99956	5.77	9.69
	4	0.99975	4.34	9.76

3.1.3 *Confounding Effects of Other Chiral Constituents in Aqueous Humor to Polarimetric Glucose Measurement*

Since the basis of polarimetric glucose concentration determination is the amount of rotation of a linearly polarized incident beam by glucose, the presence of other chiral molecules within the aqueous humor creates the potential for confounding this measurement. To address this problem, Gough et al.[48] investigated the contributions of potential aqueous humor confounders to glucose measurement within the wavelength range of 365nm to 589nm. More recently, our group[20] extended this work to include the full visible spectrum for the two primary optical confounders to glucose measurements in the eye namely, albumin and ascorbic acid. These results are illustrated in Figure 3.5 and summarized in Table 3.2. It can be seen that the contributions of albumin and ascorbic acid are negligible, particularly at higher wavelengths. It is worth noting that the effect of albumin and ascorbic acid in Table 3.2, are evaluated for their average physiological levels. This is based on the assumption that any fluctuations in their concentrations within their full physiological ranges will be minimal and slow in the aqueous humor compared to those of glucose. In addition, these two components are contra-rotatory and thus will partially cancel each other. Therefore, it is not likely that these optically active substances in the eye will significantly affect the glucose signal. However, if necessary, a multi-wavelength system should enable the compensation of any confounding effects due to other chiral analytes. These conclusions are supported by the results from prior work done by this group (King et al.[92] and Cameron et al.[2]) all of

which indicate a significant decrease in glucose prediction errors, in the presence of confounders, utilizing a multi-wavelength system as compared to the results obtained using a single wavelength system. Lastly, due to the temperature and pH dependence of optical activity, we investigated the potential effects of varying temperature and pH on glucose measurements. Our results suggest that temperature and pH effects will be negligible in vivo due to the small changes in optical activity within their physiological ranges of variation.[93]

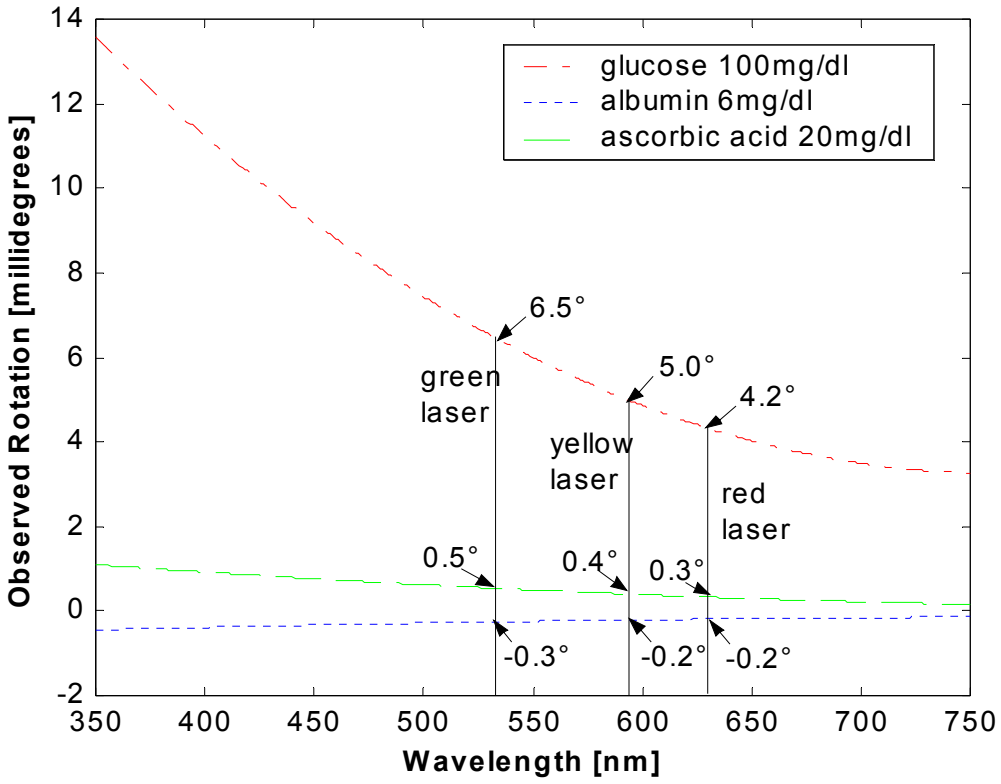

Figure 3.5: Observed optical rotations for physiological concentrations of aqueous humor analytes, glucose, albumin, and ascorbic acid for a 1cm pathlength.

Table 3.2: This presents the contributions of physiological concentrations of albumen, 6 mg/dl, and ascorbic acid, 20mg/dl, to the detected observed rotation when glucose is present and varies within physiological concentrations: extreme hypoglycemic 40mg/dl, normal 100mg/dl, and extreme hyperglycemic 600mg/dl.

	% MAXIMUM CONTRIBUTION TO OBSERVED ROTATION					
	Glucose 40mg/dl		Glucose 100mg/dl		Glucose 600mg/dl	
Wavelength	532nm	635nm	532nm	635nm	532nm	635nm
Albumen	5.48	6.13	2.48	2.81	0.45	0.51
Ascorbic Acid	13.69	15.30	6.19	7.02	1.11	1.28

3.1.4 *The Confounding Effects of Motion Artifact Coupled With the Spatial Variations in Corneal Birefringence*

Corneal birefringence becomes a problem when there is motion artifact because the affect of birefringence masks the glucose signature. For our *in vivo* measurement system, motion artifact has been a recurrent problem. In order to understand this issue, the source of the noise needed to be isolated. Using the single wavelength system depicted in Figure 3.2 and an anesthetized rabbit, a spectral analysis of our detected signal was obtained. As depicted in Figure 3.6, the artifact was found to be a result of changes the location of eyeball with respect to the stationary input laser beam due to respiratory motion and, to a limited extent, the cardiac cycle. This motion brought into play the spatial variations in corneal birefringence, thus causing a change in the measured signal that was not due to glucose. Based on the reason that this was a direct response to the respiratory and cardiac cycles and not to some random eye motion, i.e. it is a systematic and not a systemic error, this means that it cannot be entirely removed (for instance in a human by asking the person to focus their vision straight ahead). Thus, this finding necessitates the development of a robust method for measurement in the presence of birefringence.

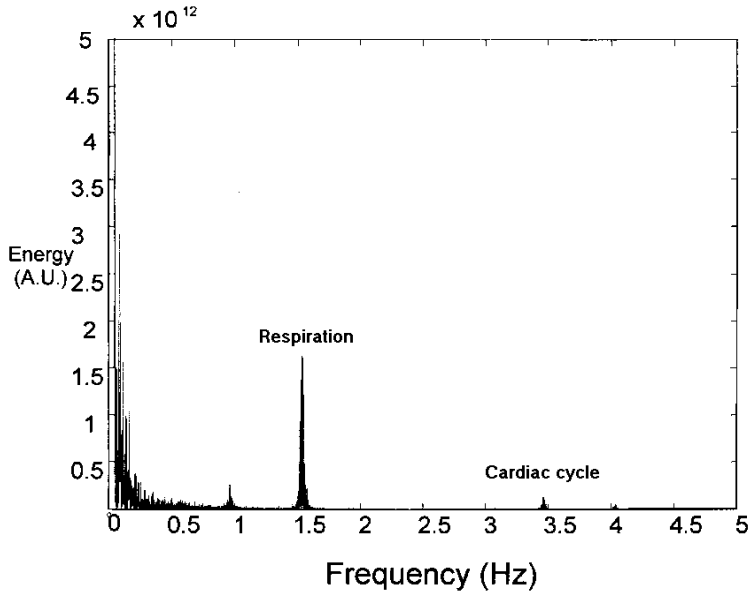

Figure 3.6: The fft of the detected signal from an *in vivo* study aimed at measuring glucose optical rotation in an anesthetized rabbit. This shows the presence of motion artifact due to respiration and, to a lesser degree, the cardiac cycle in our detected signal.

In order to develop a robust polarimetric glucose detection system, it is necessary to quantify the degree of the relative spatial variations in corneal birefringence, which confounds polarimetric glucose measurements through the eye. The birefringence of the eye is well documented in literature and numerous investigators have studied and developed models for corneal birefringence.[94-107] However, these models are based on the transmission of light through excised and fixated cornea *in vitro*, [94-98,101-103] or by *in vivo* imaging of back reflected light that has traversed the apex of the cornea and reflected off the inner structures, e.g. iris, retina, lens.[99,100,104-107] For our geometry (see Figure 3.7), where we couple light laterally to traverse the anterior chamber of the eye from the tear duct to the opposite edge where the upper and lower eyelids meet, these models are insufficient. The rest of the discussion in this chapter will address the specific task of mapping the spatial variations in corneal birefringence as seen by the aforementioned *in vivo* polarimetric glucose system.

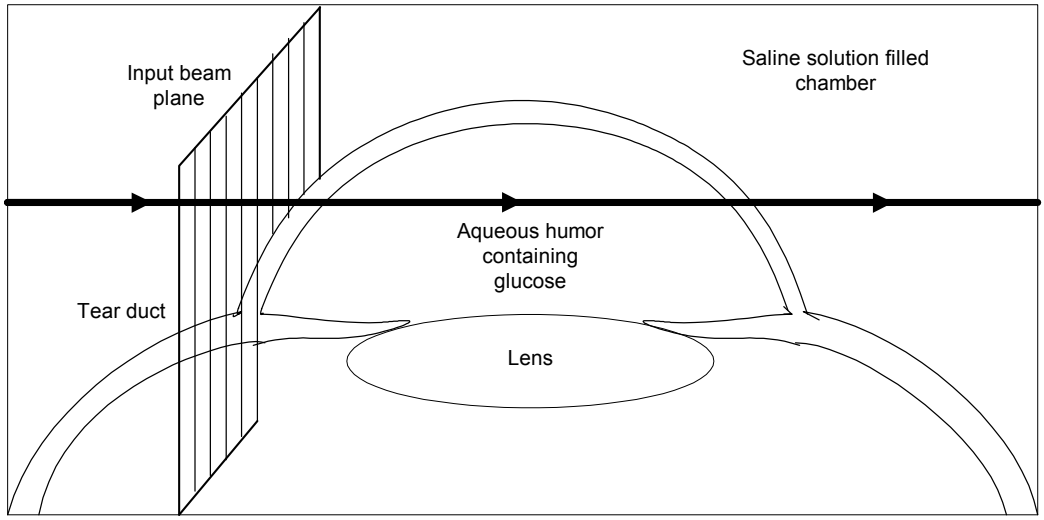

Figure 3.7: Diagram depicting glucose detection eye-coupling geometry.

3.2 Birefringence Theory

3.2.1 *Quantum-Mechanical Explanation for Inherent Birefringence*

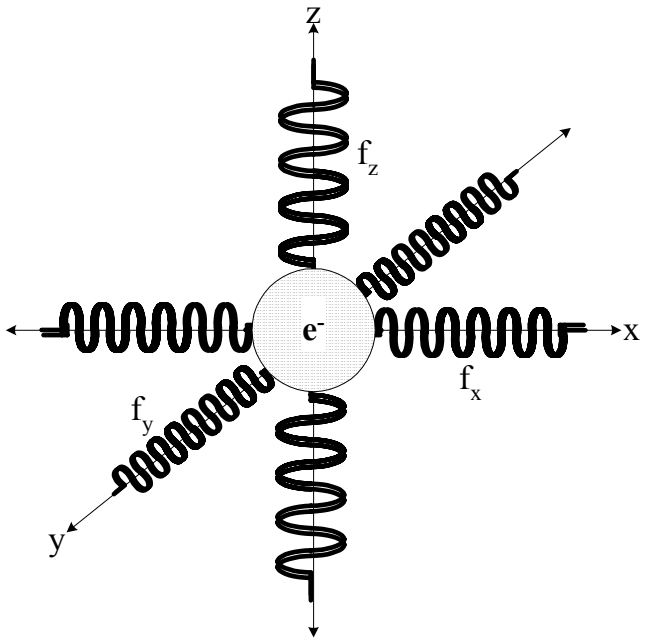

Figure 3.8: Diagram illustrating electron binding force spatial asymmetry.

Applying Section 2.5.4 to Figure 3.8 yields

$$U = \frac{1}{2}\left(f_x x^2 + f_y y^2 + f_z z^2\right) \tag{3.2}$$

$$\left[-\frac{h^2}{8\pi^2 m}\nabla^2 + \frac{1}{2}\left(f_x x^2 + f_y y^2 + f_z z^2\right)\right]\psi = E\psi \tag{3.3}$$

$$\mathscr{H}_{mn}(t) = -\overline{\mu}_{mn} \cdot \left(e^{i\omega t} + e^{-i\omega t}\right)\left(\hat{\boldsymbol{i}} + \hat{\boldsymbol{j}} + \hat{\boldsymbol{k}}\right) \tag{3.4}$$

which leads to an absorption and emission of light that are based on the polarization orientation of the incident EM field. From a classical mechanics point of view, applying Eqn 2.23 to Figure 3.8 gives

$$F_{\text{bind}} = -f_x x + f_y y + f_z z = -m\left(\omega_{x0}{}^2 x + \omega_{y0}{}^2 y + \omega_{z0}{}^2 z\right), \tag{3.5}$$

and Eqn 2.30 now becomes a dot product represented by

$$\boldsymbol{\mu}'_{ind} = q \cdot x'_0(t) \bullet \left(\hat{\boldsymbol{i}} + \hat{\boldsymbol{j}} + \hat{\boldsymbol{k}}\right), \tag{3.6}$$

which yields

$$\boldsymbol{\mu}'_{ind} = \frac{Nq^2}{m}\left(\sum_{l=x}^{z} \frac{1}{\omega_{l0}{}^2 - \omega_l{}^2 - i\xi\omega_l} E_l e^{-i\omega\cdot t}\right) \tag{3.7}$$

Recalling Eqn 2.33, where

$$\boldsymbol{\mu}'_{\text{ind}} = \in_0 \chi'_e \mathbf{E}', \text{ and } \in' \equiv \in_0 (1 + \chi'_e)$$

$$\Rightarrow \in' \equiv \left[1 + \frac{Nq^2}{m \in_0}\left(\sum_j \frac{n_j}{\omega_j{}^2 - \omega^2 - i\xi_j\omega}\right)\right] \;;$$

this means that

$$\left|\boldsymbol{\mu}'_{\text{ind}}\right| \propto \begin{bmatrix} \in'_{11} & \in'_{12} & \in'_{13} \\ \in'_{21} & \in'_{22} & \in'_{23} \\ \in'_{31} & \in'_{32} & \in'_{33} \end{bmatrix}\begin{bmatrix} E_x \\ E_y \\ E_z \end{bmatrix} \propto \begin{bmatrix} \chi'_{11} & \chi'_{12} & \chi'_{13} \\ \chi'_{21} & \chi'_{22} & \chi'_{23} \\ \chi'_{31} & \chi'_{32} & \chi'_{33} \end{bmatrix}\begin{bmatrix} E_x \\ E_y \\ E_z \end{bmatrix}. \tag{3.8}$$

Birefringence is a phase retardation of emitted light from a sample due to the incident EM radiation encountering principle axes asymmetries. From section 2.4.2, Eqn. 2.13 suggests that the induced electric dipole moment, $\boldsymbol{\mu}_{\text{ind}}$, is always aligned with the applied external electric field, **E**, that generated it. This is true for an isotropic

sample, but for a birefringent sample, anisotropies exist between the principle axes of the sample, which can lead to the misalignment of the dipole moment with the plane of polarization of the incident field. Hence, birefringence is a phase retardation of emitted light from a sample due to the incident EM radiation encountering principle axes asymmetries that leads to a non-coplanar induced dipole moment. As illustrated in Figure 3.8, the binding forces on an electron in the structural arrangement can vary spatially along the x, y, and z directions. Recalling Eqn. 2.14, this implies that the electric susceptibility, χ_e, is a 3×3 tensor, as is the complex dielectric constant, $\in'$. For a non-absorbing medium, only the diagonal elements, corresponding to the three principle axes, are non-zero. Therefore, when an incident EM wave interacts with such an electron, the displacement of the electron, thus the induced dipole moment, becomes a function of the spatial orientation of the incident polarization. The net result is that the induced dipole moment is not aligned with the plane of the incident field polarization.

In the case where the plane of the linear polarization vector of the incident light wave aligns with one of the principle axes, the induced dipole moment generated is aligned with the incident plane of polarization. From Eqn. 3.8 given a Horizontal incident SOP for a wave propagating along the z-axis, i.e. E_y=E_z= 0, yields a dipole moment, $|\boldsymbol{\mu}'_{ind}| \propto E_x \cdot \chi'_{11} = a$, with a direction given by: $\hat{\boldsymbol{r}} = E_x \hat{\boldsymbol{i}}$, which is aligned with the incident field SOP. Because of this alignment, the incident and scattered light will have the same SOP because the phase retardation between the fields will be an integer multiple of π (refer to Table 2.2). However, in the case where the plane of the linear polarization vector of the incident light wave does not align with any of the principle axes, i.e. E_z= 0, and $E_x \neq E_y \neq 0$, the induced dipole moment is not aligned with the incident plane of polarization. This misalignment introduces a phase retardation between the incident and emitted: transmitted, fields that is not an integer multiple of π, therefore, the field of the scattered light will be out of phase with the incident field, thus, changing the incident linear SOP polarization to an elliptical SOP.[80] This can be explained further, using Table 3.3 in conjunction with Eqn. 3.8.

Table 3.3: Classification of birefringence based on the number of principle axes lacking symmetry for non-absorbing media.[s]

CLASSIFICATION -Crystalline Arrangement	**ELECTRIC SUSCEPTIBILITY**	**REFRACTIVE INDEX / INDICES**
Isotropic -Cubic	$\begin{bmatrix} \chi'_{11} & 0 & 0 \\ 0 & \chi'_{22} & 0 \\ 0 & 0 & \chi'_{33} \end{bmatrix} = \begin{bmatrix} a & 0 & 0 \\ 0 & a & 0 \\ 0 & 0 & a \end{bmatrix}$	$\eta_o(\omega) \cong \sqrt{\epsilon'} = \sqrt{(1+a)}$
Uniaxial -Trigonal -Tetragonal -Hexagonal	$\begin{bmatrix} \chi'_{11} & 0 & 0 \\ 0 & \chi'_{22} & 0 \\ 0 & 0 & \chi'_{33} \end{bmatrix} = \begin{bmatrix} a & 0 & 0 \\ 0 & a & 0 \\ 0 & 0 & b \end{bmatrix}$	$\eta_o(\omega) \cong \sqrt{\epsilon'} = \sqrt{(1+a)}$ $\eta_e(\omega) \cong \sqrt{\epsilon'} = \sqrt{(1+b)}$
Biaxial -Triclinic -Monoclinic -Orthorhombic	$\begin{bmatrix} \chi'_{11} & 0 & 0 \\ 0 & \chi'_{22} & 0 \\ 0 & 0 & \chi'_{33} \end{bmatrix} = \begin{bmatrix} a & 0 & 0 \\ 0 & b & 0 \\ 0 & 0 & c \end{bmatrix}$	$\eta_1(\omega) \cong \sqrt{\epsilon'} = \sqrt{(1+a)}$ $\eta_2(\omega) \cong \sqrt{\epsilon'} = \sqrt{(1+b)}$ $\eta_3(\omega) \cong \sqrt{\epsilon'} = \sqrt{(1+c)}$

From Table 3.3 and Eqn. 3.8, an optic axis exists for the case of a uniaxial crystal such that if the incident light beam propagates along the z-axis: the χ_{33} principle axis - which is the optic axis, the polarization of the output beam will be retained;

$$\left|\boldsymbol{\mu}'_{\text{ind}}\right| \propto E_x \cdot \chi'_{11} + E_y \cdot \chi'_{22} = 2a \text{ with a direction given by } \hat{\boldsymbol{r}} = E_x\hat{\boldsymbol{i}} + E_y\hat{\boldsymbol{j}}.$$

Eqn 3.8 suggests that the incident polarization state is retained because the incident electric field encounters the same electric susceptibilities, as if the sample were isotropic, as it traverses the sample because $\chi_{11} = \chi_{22} = a$. In the case where the incident beam does not propagate along the optic axis, then from Eqn 3.8, the incident polarization state is not retained because it encounters asymmetric orthogonal susceptibilities. Likewise if the structure of the matter represents a biaxial crystal, then the incident SOP is always changed due to the interaction with the sample[80] and

$$\left|\boldsymbol{\mu}'_{\text{ind}}\right| \propto E_x \cdot \chi'_{11} + E_z \cdot \chi'_{33} = a + b \text{ with a direction given by } \hat{\boldsymbol{r}} = E_x\hat{\boldsymbol{i}} + E_z\hat{\boldsymbol{k}}.$$

---

[s] Adopted from Grant R. Fowles, reference 75, pp. 175.

3.2.2 *Phenomenological Explanation for Birefringence*

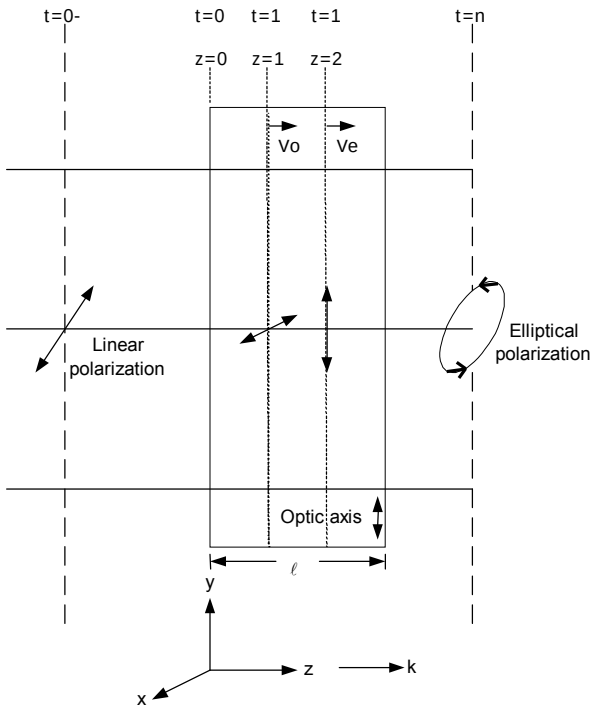

Figure 3.9: Birefringent sample effect on an input linear polarized light beam. The beam is decomposed into two orthogonal components of differing wave velocities, ν_o and ν_e, one aligned with the optic axis and the other perpendicular to the optical axis. The output light is converted into an elliptical polarization by the phase shift introduced between the normal and extraordinary velocity waves during propagation.

Birefringence describes the phenomena where an incident light beam experiences two refractive indices for light, the ordinary refractive index η_o (along the slow axis) and the extra-ordinary refractive index η_e (along the fast axis), as it propagates through a medium. This process can be characterized by the separation of an incoming ray of light into two orthogonal polarization components traveling at differing phase velocities. Figure 3.9 illustrates this phenomenon; where a normal incident linearly polarized light beam at time t=0 propagates with two different phase velocities within the birefringent medium, ν_o (slower, ordinary) and ν_e (faster, extra-ordinary). At a later time, t=1, the

phase angle between the orthogonal components, has changed from the initial odd integer multiple of nπ . Finally, when detected at some later time, t=n, after propagating through the medium length *l*, the polarization is no longer linear but elliptical. This change in the input SOP, due to birefringence, confounds the rotation of the azimuthal angle of a linearly polarized input light beam by glucose.

Figure 3.10 is a MATLAB® generated simulation of the effects of linear birefringence. This is confirmed experimentally in Figure 3.11 for a birefringent glass eye-coupling device. The birefringence values used for the simulation are within the range based on the measured refractive index variations available in literature for the fast and slow axes of rabbit cornea.[108] As measured, $(\eta_o - \eta_e)$ varies within the range of 0-5.5 x 10^{-03}, thus causing a net change in the retardance, δ, experienced by a propagating linearly polarized light beam which traverses a corneal thickness, *t*; as a function of its wavelength, λ, where

$$\delta = \frac{2\pi \cdot t}{\lambda}(\eta_o - \eta_e). \tag{3.9}$$

Figures 3.10 and 3.11 substantiate the changes of a horizontal linear SOP into an elliptical SOP whose ellipticity changes with variations in the sample birefringence when the input SOP is neither aligned with the slow or fast axis of birefringence, i.e. one of the principle axes. In Figure 3.11, the fast axis was aligned at 5° with respect to the horizontal linear input. Therefore, it can be assumed that the glass device has a birefringent effect similar to that of the location on a rabbit cornea that results in a net retardance,δ, of 101.5°, as depicted in Figure 3.10. It is worth noting that the documented range for corneal birefringence in human subjects is much smaller.[108] This suggests, that birefringence changes due to motion artifact will have less of a confounding affect on glucose measurements in human subjects.

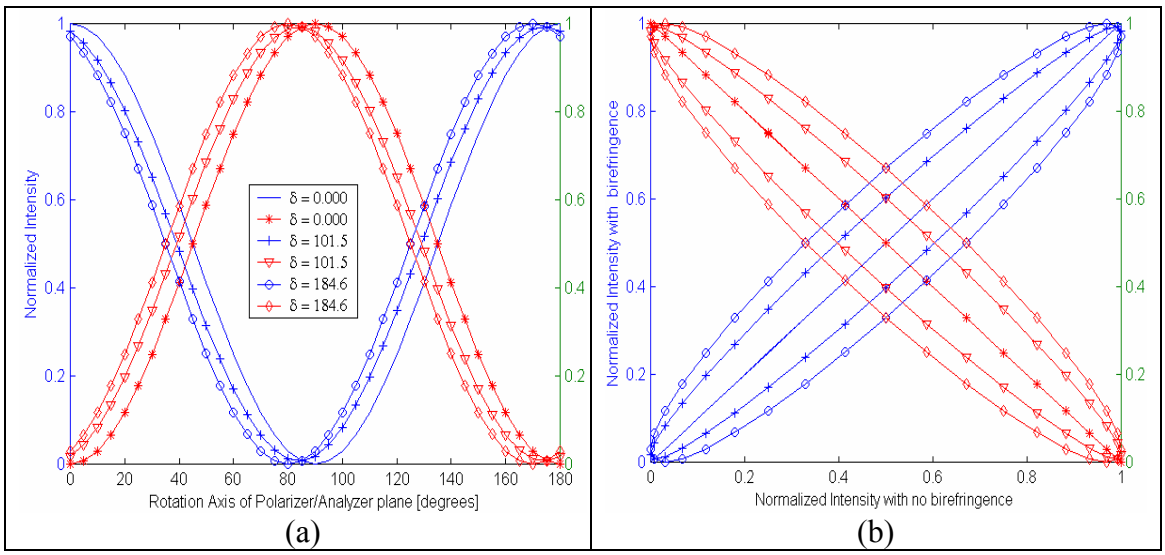

Figure 3.10: These MATLAB derived simulations illustrate the effect of changing birefringence, (η_o - η_e), on the detected intensities for H and V polarization state detectors. These plots were derived by rotating the analyzers with respect to the polarizer to determine the effect of a birefringent sample placed in between them. (a) For a linear horizontal (H) polarization input, both the aligned polarization (H-blue) and perpendicular, vertical (V-red), polarization detected intensities vary sinusoidally as the polarizer/analyzer plane is rotated through 180°. It is evident that birefringence has the affect of introducing a phase shift and a change in the magnitude of the detected intensities. (b) This plot, which was produced by plotting the detected intensities for each detector versus the normalized theoretical detection intensity for a polarizer/analyzer combination without a sample, shows the conversion of the linear polarization into elliptical polarization states of varying ellipticity and azimuthal angle of the major axis as birefringence changes.

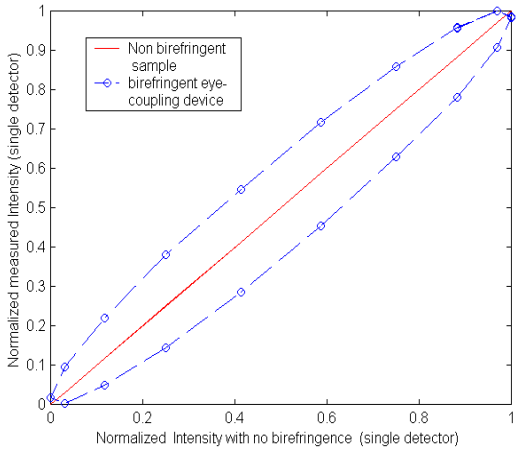

Figure 3.11: This is the experimental result obtained from a birefringent eye-coupling device, using a single detector. These results demonstrate the conversion of a linear input SOP into an elliptical SOP as a result of linear bire-fringence and matches the simulated case for δ=101.5° in Figures 3.10 (a) and (b).

For *in vivo* glucose measurements, the cornea is subject to motion during respiration as a result of pressure changes in the nasal cavity, which is connected to the eye orbital cavity, thus, the variation of birefringence over the corneal surface interferes with the glucose measurement. In order to develop a suitable solution, there is a need to determine the degree to which this affects the glucose measurements.

3.3 Phenomenological Measurement Approach

3.3.1 *Assumptions of Methodology*

The stated goal is to successfully recreate and measure the affect of a moving eyeball on an incident polarized light beam due to corneal birefringence variations using an intact excised rabbit eyeball. For the proposed method, several assumptions have to hold:

1. Minimal scattering of light by the eyeball cornea such that the polarization and intensity of the probing light beam is not changed. This is a reasonable assumption because the eyeball is transparent to visible light.

2. The interactions of the polarized light with the eyeball are linear. This is a reasonable assumption because the total intensity of the light at the eyeball is in nanowatts, therefore, not sufficiently strong enough to generate noticeable nonlinear effects.

3. The effects of absorption and dichroism are homogenous throughout the beam path across the eye and any relative changes in the state of the polarized beam are due only to variations in corneal birefringence.[109] It is important to note that for this study, it is not necessary for the path length of the individual rays, which represent different corneal positions for an incident point source laser beam in the *in vivo* experiments, to be constant; nor is necessary for the corneal thickness to be uniform. The magnitude of relative changes is the goal of this study and not the quantification of the actual birefringence and fast axis location. This method is not sufficient to accomplish the later goal.

4. The use of saline solution for refractive index matching of the cornea enables the rays of the light beam to propagate with extremely little or no refraction;[110] therefore, each input and output ray combination completely mimics a location on the eyeball for the narrow: pencil beam size, laser input for the *in vivo* glucose polarimetric system. This assumption is reasonable based on the analysis of Cameron[110] that indicates minimal refraction of the input beam for the saline solution coupled system.

5. The affect of reflections off the surfaces of the glass eye holder, and the cornea are minimal and do not appreciable change the SOP of the input beam. For the *in vivo* system, this is not an issue because any loses due to reflection do not noticeably affect the SNR for a linearly polarized incident beam. In the imaging system, this can become an issue, because the process of measuring the birefringence and fast axis locations requires using SOPs that are affected by reflection due to helicity. This can create some depolarization in certain cases, therefore, resulting in error in the Mueller matrix computations. Computing the Mueller matrix of the empty sample cell holder with saline and no eyeball, and using this to remove the sample cell holder effect, will still not account for the reflections off both input and output sides of the cornea and the possible light reflection oscillations this generates within the sample cell holder. This is an inherent problem of this method, only when correlating the results to the *in vivo* system. Since this study considers only the relative changes, the results still provide a reasonable picture for the *in vivo* system.

6. The birefringence of the cornea can be modeled by a linear retarder.

3.3.2 *Methodology*

The Mueller matrix is a mathematical representation of the optical polarization properties of any given sample.[111] In order to experimentally measure the Mueller matrix for an unknown sample, a minimum of 16-independent polarization images are required.

For this report, we use 36 polarization images to generate the 16-element Mueller matrix (Figure 3.12), the benefit being less noise in the computed matrix,[112] and normalize by the M_{11} element. We can map the apparent relative birefringence of the eye and the apparent position of the fast axis, i.e. as seen by our light-coupling geometry, by utilizing certain elements of the Mueller matrix, e.g. M_{43} and M_{44} elements of Table 2.3(b). From Eqns. 3.10 through 3.14, the birefringence, η_o - η_e, is related to the retardance in the M_{44} component, δ in Eqn. 3.10, as a function of the sample length, l, and the wavelength of the propagating light beam, λ. Once δ is computed from the M_{44} component using Eqn 3.11, then the location of the fast axis, ϕ, can be computed using the M_{43}, M_{34}, M_{24}, and M_{42} components using Eqns. 3.11-3.14 respectively. We utilize a MATLAB program to compute these values for each pixel of the image.

$$\cos(\delta) = \mathrm{M}_{44} = \mathrm{RR} - \mathrm{RL} - \mathrm{LR} + \mathrm{LL} \tag{3.10}$$

$$-\cos(2\rho)\cdot\sin(\delta) = \mathrm{M}_{43} = \mathrm{PR} - \mathrm{PL} - \mathrm{MR} + \mathrm{ML} \tag{3.11}$$

$$\cos(2\rho)\cdot\sin(\delta) = \mathrm{M}_{34} = \mathrm{RP} - \mathrm{RM} - \mathrm{LP} + \mathrm{LM} \tag{3.12}$$

$$-\sin(2\rho)\cdot\sin(\delta) = \mathrm{M}_{24} = \mathrm{RH} - \mathrm{RV} - \mathrm{LH} + \mathrm{LV} \tag{3.13}$$

$$\sin(2\rho)\cdot\sin(\delta) = \mathrm{M}_{42} = \mathrm{HR} - \mathrm{HL} - \mathrm{VR} + \mathrm{VL} \tag{3.14}$$

Note: this approach assumes that the eyeball is a non-depolarizing anisotropic sample

3.4 Materials and Methods

3.4.1 *System Setup*

The optical polarimetric imaging system, shown in Figure 3.12, contains 4 electro-optical liquid crystal devices, which are used in conjunction with two fixed polarizers, to set the input, and output polarization states used for deriving the 16-element Mueller Matrix. As depicted in Figure (4), the output beam from a white light source, component (1), (Navitar, Rochester, NY) passes through a red 635nm filter (Melles Griot Electro-optics, Boulder, CO) coupled with a collimating lens, component (2), (Newport Corporation, Fountain Valley, CA) before being linearly polarized, oriented at +45 ° (P-state), by a Glan Thompson 100,000:1 polarizer, component (3), (Newport Corporation,

Fountain Valley, CA). The ensuing P-state polarized beam passes through an electro-optical variable polarization rotator, component (4), and a variable retarder, component (5), (Meadowlark Optics, Frederick, Colorado) that are used to produce the different input polarization states necessary for imaging the rabbit cornea, component (7). The lens, component (6), expands the beam to cover the whole corneal surface. The traversing beam then propagates through the detection optical train, components (8)-(10), which consist of the same components as in the input optical train but in reverse order, with the polarizer, component (10) set at -45 ° (M-state), before being imaged by a 14 bit, 509×511, TE-cooled CCD camera (Apogee, Auburn, CA). For further details of the automated Mueller matrix imaging system used, the reader is referred to an earlier publication (reference 112). The data presented in the results section was collected on a rabbit eyeball within 24 hours of excision; using 10 Mueller matrix imaging runs.

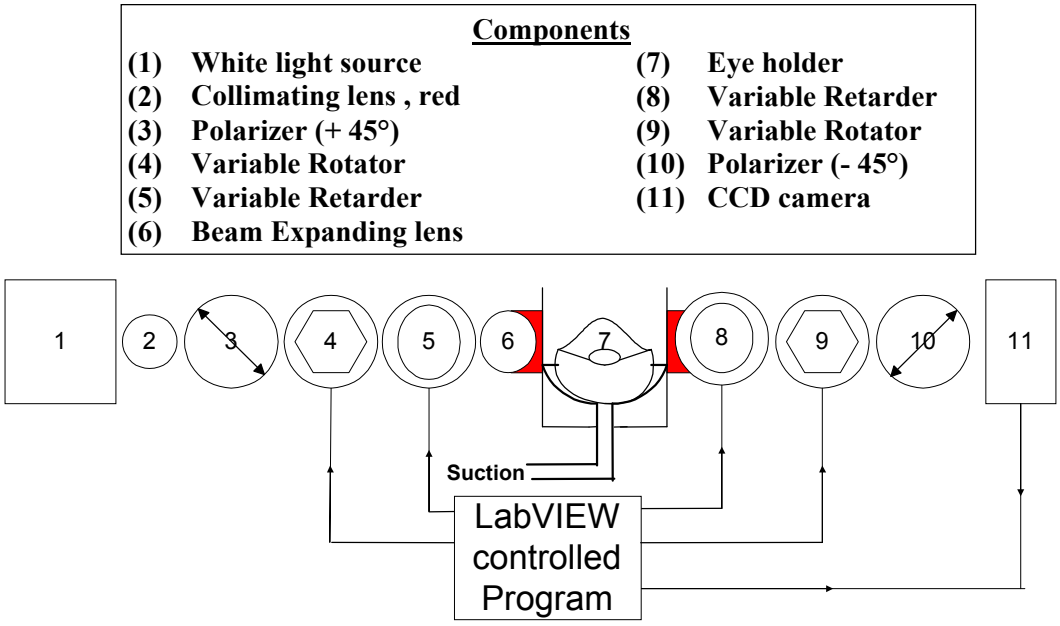

Figure 3.12: Block diagram of experimental setup.

3.4.2 *System Calibration*[t]

The system was calibrated for air, and then checked for known polarizer and QWP sample orientations. In Table 3.4, only the QWP results for a vertical fast axis orientation are presented. However, Figure 3.12 does contain the results for the fast axis orientations from –90° to 90°, investigated in 10° increments.

3.5 Results and Discussion

3.5.1 *System Calibration Results*

Table 3.4: Mueller matrix imaging system calibration results for different polarizer sample orientations, and for a QWP oriented with a vertical fast axis.[u]

SAMPLE	RESULTS	
	EXPERIMENT	THEORY
AIR	$\begin{bmatrix} 1 & 0.008 & -0.004 & -0.001 \\ 0.028 & 0.975 & 0.003 & 0.001 \\ 0.008 & -0.031 & 0.989 & 0.013 \\ -0.006 & 0.010 & 0.005 & 0.943 \end{bmatrix}$	$\begin{bmatrix} 1 & 0 & 0 & 0 \\ 0 & 1 & 0 & 0 \\ 0 & 0 & 1 & 0 \\ 0 & 0 & 0 & 1 \end{bmatrix}$
H-Polarizer	$\begin{bmatrix} 1 & 0.966 & 0.018 & -0.002 \\ 1.001 & 0.965 & 0.018 & -0.001 \\ 0.020 & 0.019 & -0.002 & -0.013 \\ -0.010 & -0.010 & -0.003 & 0.007 \end{bmatrix}$	$\begin{bmatrix} 1 & 1 & 0 & 0 \\ 1 & 1 & 0 & 0 \\ 0 & 0 & 0 & 0 \\ 0 & 0 & 0 & 0 \end{bmatrix}$
V- Polarizer	$\begin{bmatrix} 1 & -0.998 & -0.013 & 0.006 \\ -0.998 & 0.995 & 0.013 & -0.006 \\ -0.029 & 0.029 & -0.003 & 0.002 \\ 0.015 & -0.015 & -0.002 & 0.000 \end{bmatrix}$	$\begin{bmatrix} 1 & -1 & 0 & 0 \\ -1 & 1 & 0 & 0 \\ 0 & 0 & 0 & 0 \\ 0 & 0 & 0 & 0 \end{bmatrix}$

[t] The system characterization results are presented in Table I-1a of Appendix I. When compared to the ideal values in Table I-1b, these results indicate that the system possesses some residual error after calibration, which enables the generation of slightly non- realizable matrices as discussed earlier in Section 2.6.5.

[u] The standard deviation results for these samples are presented in Table I-2 of Appendix I.

Table 3.4: Continued.

SAMPLE	RESULTS	
	EXPERIMENT	THEORY
P- Polarizer	$\begin{bmatrix} 1 & -0.025 & 0.997 & -0.193 \\ -0.019 & -0.005 & -0.008 & 0.015 \\ 1.022 & -0.037 & 0.995 & -0.020 \\ 0.004 & -0.002 & 0.011 & 0.018 \end{bmatrix}$	$\begin{bmatrix} 1 & 0 & 1 & 0 \\ 0 & 0 & 0 & 0 \\ 1 & 0 & 1 & 0 \\ 0 & 0 & 0 & 0 \end{bmatrix}$
M- Polarizer	$\begin{bmatrix} 1 & 0.028 & -1.013 & 0.201 \\ 0.016 & 0.008 & -0.017 & -0.008 \\ -0.990 & -0.028 & 0.998 & -0.022 \\ -0.004 & 0.004 & 0.006 & -0.016 \end{bmatrix}$	$\begin{bmatrix} 1 & 0 & -1 & 0 \\ 0 & 0 & 0 & 0 \\ -1 & 0 & 1 & 0 \\ 0 & 0 & 0 & 0 \end{bmatrix}$
QWP-V	$\begin{bmatrix} 1 & -0.002 & -0.003 & -0.004 \\ 0.018 & 0.976 & -0.022 & -0.032 \\ 0.106 & -0.203 & 0.079 & -0.997 \\ 0.001 & 0.019 & 1.002 & 0.215 \end{bmatrix}$	$\begin{bmatrix} 1 & 0 & 0 & 0 \\ 0 & 1 & 0 & 0 \\ 0 & 0 & 0 & -1 \\ 0 & 0 & 1 & 0 \end{bmatrix}$

The results, presented in Table 3.4, indicate that the system does not have sufficient accuracy and sensitivity to enable the absolute quantification of birefringence and fast axis location. Notwithstanding, the results will be very useful qualitatively, in determining how much of a variation the *in vivo* glucose detection system laser will see due to motion artifact as the eyeball changes its position.

The results in Figure 3.13 indicate an angular dependence of retardance, which should not be the case for a pure QWP sample imaged at normal incidence. Furthermore, these variations exceed what would be considered reasonable for slightly off normal incidence. A careful analysis of this angular dependence produced the following 4th order polynomial model:

$$y = -(8\times10^{-09})x^4 + (2\times10^{-08})x3 + (0.0001)x^2 - (0.0002)x - 0.1385; \quad r^2 = 0.966 \qquad (3.15)$$

where M_{44} is represented by 'y' in this model.

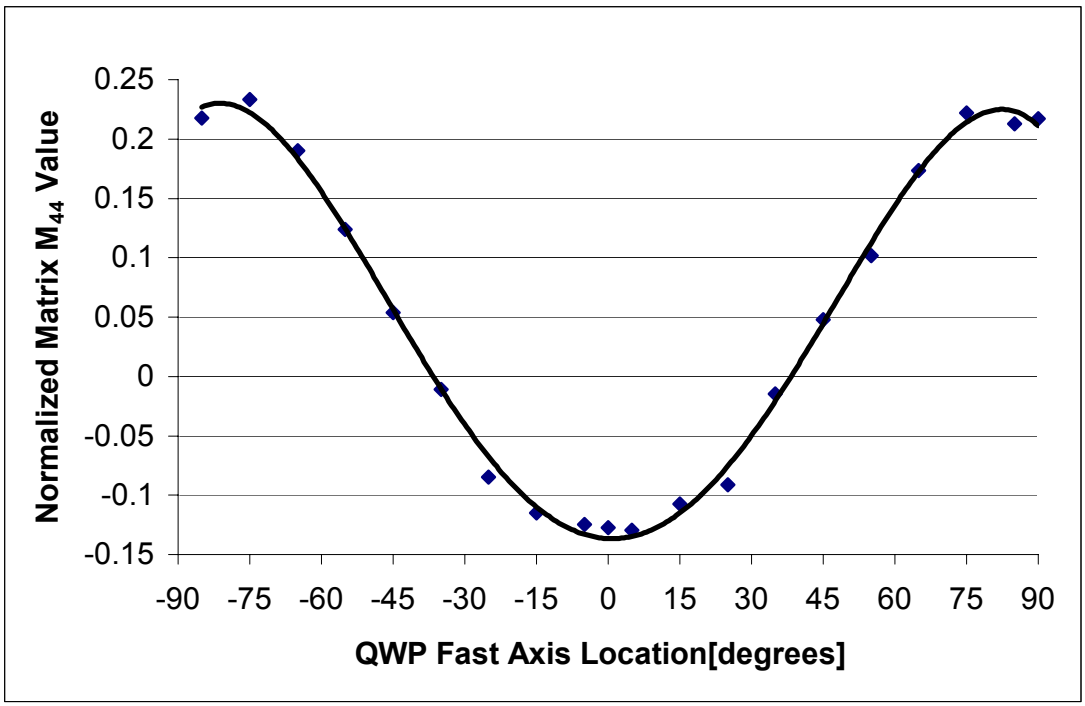

Figure 3.13: Calibration results for the M_{44} component, retardance measurement, of a QWP sample as the fast axis angle is rotated through 180 degrees.

Upon further investigation, it was discovered that the graph in Figure 3.13 can essentially be reproduced by plotting the following relationship [$tan(M_{44})/cos(M_{44})$] versus the QWP fast axis location. Considering small angle approximation, this relationship then reduces back to M_{44}, thus, suggesting that the M_{44} value variations with fast axis location are equivalent to very small radian angle changes. Though this analysis did not solve the systemic angular dependence on the fast axis position of a birefringent sample, it did, however, shed some light on the nature of the variations.

3.5.2 *System Modeling Results*

A program was written in MATLAB® 5.3 to investigate how the computed fast axis location changes as a function of actual fast axis position. Figure 3.14(a) is a plot of the computed fast axis location based on Eqns. 3.10 through 3.14. This indicates that the model equations cannot uniquely resolve angles greater than 90º.

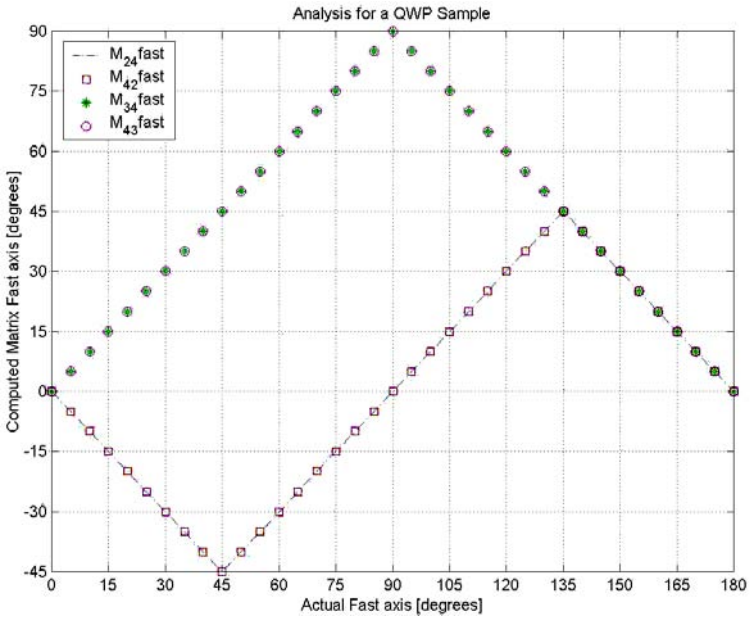

(a)

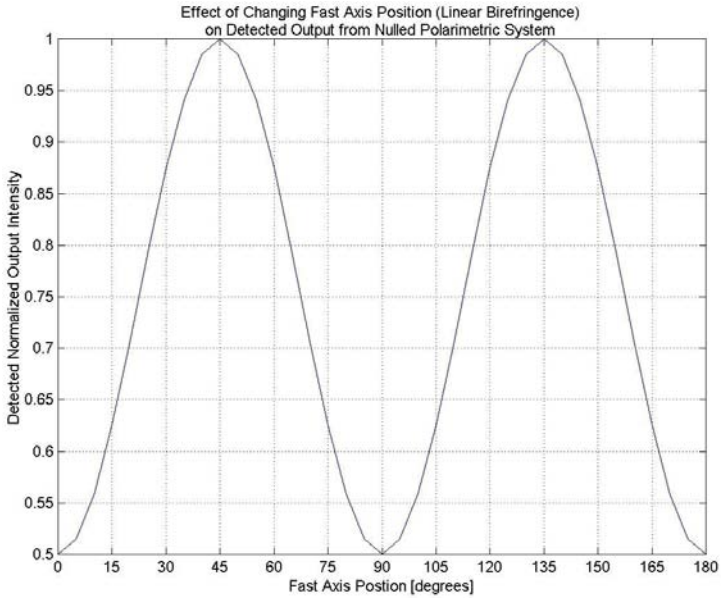

(b)

Figure 3.14: Plots indicating the response of the analytical model for Fast Axis Position in (a) the theoretical model using Eqns. 3.10-3.14 and (b) the aqueous humor polarimetric *in vivo* glucose detection system.[v]

[v] The results used to derive this figure are presented in Table I-3 of Appendix I.

Figure 3.14(b) was generated based on Eqn. 3.16,

$$\begin{bmatrix} a-b \\ \mp e \pm f \\ 0 \\ 0 \end{bmatrix} = \begin{bmatrix} 1 & \mp 1 & 0 & 0 \\ \mp 1 & 1 & 0 & 0 \\ 0 & 0 & 0 & 0 \\ 0 & 0 & 0 & 0 \end{bmatrix} \begin{bmatrix} a & b & c & d \\ e & f & g & h \\ i & j & k & l \\ m & n & o & p \end{bmatrix} \begin{bmatrix} 1 \\ \pm 1 \\ 0 \\ 0 \end{bmatrix}$$

Output — Analyzer (90 degrees to Input) — Birefringent Eyeball — Input

for the nulled *in vivo* system, the input is linearly polarized H or V, therefore, yielding the following relationships:

$$a = 1;\ b = e = 0;\ f = \cos(4\rho)\sin^2(\delta/2)+\cos^2(\delta/2), \qquad (3.16)$$

which can be used to compute the output from the nulled polarimetric *in vivo* glucose detection system. The plot indicates that once the fast axis angle exceeds 90º the affect on the system reverses itself, i.e. it is a recursive sinusoidal function, therefore, any angle (90º + theta) has the same affect on the system as the angle (90º - theta). As such the inability to resolve angles greater than 90º based on the Mueller matrix model equations is not a problem in the context of the experimental implementation.

Additionally, the range of published birefringence values for rabbit cornea was used to investigate the amount of retardation that would be expected experimentally.[108] Figure 3.15 is a linear plot of the retardance due to published rabbit corneal birefringence values. From the plot the value for retardance is seen to vary as high as 126º. However, recalling the 90º max retardance limitation of the nulled *in vivo* system, 90º should be the expected maximum retardation encountered by the input light beam.

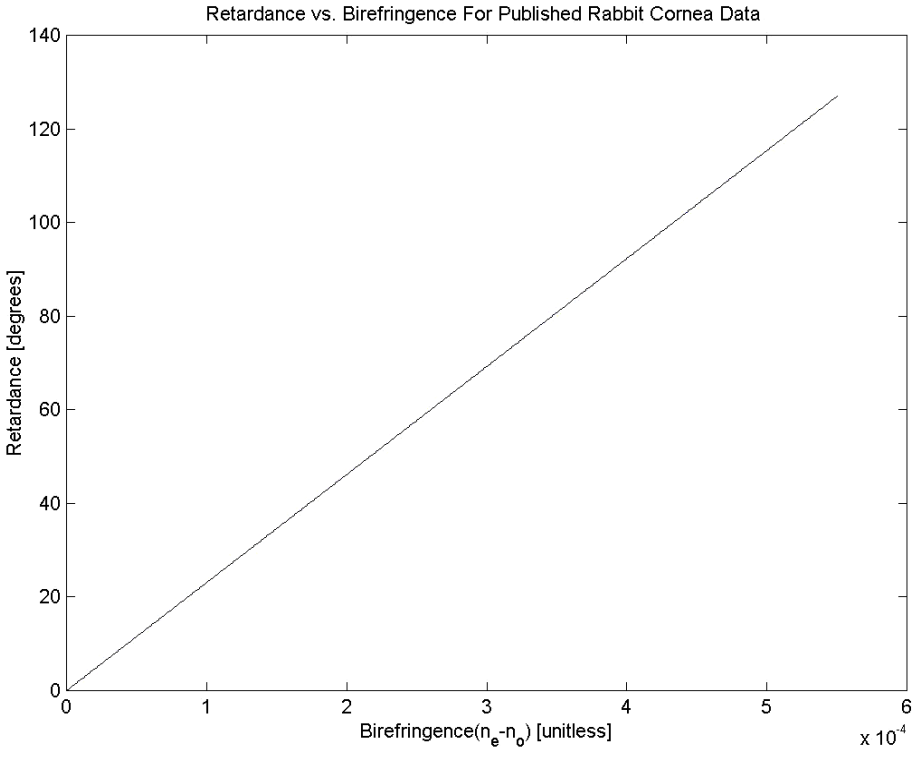

Figure 3.15: Plot of Retardance versus birefringence based on published values for rabbit cornea (reference 108).

3.5.3 *System Precision Results*

The precision of the system was computed by taking the standard deviation for each pixel across 10 repetitions (images) from the Figure 3.16 subplots (b) and (d). Based on these, the retardance value can be determined within ±2.7º and the fast axis location within ±1.1º. There are noteworthy: greater than system variability in Figures (b) and (d), changes in the apparent relative corneal retardance and in the apparent relative location of the fast axis of corneal birefringence as seen in Figures (a) and (c).

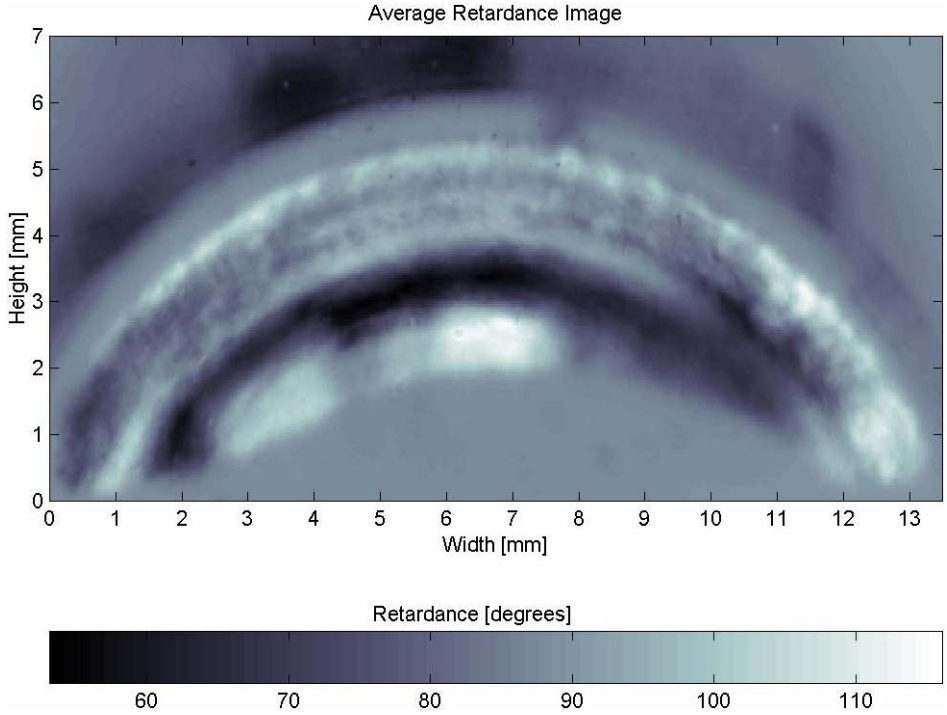

(a)

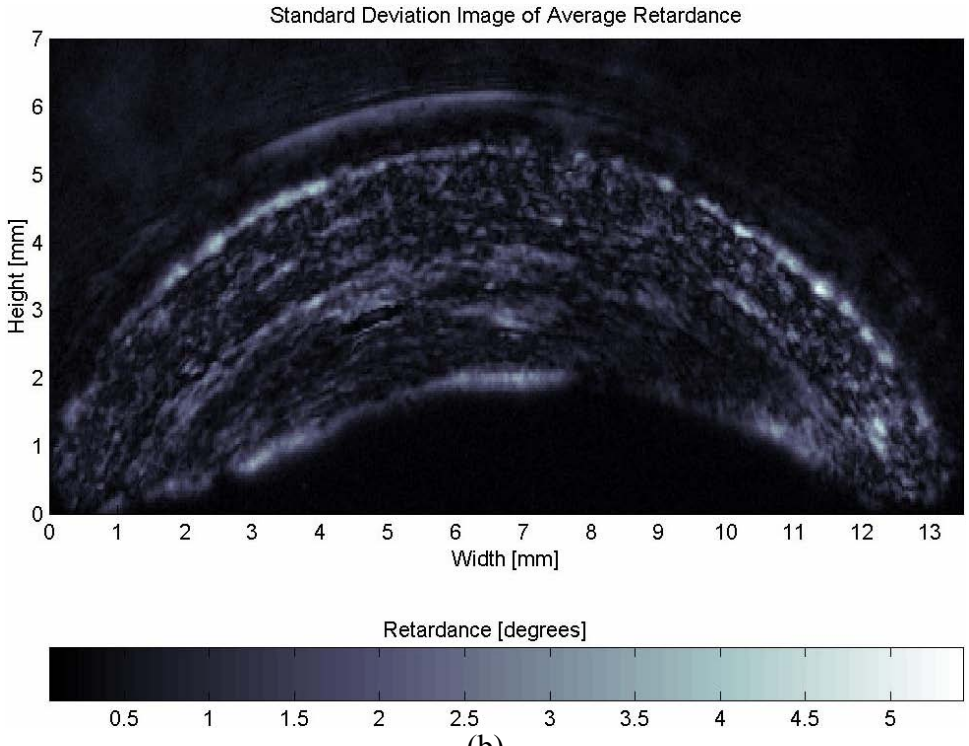

(b)

Figure 3.16: Corneal map results computed from ten repetitions for (a) average apparent retardance, (b) standard deviation of average apparent retardance image.

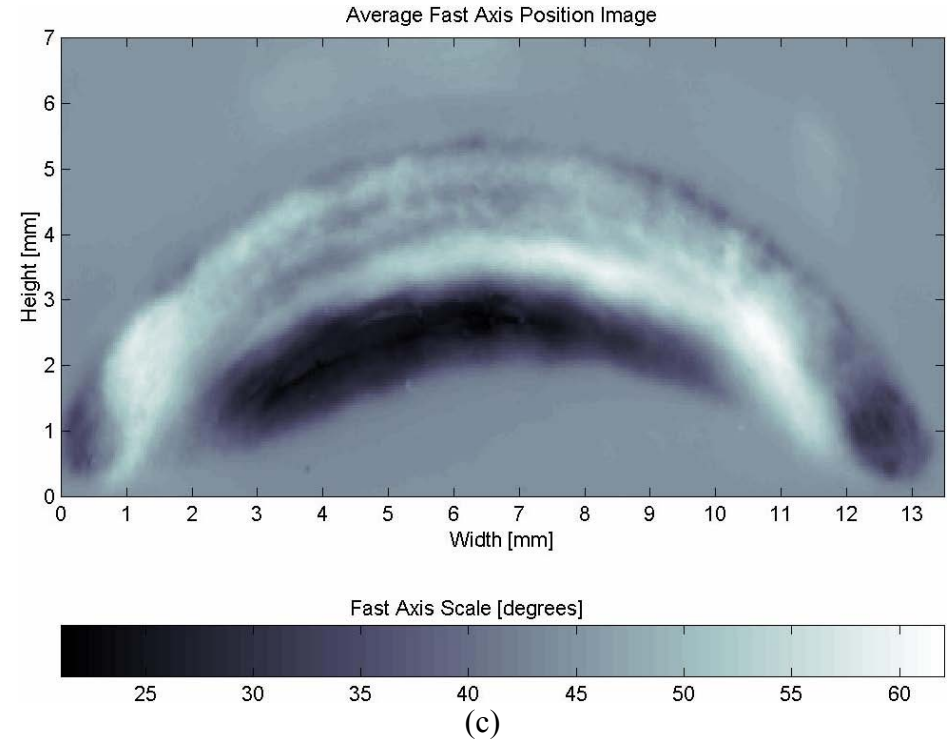

(c)

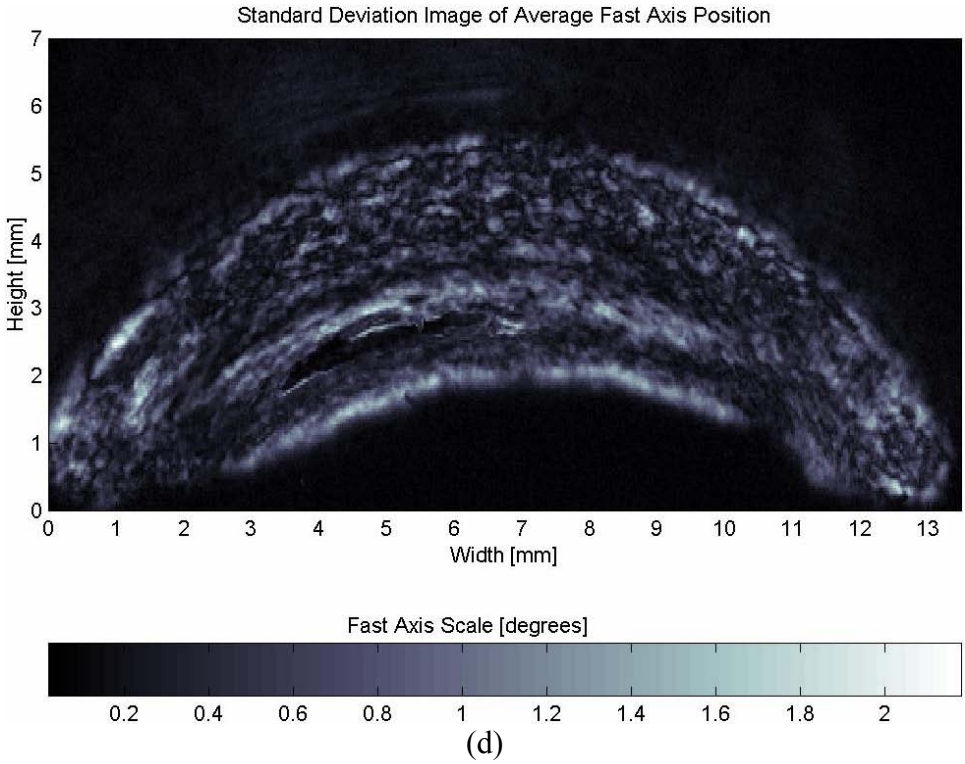

(d)

Figure 3.16: Continued; (c) average apparent fast axis position (the zero degree reference) is the standard positive x-axis). and (d) standard deviation of average apparent fast axis position image

3.5.4 *Experimental Results*

Figure 3.17 (a) represents the sample Mueller matrix and (b) is the raw white light image of the cornea. Recalling the results presented in Table 2.5 for the eight dielectric optical properties for a non-depolarizing sample, from (a), it is evident that the sample possesses LB for both the V-H and the P-M planes, which correspond to Mueller matrix elements M_{34}-M_{43} and M_{24}-M_{42} respectively. The sample exhibits very little CD, Mueller matrix elements M_{41}-M_{14}, and very little LD, Mueller matrix elements M_{12}-M_{21} and M_{13}-M_{31}.

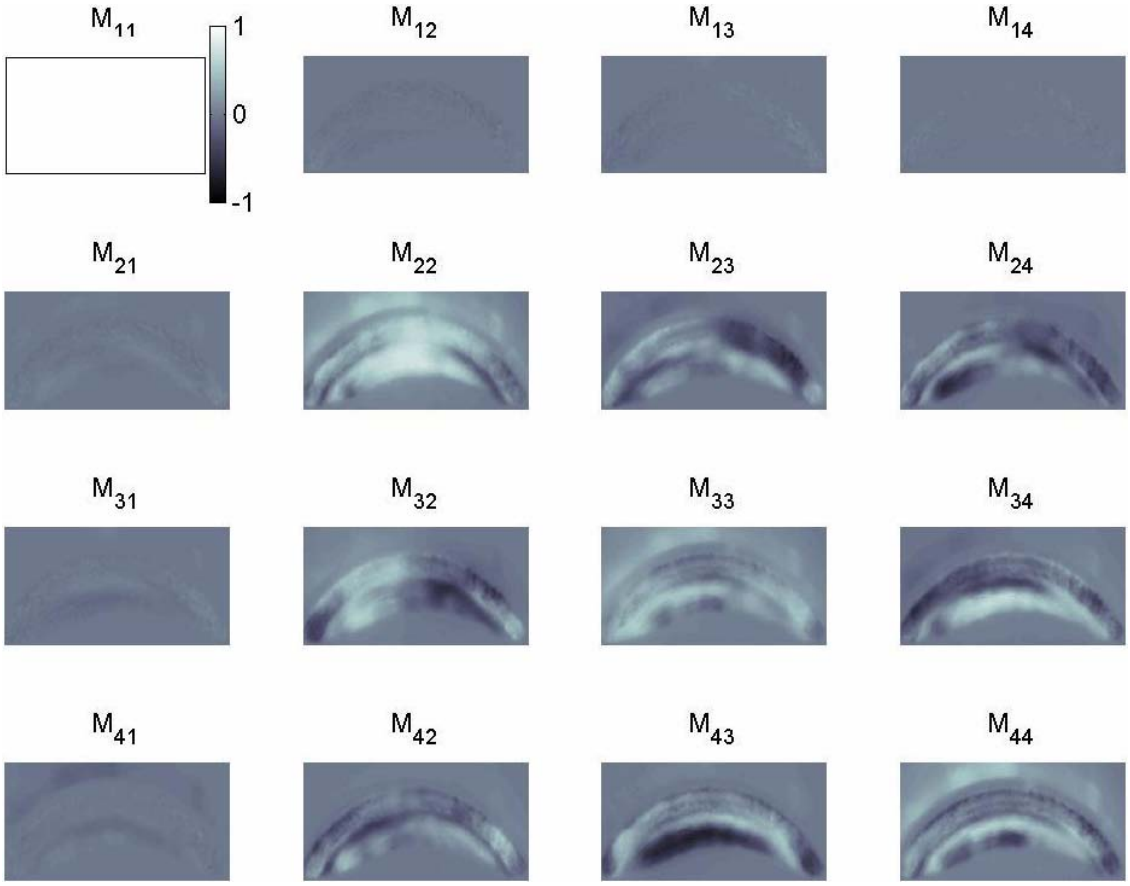

(a)

Figure 3.17: Experimental results for a rabbit eyeball collected within 6 hours of excision. Dimensions are width 13.5[mm] and height 5.25[mm].

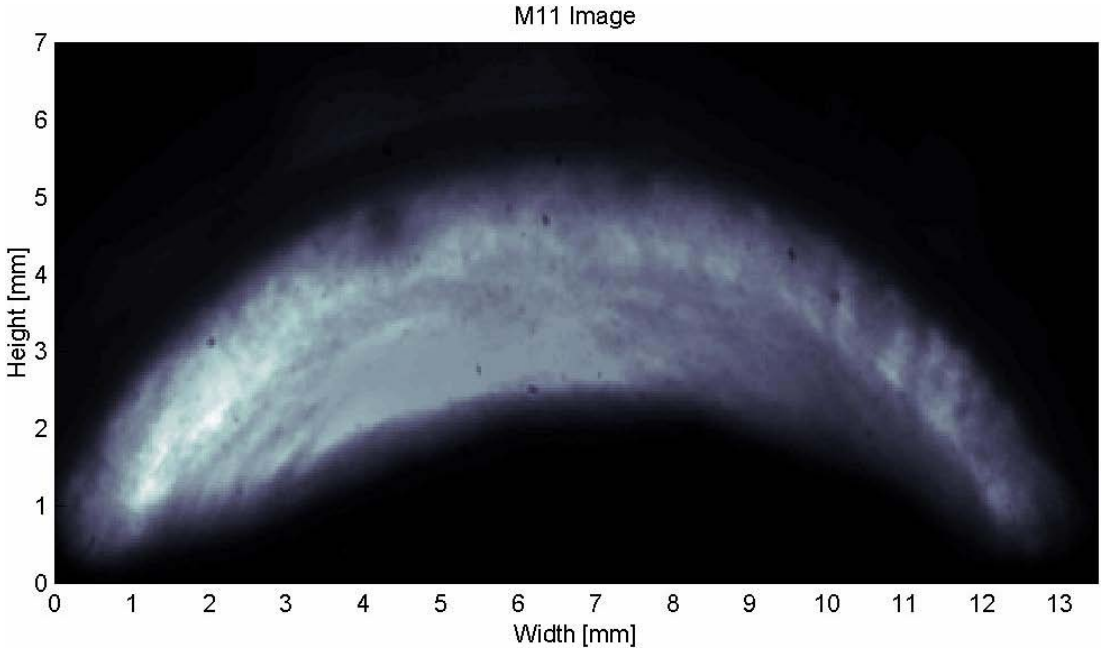

(b)

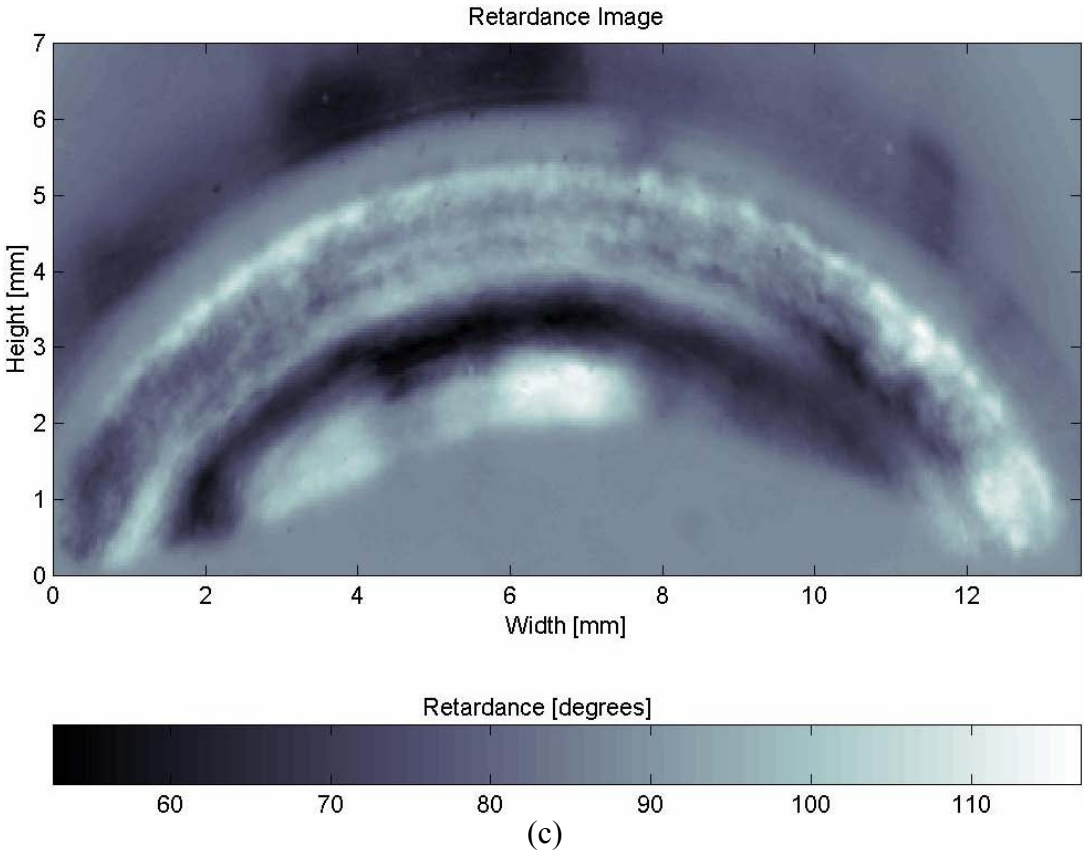

(c)

Figure 3.17: Continued.

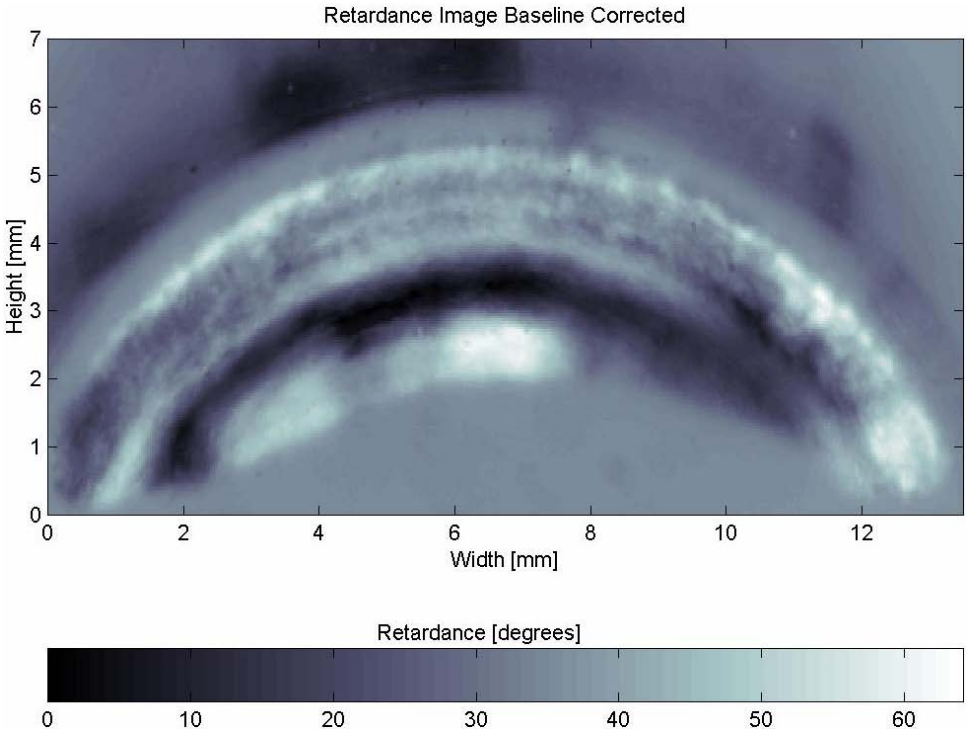

(d)

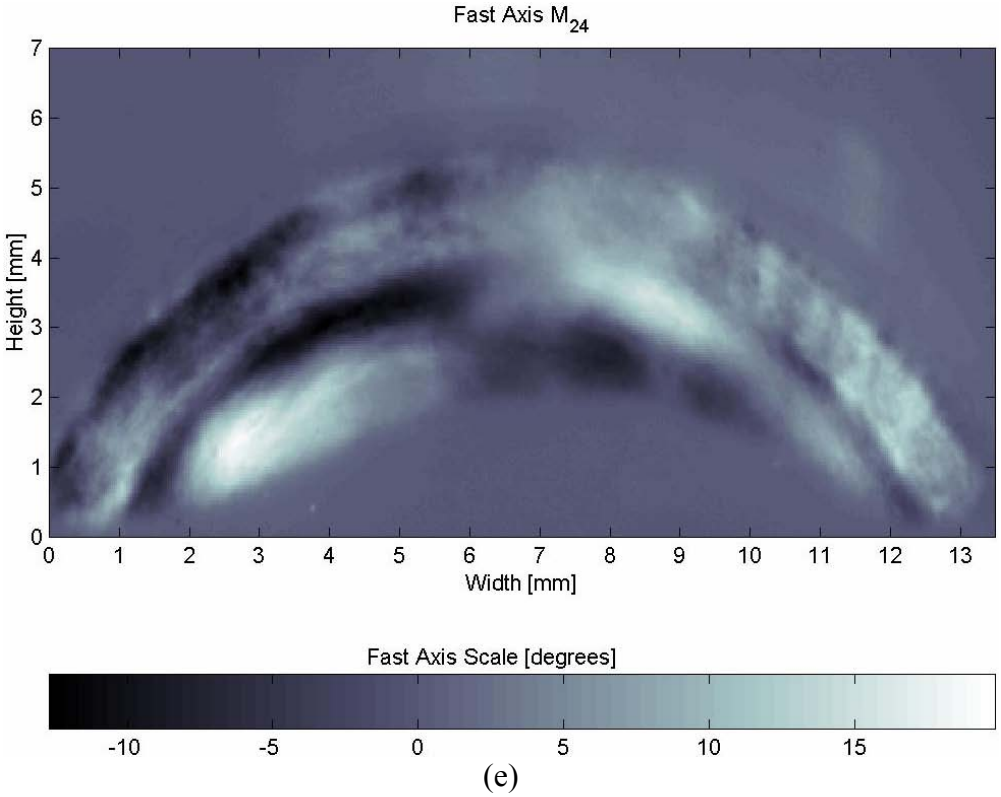

(e)

Figure 3.17: Continued.

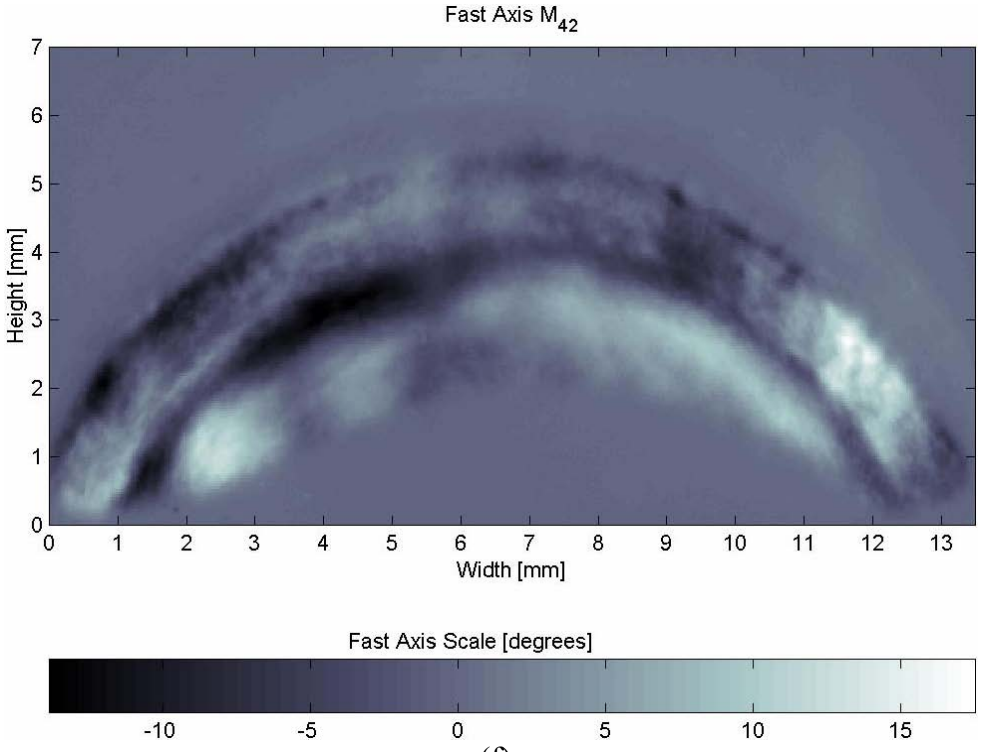

(f)

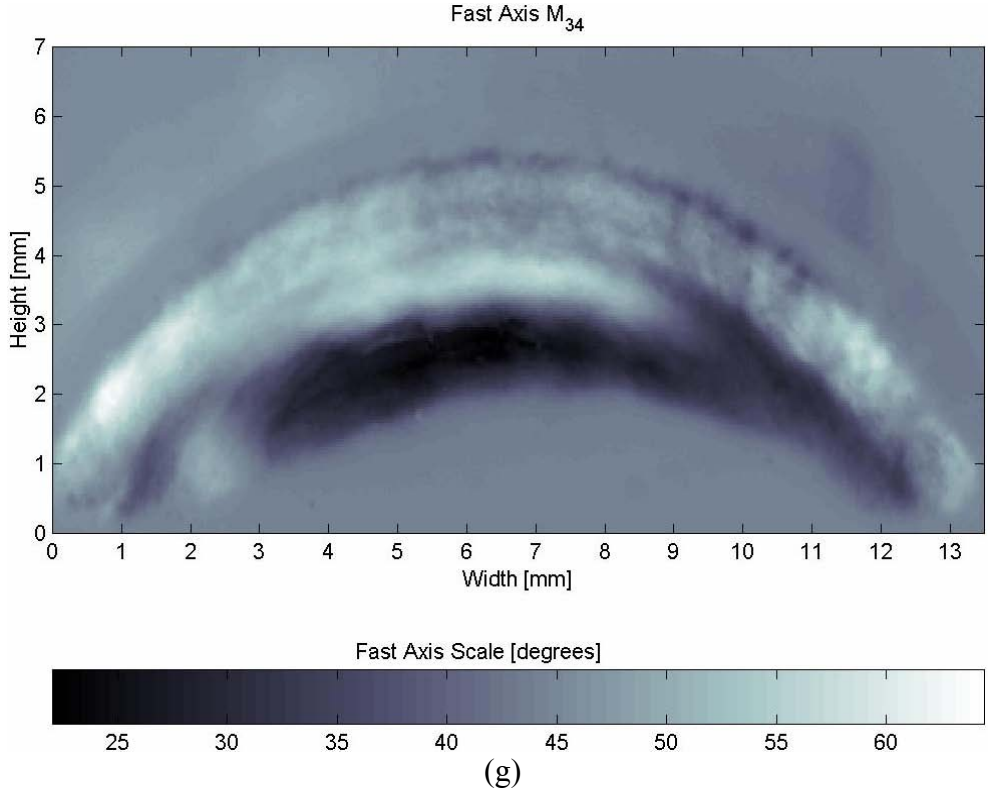

(g)

Figure 3.17: Continued.

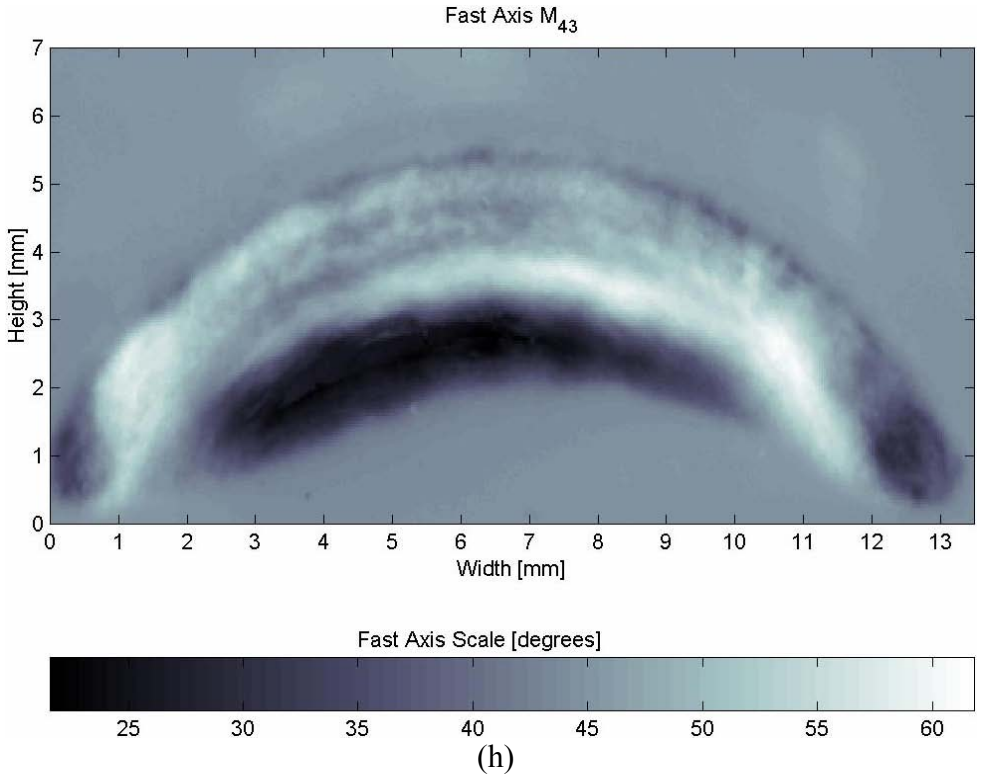

(h)

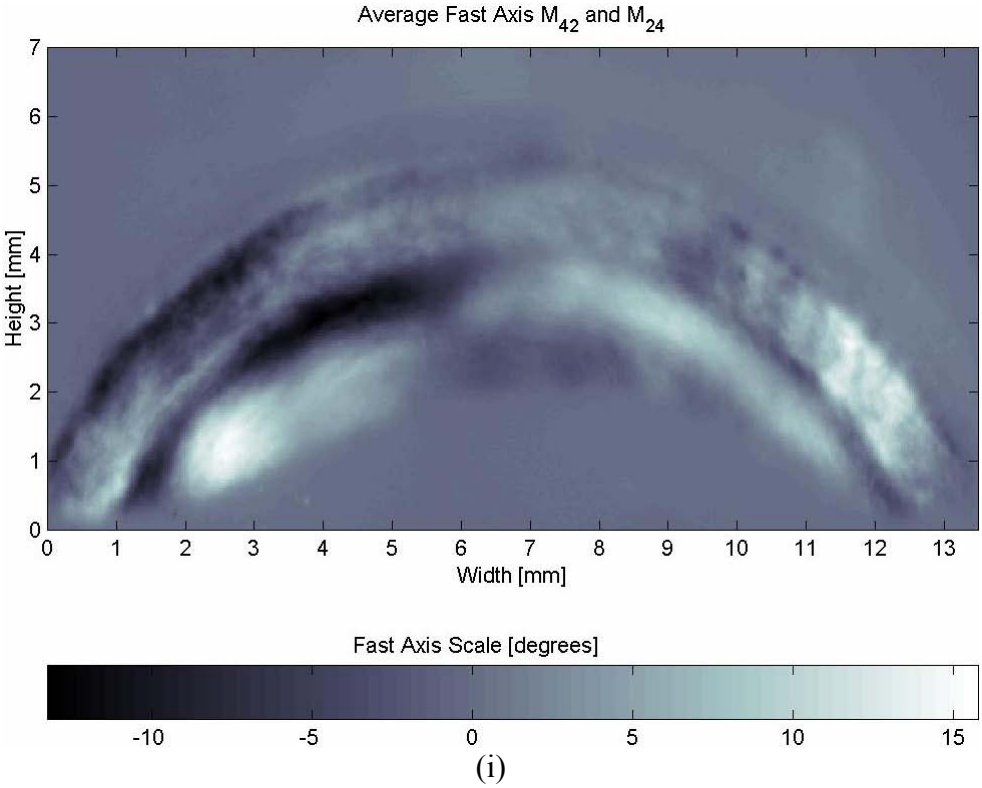

(i)

Figure 3.17: Continued.

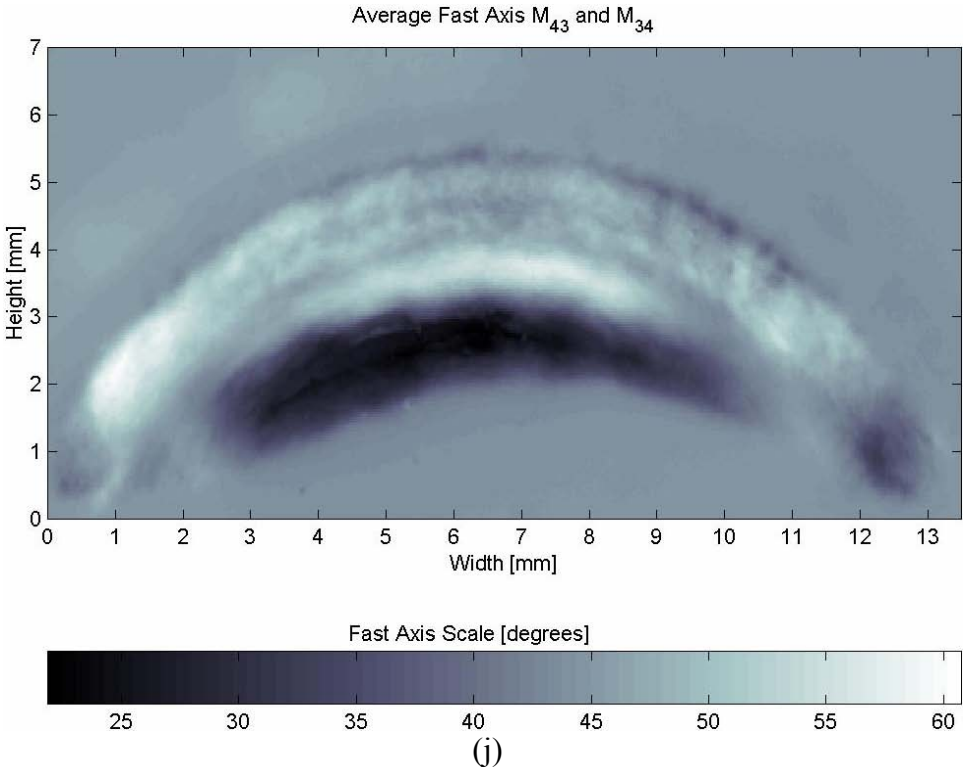

(j)

Figure 3.17: Continued.

The major results of importance to this study are reported in figures (e) through (m). Figure (c) and (d) demonstrate the affect of baseline correction on the retardation image. The baseline correction was done by subtracting out the minimum value of (c) from (d). The baseline correction essentially scales the observation to a start point of zero degrees, by removing the system background retardance offset, thus, confirming the system theoretical measurement limit of 90°, i.e. the actual maximum retardation measured did not exceed the theoretical limit of 90°. Figures (e) and (f) represent the fast axis position as determined based on the M_{24} and M_{42} components of the sample Mueller matrix. It is clear here that they are mirror images of each other as the theory suggests. Likewise, Figures (g) and (h) are also mirror images of each other based on their derivations from the M_{34} and M_{43} Mueller matrix components. The range of retardance values for (e) and (f) versus (g) and (h) shows almost a 1:2 ratio, which is also in agreement with the theoretical expectation based on Figure 3.14(a). Finally Figures (i)

and (j) are the average retardances based on averaging the two complementary derivations: averaging of M_{24} and M_{42} for (i) and the averaging of M_{34} and M_{43} for (j).

3.6 Conclusion

In this chapter the use of polarized light in the aqueous humor of the eye has been described as a potential means of non-invasively quantifying blood glucose levels. It has been shown that the time lag between blood and aqueous humor glucose levels is within five minutes, and that a system can be built that has the sensitivity to measure the milli-degree rotations observed for physiologic glucose concentrations. The information that we have garnered from the ORD characterizations of the other primary chiral components in the aqueous humor of the eye has shown that their contributions are potentially negligible. But, if necessary, the prediction errors for glucose can be improved considerably if a multi-wavelength system is utilized. Finally, by modeling and characterizing the effect of changing birefringence on our glucose measurements *in vivo*, this information will enable us to design and implement a closed loop multi-wavelength system that we anticipate will facilitate the accurate and repeatable measurement of glucose *in vivo*. It will be a challenging feat based on the many variations evidenced by the coloration of the figures, which indicates an effect of relative birefringence changes that produce a retardation of greater than 60º, which when factored into Eqn. 3.7, is a considerable glucose measurement artifact.

The retardance and fast axis position are seen to vary significantly as you travel from the corneal apex (at the top) to the lens (at the bottom). In this direction, a light beam would be seen to traverse many retardation and fast axis isochores. From side to side, however, the variations observed are very minimal, as the isochores primarily follow the cornea contour. For glucose monitoring it may make sense to keep the beam within a reasonable contour area or perhaps try different light profiles such as a laser line instead of the typical circular beam. Furthermore, due to expected variations in corneal birefringence between eyeballs,[113] it may be necessary to have a calibration system that takes into account the unique optical properties of the eyeball that is utilized. This can

potentially be done by scanning in the spatial distribution of the corneal birefringence and fast axis location and building a complex calibration model or incorporating a simultaneous imaging system to record the path of the probing light beam through the eye and accounting for this in the glucose measurement. Once, a reasonable sample of human eyeball cornea birefringence and fast axis position data is accumulated, it is possible that the noted variations will necessitate a combination of all of the aforementioned ideas to ensure a robust sensor.

CHAPTER IV
THE APPLICATION OF POLARIZED LIGHT FOR NON-STAINING CARDIOVASCULAR HISTOLOGY

Whereas birefringence is problematic for the polarimetric determination of glucose through the aqueous humor *in vivo*, birefringence is essential for polarization microscopy. In fact, birefringence is the basis for the contrast in some forms of polarization microscopy. The molecular structure of proteins, lacking a symmetry axis, makes them optically active and gives them inherent birefringence. In addition, their ordered arrangement in the cellular structures, such as is the case for muscle and collagen fibers, results in form birefringence.[114-117] Hence, this is the reason that polarization microscopy is very useful in imaging protein structures.

Having previously introduced the need for non-caustic tissue staining techniques in Chapter I, this chapter examines the basis for this and also introduces a polarization microscopy imaging technique that provides sufficient contrast for certain cardiac tissue biomechanical measurements, without requiring the use of staining. But first, the chapter will begin with a brief overview of the current histological techniques applied for studying cardiac tissue and the problems associated with these techniques. Then it will examine the theory behind the contrast enhancement of cardiac tissue due to polarization microscopy. Finally it will present the studies conducted using polarization microscopy to provide contrast for biomechanical measurements on cardiac tissues.

4.1 Overview of the Current Polarization Microscopy Tissue Preparation Histological Techniques

Amongst histologists, it is widely known and accepted that the process of sample preparation for analysis introduces measurement artifacts. Therefore, the goal of any histologist is to minimize and to know the exact measurement artifacts that they have introduced during the sample preparation process. Albeit this is easier said than done

because all sample preparation techniques introduce their own set of artifacts, which are sometimes unique.

4.1.1 *Tissue Sectioning for Histological Analysis*

The standard technique for tissue preparation for histological investigation typically involves chemical fixation: for sample preservation purposes, and mechanical stabilization: for providing rigidity to enable microtome sectioning of thin samples for viewing using microscopic techniques. Frequently, the sample is also stained to enhance the contrast of various tissue structures.

4.1.1.1 *Sample Chemical Fixation*

Current tissue preparation techniques for cardiac myofiber studies, involve utilizing Bouin's fluid to chemically fixate the sample.[64-66,118] Bouin's Fluid is a fixative used for routine procedures that contains formaldehyde: for cytoplasmic fixation, picric acid: for chromatin fixation, and glacial acetic acid. [119] The chemical fixation process prevents the lyses of the tissue by enzymes or bacteria, thus, preserving the physical structure for analysis. This process is accomplished by the action of formaldehyde or glutaraldehyde that are typically used because they react with the amine groups of tissue proteins and create crosslink bonds between the proteins, thus, effectuating the structural fixation of the tissue sample.[120]

4.1.1.2 *Sample Mechanical Stabilization*

For light microscopy studies, paraffin embedding is the preferred mechanical stabilization method. The process of paraffin embedding requires initially dehydrating the tissue, usually using concentration gradations of ethanol, then using xylene - which is miscible with paraffin, to remove any traces of alcohol. Dehydrating the tissue sample with a different chemical that is not miscible with paraffin prevents successful paraffin embedding. On the other hand, the process of treating the tissue sample for proper paraffin embedding, i.e. with xylene, absorbs the tissue lipids, thus, introducing systemic

artifacts, which prevent tissue lipid analysis. Other techniques such as the freezing microtome have been developed to prevent this chemically induced lipid artifact by freezing the sample, instead of using paraffin, for mechanical stabilization before slicing the sections. For paraffin embedded samples, after slicing the tissue, the sections are treated to remove the paraffin so that the tissues can be stained to enhance the various structures for imaging. Alternatively, frozen microtome sliced sections can be stained immediately on a glass slide and preserved by applying mounting media before applying the cover slide. The frozen microtome procedure, though relatively quick, introduces cracks in the tissue, thus, also creating its own set of systemic measurement artifacts.[120] Furthermore, though the preferred embedding method, paraffin embedding is not suitable for use when investigating myofiber sheet angles because it introduces systemic artifacts by distorting the fiber positions and alignments. Plastic embedding, with say JB-4 plastic, causes much less fiber position and alignment distortion but the JB-4 plastic is not removable from the sample to enable proper tissue staining because it cross links with the tissue structure. Therefore, using plastic embedding requires utilizing methods other than staining for tissue structure contrast enhancement. In situations where the tissue fiber position and alignment is the measured parameter, paraffin embedding is the least desired option for mechanical stabilization.[73]

4.1.2 *Health Risks Associated with the Techniques*

The chemicals contained in the fixative agent, Bouin's solution, and in the staining solutions are rather toxic. Some of the hazards for the constituents of Bouin's solution, as listed by OSHA's website,[121-124] are summarized in Table 4.1.

Table 4.1: A summary of some of the hazards associated with using Bouin's solution for staining and chemical fixating tissue samples.

CHEMICAL	HAZARDS
picric acid	Class A explosive agent: must be stored appropriately. *Health risks, short and long term due to exposure*: Skin irritant and sensitizer; Leads to cumulative liver, kidney, and red blood cell damage; Mutagenic leading to increased cancer risk: linked to lung, nasopharynx, oropharynx, and nasal passage cancers in humans; Prolonged exposure can lead to structural changes in human nose epithelial cells.
glacial acetic acid	*Health risks*: Exposure to fumes causes irritation of eyes, nose, throat, and skin; Prolonged exposure can lead to asthma and lung damage.
formaldehyde	*Health risks*: It is a suspect human carcinogen (carcinogenic); Accidental spill exposures have resulted in bronchitis or asthma.

4.1.3 *Sample Contrast Enhancement Techniques*

4.1.3.1 *Sample Staining Techniques*

Currently, most samples are stained to enhance the contrast of the structures of interest. There are many different staining techniques utilizing various chemical recipes of which a majority of them involve toxic chemicals. For cardiac tissue investigations, Picrosirius solution is used to enhance the sample collagen birefringence. The enhancement is facilitated by the bonding of Sirius Red dye elongated molecules with the collagen fibers such that their long axes are parallel with that of the collagen, therefore, enhancing the collagen form birefringence; typically 120 molecules of dye bind per collagen molecule.[64] The collagen form birefringence is discussed in greater detail in the upcoming Section 4.2.

4.1.3.2 *Non-Staining of Sample Techniques*

Cardiac tissues contain a large amount of ordered birefringent and optically active protein structures, and as such, they have long been studied by applying polarization microscopy to stained cardiac tissue sections. However, to our knowledge, it is only recently that polarization microscopy has been applied to image unstained cardiac tissues for the purpose of biomechanical measurements (Tower et al.).[88,125] For samples that are not stained, the structural contrast has to be enhanced by the imaging[126] and data analysis techniques.[127-129] The later parts of this chapter, present a polarization microscopy technique, which utilizes a data analysis algorithm that generates a polarization contrast enhancement, that is used to investigate birefringent collagen and muscle fibrous structures in cardiac tissue for the purpose of making biomechanical measurements.

4.2 Form Birefringence Theory

Inherent birefringence has been covered in depth in Chapter III, so this chapter will focus primarily on form birefringence, which is responsible for the majority of the polarization contrast in cardiac tissue polarization images. The form birefringence of the collagen myofibers in cardiac tissue provides the necessary polarization contrast to view the fibers embedded within a ground matrix and in clear plastic.

4.2.1 *Quantum-Mechanical Explanation for Form Birefringence*

From Section 3.2: Table 3.3, the arrangement of collagen fibers, as depicted in Figure 4.1, represents a uniaxial crystal with a vertical, z-axis, optic axis. Similar to the discussion in the preceding chapter, if the incident EM wave propagates in the direction of the long axes of the fibers, z-axes, the incident state of polarization (SOP) will be maintained. However, in this case unlike that of the preceding chapter, there will be significant absorption, evidenced by the off- white color of collagen fibers, but the asymmetric absorption will not have any affect in the x-y symmetry plane. If the sample is rotated or the incidence plane of the input EM field is rotated such that the beam no longer propagates along the optic axis, then the incident SOP will be changed as it traverses the fibers, thus, creating an elliptical SOP. Essentially form birefringence refers to the probing volume direction dependence of an EM wave for an arrangement of aligned anisotropic structures. For aligned anisotropic structures, the electric susceptibility, χ_e, 3×3 tensor is the average value across the probing volume direction. This value is relatively constant for probing directions aligned with the axis of the fiber alignments, i.e. the z-axis, regardless of the incident SOP. However, all other probing directions create variations in χ_e as a function of the incident SOP, which lead to the misalignment of the dipole moment with the polarization orientation of the incident E-field, thus, creating a non integer multiple of π retardation that leads to an elliptical SOP.[w]

---

[w] Note: if the incident field propagates perpendicular to the optic axis, z-axis, i.e. in the x-y plane say along the y-axis, and has a polarization orientation parallel to either the z-axis, or x-axis, it will retain its SOP, and there will be no birefringence effect because E_y =0 and either E_x =0 or E_y =0 respectively.

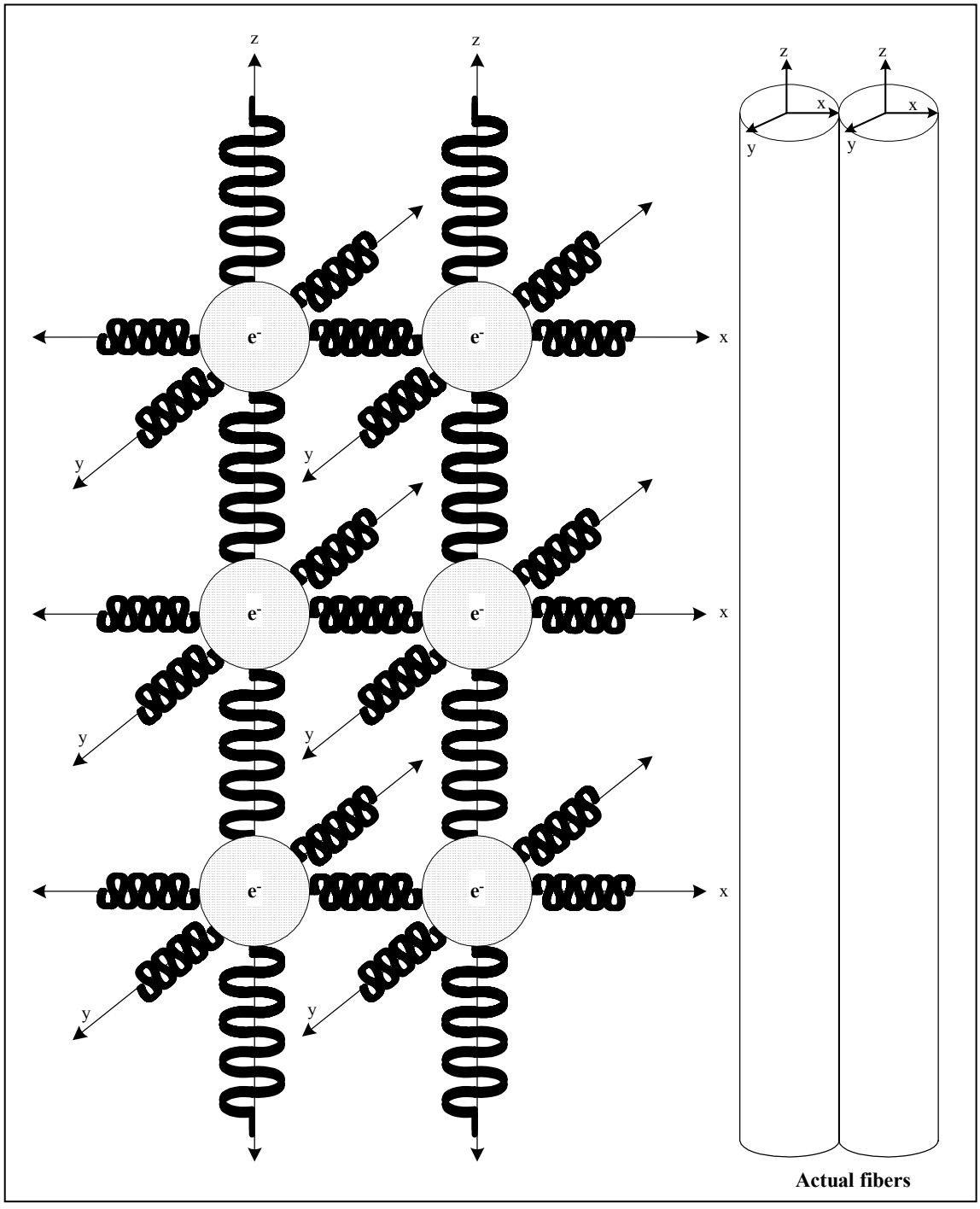

Figure 4.1: Illustration of form birefringence for aligned structures. The connected electrons represent protein molecules that possess symmetry in the x-y plane, i.e. the short axis, and have an optic axis aligned with the long axis, represented by the z-axis, of the fibers.

4.2.2 *Phenomenological Explanation for Form Birefringence*

Aligned asymmetric samples, such as collagen fibers, introduce phase retardation in the electric vector of linearly polarized light, when it does not travel along the alignment symmetry axis, which varies with the orientation of the incident SOP. As such an introduced phase change, due to form birefringence, converts the state of polarization of the incident light beam from linear to elliptical.

4.2.3 *Sources of Contrast for Polarization Microscopy*

Not all of the sources of polarizance discussed in Section 2.6.8.3 are sources of polarization contrast for this method. The numerical aperture of the light delivery microscope objective, which typically limits the angle of incidence to that much smaller than the Brewster's angle, inhibits polarizance due to Brewster's reflection. Polarizance due to the asymmetric refraction of light is not a factor because the inherent birefringence for biological tissues, i.e. due to the difference in the refractive index for the ordinary and extraordinary ray, is not large enough to create a physical separation of an incident ray into two orthogonally linear polarization states. However, the inherent birefringence does contribute to the polarization contrast in addition to scattering effects. If a biological sample is composed of structures with varying polarization anisotropies, then a polarization contrast image can be obtained that discriminates between the different structures. This is the basis for utilizing polarization microscopy to help elucidate biological structures.

4.2.3.1 *Inherent Birefringence Effects*

Inherent birefringence contributes to polarization contrast due to its affect of changing the input SOP, thus, highlighting birefringent structures within a crossed polarization image. For a nulled polarization imaging system, the introduction of a non-birefringent sample produces no image because the crossed polarized analyzer blocks all of the light backscattered from the sample. Conversely, the introduction of a birefringent sample will

yield a polarization image. This is illustrated and further explained in Figure 4.2 of Section 4.3.2.2.

4.2.3.2 *Optical Activity Effects*

Similar to the affect of a birefringent sample, an optically active sample will yield a polarization image in a nulled polarization system. Optical activity is due to a lack of an axis of symmetry at the molecular level, thus, generating a rotation of the azimuthal angle of linearly polarized light. The affect of optical activity in the polarization imaging system is to rotate the incident light such that it is no longer crossed polarized to the analyzer setting, therefore, yielding a bright illumination for the areas that posses this property. This is illustrated and further explained in Figure 4.3 of Section 4.3.2.2.

4.2.3.3 *Scattering Effects*

The polarizance effect of asymmetric scattering was discussed earlier in Section 2.6.8.3; this was primarily due to the Rayleigh scatter of the incident light by the structures much smaller than the wavelength. This polarizance effect also generates polarization contrast by enhancing or nulling the incident linear polarization state, therefore, showing up as brighter or darker regions respectively in a bright field polarization image.

4.3 Phenomenological Measurement Approach

4.3.1 *Assumptions of Methodology*

Since the objective of the application of this technique is qualitative and not quantitative, the only assumptions made is that the birefringence and optical activity of the protein structures of interest within the tissues that will be imaged, will be sufficiently large enough to provide adequate contrast to enable their elucidation.

4.3.2 *Methodology*

4.3.2.1 *Polarization Images*

Polarization images are acquired for a particular orientation of the input polarizer and analyzer as previous discussed (see Table 2.3 in Section 2.6.5). A quick overview of the

linear polarization cases, used to image the samples used for the studies discussed in the later parts of this chapter, and their practical significance for polarization microscopy of biological tissues is contained in the preceding Table 4.2.

Table 4.2: An overview of the standard linear polarization cases and their practical significance for polarization microscopy. Here the polarization symbols are defined as H=horizontal, V=vertical, M=minus 45°, and P=plus 45°.

CASE	PRACTICAL SIGNIFICANCE
HH,VV PP,MM	These aligned, parallel (par), polarization images detect light that has retained its polarization. Typically, these images alone do not contain much information about the polarization properties of the sample because the sample information contained is swamped by the huge contribution from the specular, surface glare, reflection, which retains the original incident polarization state.
HM,HP VM,VP PH,PV MH,MV	These ± 45° polarization images detect some light that has changed its polarization orientation, but also contains a huge background component from the majority that has not. In biological tissues the net birefringence and optical rotation effects are typically not large enough to provide much information in any of these images alone.
HV,VH PM,MP	These crossed, perpendicular (per), polarization images only detect light that has changed its polarization orientation, and thus, singularly supply the most information about sample birefringence or optical activity: provided that the combination picked most greatly highlights the samples axial asymmetries.

4.3.2.2 *Investigated Algorithms for Enhancing the Polarization Contrast of a Sample*

An algorithm that is applied to enhance polarization contrast works by highlighting the sample anisotropies by the process of cleaning up the image and eliminating the contributions of non-anisotropic structures. Two algorithms were investigated for the purpose of enhancing the polarization contrast of *ex vivo* biological samples that were imaged and are later presented in Section 4.5.3.

The first algorithm investigated was the Mueller matrix, which has the inherent property of separating out the polarization anisotropies of a sample, albeit a non-depolarizing sample as required by the Mueller matrix formulations discussed in Section 2.6.7 and succinctly presented in Table 2.5. Because the samples that were investigated are known to be de-polarizing, there was not much expectation for attaining polarization contrast enhancement using this method. That notwithstanding, there were some rather insightful results attained for one of the samples that are presented in Section 4.4.3. The second algorithm investigated is one that is known to be effective in filtering out light reflected by non-birefringent and non-polarization active structures by employing several polarization images. The algorithm, which is presented in Eqn 4.1, is based on a ratio involving the aligned and crossed polarization images

$$I_{H,V} = \frac{|HH - VH|}{HH + VH} = \frac{|VV - HV|}{VV + HV}$$
$$I_{P,M} = \frac{|PP - MP|}{PP + MP} = \frac{|MM - PM|}{MM + PM} \tag{4.1}$$

Where: H=Horizontal polarization; V=Vertical polarization; P=Plus 45° polarization; M=Minus 45° polarization.

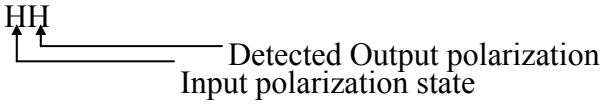

The ratio-metric method, described by Eqn. 4.1 has proven to be very effective in removing the effects of surface glare from tissue images. The results using this method are also presented in Section 4.4.3.

The following two examples serve to illustrate how the ratio-metric method described by Eqn. 4.1 works to enhance the sample polarization contrast. In Figure 4.2, an incident horizontally polarized light beam is changed to an elliptical SOP. From Section 2.6.3, recalling that the detected intensity is proportional to the square of the electric field, this implies that the relative intensity components in Figure 4.2 can be computed by:

$$HH = \frac{E_{ox}{}^2}{E_{ox}{}^2 + E_{oy}{}^2} = \frac{15^2}{15^2 + 3^2} = 0.962$$

$$HV = \frac{E_{oy}{}^2}{E_{ox}{}^2 + E_{oy}{}^2} = \frac{3^2}{15^2 + 3^2} = 0.038$$

and implementing these values into the ratio yields the result $I_{H,V} = 0.924$. This really means that the polarization anisotropy responsible for the ellipticity illustrated in Figure 4.2 is (1-0.924) = 0.076: a 7.6% linear polarization anisotropy.

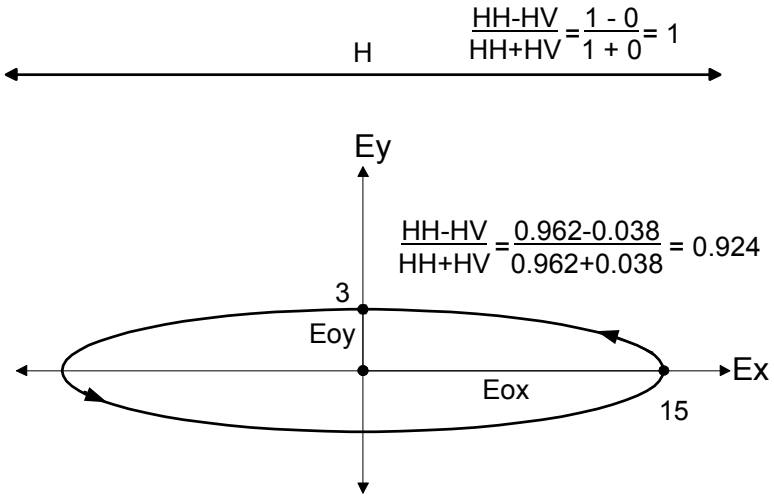

Figure 4.2: The effect of sample birefringence in creating an elliptical SOP and the polarization contrast enhancement obtained using the ratio-metric method described in Eqn. 4.1.

In Figure 4.3, an incident horizontally polarized light beam is rotated azimuthally but still retains its SOP. Again, from Section 2.6.3, the relative detected intensities can be computed by:

$$HH = \frac{E_{ox}{}^2}{E_{ox}{}^2 + E_{oy}{}^2} = \frac{15^2}{15^2 + 3^2} = 0.962$$

$$HV = \frac{E_{oy}{}^2}{E_{ox}{}^2 + E_{oy}{}^2} = \frac{3^2}{15^2 + 3^2} = 0.038$$

and implementing these values into the ratio yields the result $I_{H,V} = 0.924$. This really means that the polarization anisotropy responsible for the optical rotation, α, illustrated in Figure 4.3, is (1-0.924) = 0.076: a 7.6% linear polarization anisotropy. [x]

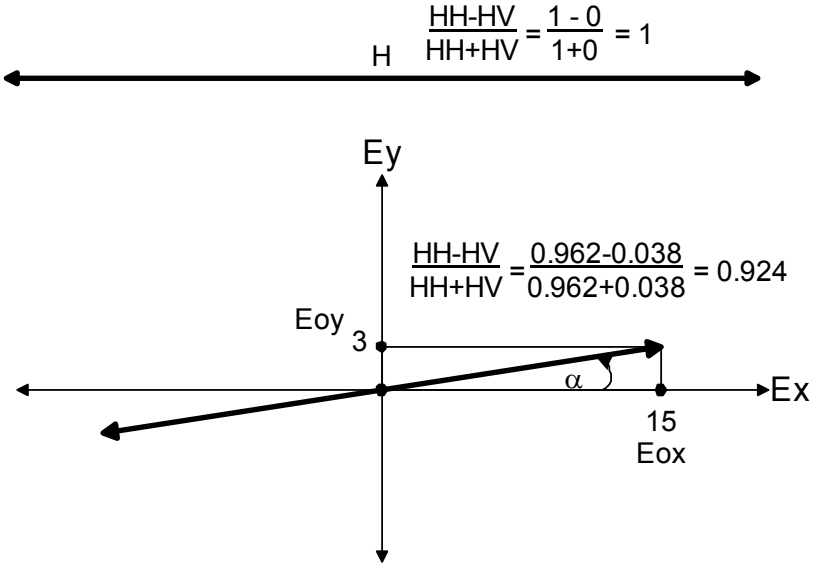

Figure 4.3: The effect of sample optical activity causing an azimuthal rotation of the plane of polarization by an amount α and the polarization contrast enhancement obtained using the ratio-metric method described in Eqn. 4.1.

4.4 Materials and Methods

4.4.1 *System Setup*

The experimental setup used for the backscattered-light-collection polarization imaging of a cardiac myocardium sample is illustrated in Figure 4.4. As depicted, a Leica DMLM microscope was modified to perform polarization microscopy by inserting two Leica custom-made, rotatable polarizers in the appropriate accessory slots, and installing a red

---

[x] Note that for the illustrations, I chose the values for the components E_{ox} and E_{oy} such that the polarization contrast enhancement would be the same; but in biological tissue, the effect of birefringence far outweighs that due to the effect of optical rotation because of the low concentrations for the pathlength of the tissue structure that the collected back-scattered light traverses.

650nm interference filter, 03 FIV 048, (Melles Griot, Carlsbad, CA). An Apogee KX260E (Apogee Instruments Inc., Auburn, CA), TE cooled 14 bit 509×510 pixel imaging area camera was mounted using a C-mount adapter camera attachment on the top of the microscope. The light extinction ratio of the system was limited by the dynamic range of the camera, with an average pixel intensity value of 104 for a dark field image and a 16348 value for a saturated image pixel. For analysis purposes, the image area was cropped to eliminate lines of dead pixels that were introduced by the optical system.

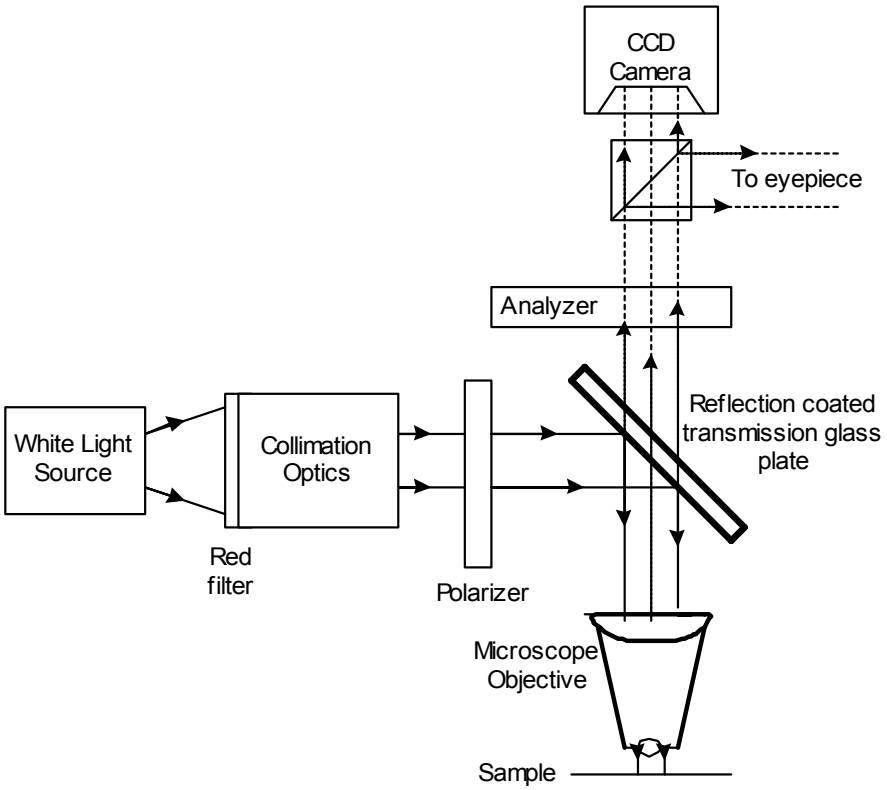

Figure 4.4: Block diagram of polarization microscope setup.

4.4.2 *System Calibration*

The system was calibrated using air and two known polarizer samples: a vertical and a horizontal axis sheet polarizer (Edmund Industrial Optics, Barrington, NJ).

4.4.3 *Sample Methods*

The septum from an excised rat heart was dissected, and treated with phosphate buffered formaldehyde to chemically fixate the structure. The unstained fixated sample was embedded in JB-4 plastic (Polysciences, Inc., Warrington, PA) for mechanical stabilization. The stabilized sample was centered in a rotatable optical mount and mounted on the microscope sample stage in a special adapter machined from Delron®. Sequences of polarization images were then taken of the sample, by rotating the polarizer and analyzer to the appropriate polarization setting. For this study, it was necessary to maintain a static sample in order to provide a reference for the calculation of the lamina divergence angle. As a result, the experimental plane was rotated but with an increment of 45-degrees due to the rotation limitation of the input polarizer. All possible input and output H, V, M, P combinations were investigated, 16 total, to determine which combination provided the best polarization contrast. The previously discussed ratio-metric method was investigated as a contrast enhancement technique. Each polarization case was imaged 5 times.

The second sample was a porcine lymphatic vessel cross-sectioned and treated with phosphate buffered formaldehyde to chemically fixate the structure. No mechanical stabilization was done for this sample, as such, the sample was placed on top of a glass slide that had the underside covered with a black paper and imaged without a cover slide.

4.5 Results and Discussion

4.5.1 *System Precision Results*

A set of ten consecutive bias frames were acquired to be used for bias correction. The mean of these ten images was applied as the correction for all subsequent images

acquired. Table 4.3 displays the results that show the reduction in the mean standard deviation for twenty-five consecutive images. The table also demonstrates the legitimacy of using 5 repetitions when collecting sample data; the lack of an improvement in using 5 images versus 25 means that the use of 5 images will not result in any considerable loss in signal-to-noise ratio (SNR).

After bias correction, the uniformity of the images was investigated. Figure 4.5 shows the irregularities in the pixel intensity values, for the case with maximum variation, i.e. HH case, and Table 4.4 contains results for all of the maximum intensity cases. These results demonstrate a lack of uniformity in the system illumination of the pixels for the different polarization combinations.

Table 4.3: Table indicating the improvement in average standard deviation of successive images due to the application of bias correction.

NON-BIAS CORRECTED				BIAS CORRECTED			
N	**Mean**	**Std**	**%Mean Deviation**	**N**	**Mean**	**Std**	**%Mean Deviation**
25	14460	109.5	0.631	25	13977	96.5	0.587
20	14457	113.2	0.667	20	13963	85.2	0.528
15	14466	106.3	0.583	15	13955	76.5	0.457
10	14472	118.9	0.678	10	13952	78.5	0.467
5	14500	124.6	0.631	5	13918	69.3	0.381
4	14505	143.2	0.731	4	13914	79.2	0.445
3	14484	166.9	0.875	3	13928	90.6	0.456
2	14579	39.1	0.190	2	13976	52.7	0.267
Average	**14490**	**115.2**	**0.623**	**Average**	**13948**	**78.6**	**0.449**

Table 4.4: Results for intensity variations across the image for the maximum intensity cases.

MEASUREMENTS

$$\begin{bmatrix} HH & HV & HM & HP \\ VH & VV & VM & VP \\ MV & MV & MM & MP \\ PV & PV & PM & PP \end{bmatrix}$$

MEAN VALUE [$\times 10^4$]

$$\begin{bmatrix} 1.2907 & 0.657 & 0.7377 & 0.7059 \\ 0.0654 & 0.8677 & 0.4292 & 0.4579 \\ 0.6677 & 0.4745 & 1.0859 & 0.0876 \\ 0.7184 & 0.4449 & 0.0966 & 1.076 \end{bmatrix}$$

STANDARD DEVIATION

$$\begin{bmatrix} 851.80 & 2.7888 & 473.9481 & 408.85 \\ 2.8917 & 615.32 & 294.08 & 292.66 \\ 410.585 & 316.420 & 717.473 & 19.860 \\ 428.754 & 300.259 & 23.125 & 684.12 \end{bmatrix}$$

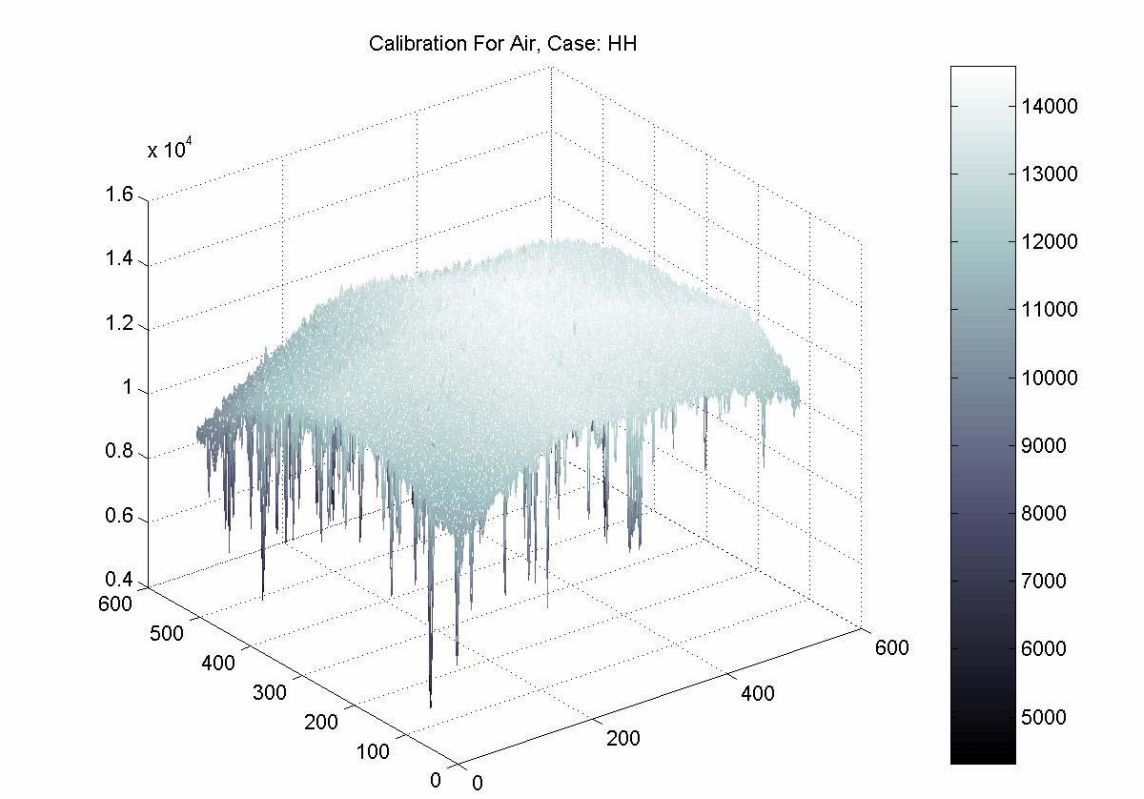

Figure 4.5: Mesh plot illustrating the lack of uniformity in the system illumination.

4.5.2 *System Polarization Calibration Results*

Though for this application, i.e. enhancing tissue features, quantification of optical parameters was not the goal; the polarization of the system was still calibrated using sheet polarizers, oriented at V and H, and air: via reflection off a silicon wafer, as the samples. The results in Table 4.5 show good agreement with theory with a maximum error of 22% for air and 5% for the polarizer samples. A careful analysis of the system did not reveal why the error for air was considerably larger. It is highly possible that the silicon wafer that was used as a reflecting surface for the backscattered light exhibited some polarization properties, therefore, accounting for the abnormally high values for the M_{12} and M_{21} values, which are indicators for polarizance and linear diattenuation based on Table 2.5.

Table 4.5: Polarization calibration results for the system.

SAMPLE	RESULTS	
	EXPERIMENTAL	THEORETICAL
AIR	$\begin{bmatrix} 1.0455 & -0.2184 & -0.0023 \\ -0.2178 & 1.0446 & -0.0401 \\ -0.0050 & 0.0316 & 1.0241 \end{bmatrix}$	$\begin{bmatrix} 1 & 0 & 0 \\ 0 & 1 & 0 \\ 0 & 0 & 1 \end{bmatrix}$
H-Polarizer	$\begin{bmatrix} 1.0000 & 0.9959 & 0.0329 \\ 0.9996 & 0.9954 & 0.0323 \\ 0.0500 & 0.0495 & 0.0235 \end{bmatrix}$	$\begin{bmatrix} 1 & 1 & 0 \\ 1 & 1 & 0 \\ 0 & 0 & 0 \end{bmatrix}$
V- Polarizer	$\begin{bmatrix} 1.0000 & -0.9971 & -0.0230 \\ -0.9998 & 0.9973 & 0.0231 \\ -0.0124 & 0.0121 & 0.0172 \end{bmatrix}$	$\begin{bmatrix} 1 & -1 & 0 \\ -1 & 1 & 0 \\ 0 & 0 & 0 \end{bmatrix}$

4.5.3 *Experimental Results*

Two sets of results are presented for this sample; without a red lens filter and with a red lens filter. When the two sets of results are compared, it is evident that there is considerable contrast enhancement utilizing the red lens filter. This makes sense for three reasons:

1. The tissue penetration depth is an inverse function of the wavelength of light. Recalling Eqn 2.35,

$$\mathbf{E}' = E_0' e^{-\kappa \cdot z} e^{i(k'z - \omega t)}$$

where κ is the corresponding wave propagation attenuation factor and applying to Eqn. 2.78 yields,

$$I \propto |E'|^2 = E_0'^2 e^{-2\kappa \cdot z}$$

which leads to Beers Law for the attenuation of a propagating EM wave along the z-axis:

$$I(x) = I_0 e^{-\alpha \cdot z}$$

where the wavelength dependence is given by $\alpha = \dfrac{4\pi\kappa}{\lambda}$ (reminiscent of Eqn 2.37)

and the penetration depth $l \cong \frac{1}{\alpha}$.

Therefore, as the wavelength increases, the penetration depth, *l*, increases because the attenuation coefficient α decreases in value.

For a white light source, the relative penetration depth can be roughly estimated based on the λ by ignoring the UV and IR portions of the emission spectra and using the median wavelength value for the visible spectrum. A more precise estimate involves using the weighted average of the complete light source emission spectra to find the mean wavelength and then using it to compute the tissue penetration depth based on the λ factor. Using the rough estimate, the relative difference in penetration depth for a halogen white light source with median λ=550[nm] and a red λ=650[nm] filtered light source is in the order of 0.1[μm]. Based on this alone, this implies that the filtered light contains more tissue information than the non-filtered light.

2. The narrower frequency range of the filtered light source produces a more defined higher resolution image, i.e. less blurred image, because there is less overlaying of information from differing depths due to the relatively significantly smaller number of constituent λ's, which each penetrate the tissue to varying depths, as established in explanation number 1, and contribute to the total intensity making up the image. In the case of the filtered light source, the λ's are essential all probing the same depth.
3. The reduction in the total number of λ's for the λ=650[nm] filtered case enables increasing the input light intensity to maximize the collection of output light that has equally and more deeply penetrated the tissue and, therefore, contains more sample information: i.e. this increases the system SNR.

4.5.3.1 *Rat Myocardium Results*

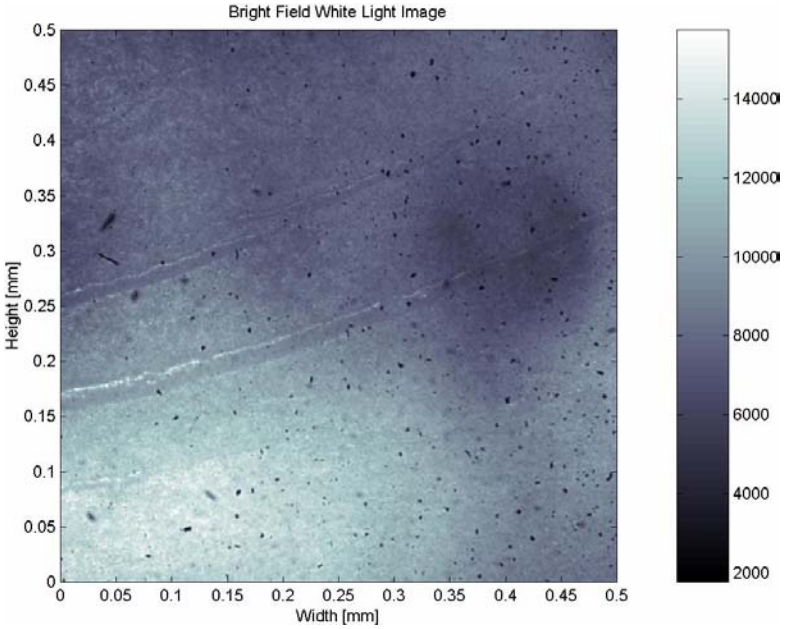

(a)

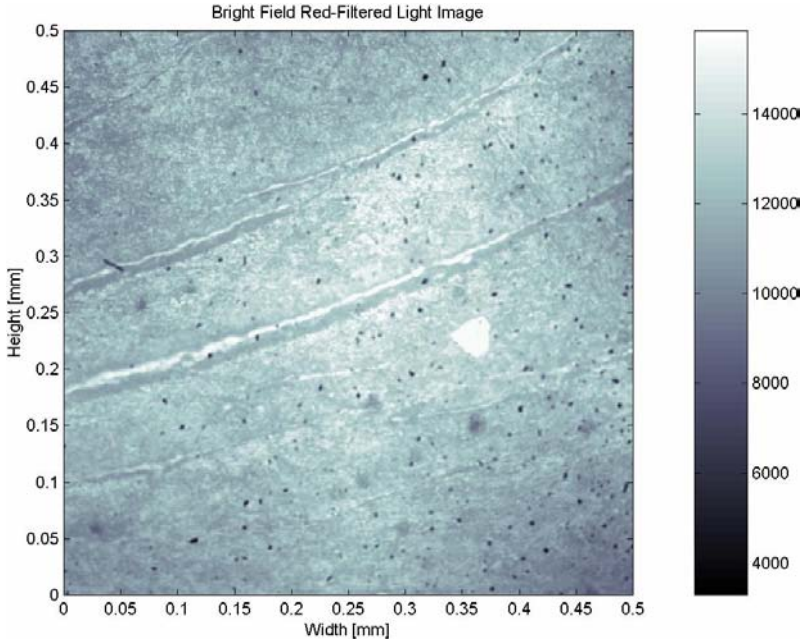

(a′)

Figure 4.6: Rat myocardium results; the non-primed and the primed cases represent the images collected without and with the red lens filter in the system respectively. (a)-(a′) Normal bright field images of rat myocardium showing the collagen lamina interface due to a large refractive index mismatch.

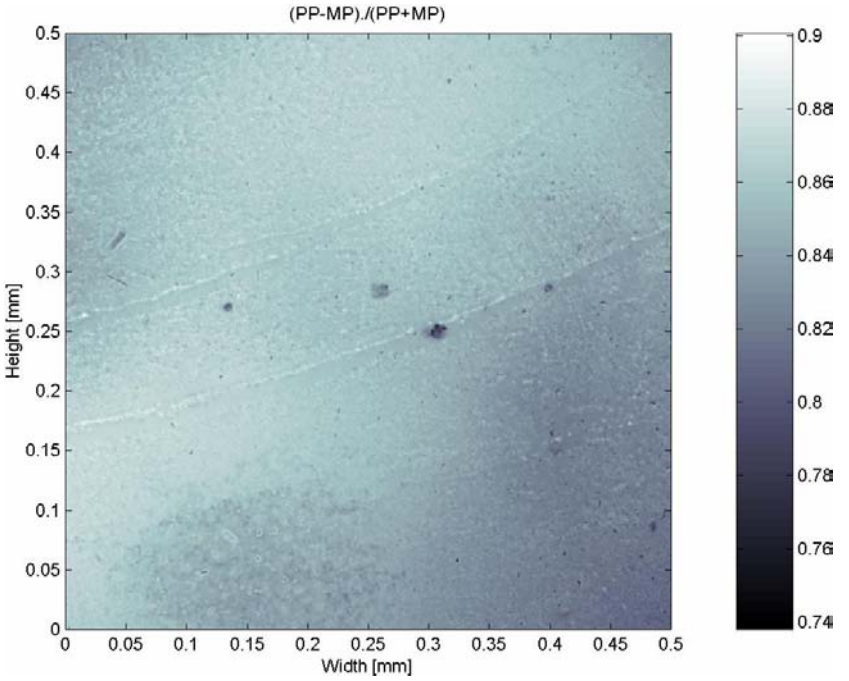

(b)

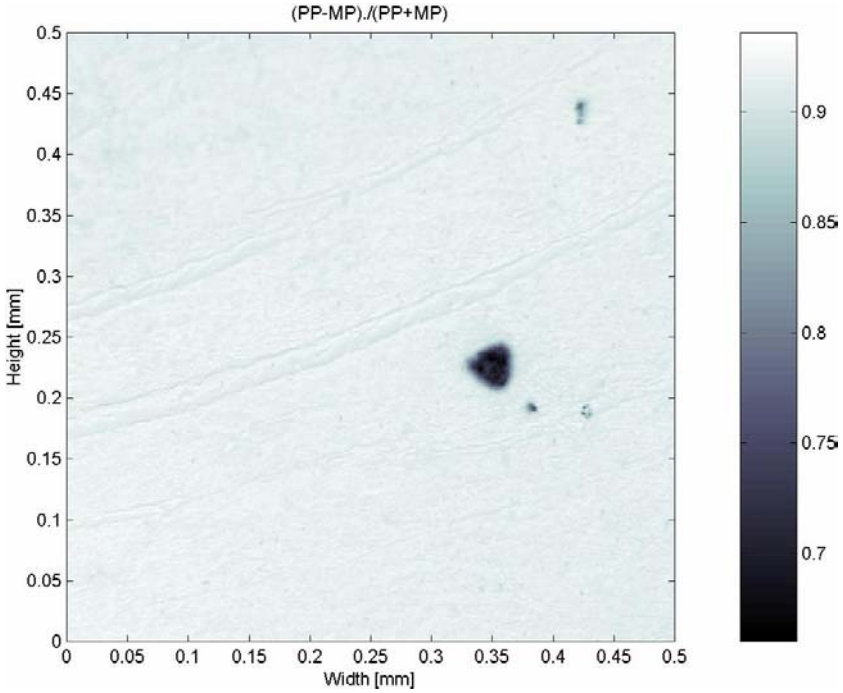

(b′)

Figure 4.6: Continued; (b)-(b′) are the linear anisotropy images based on Eqn. 4.1.

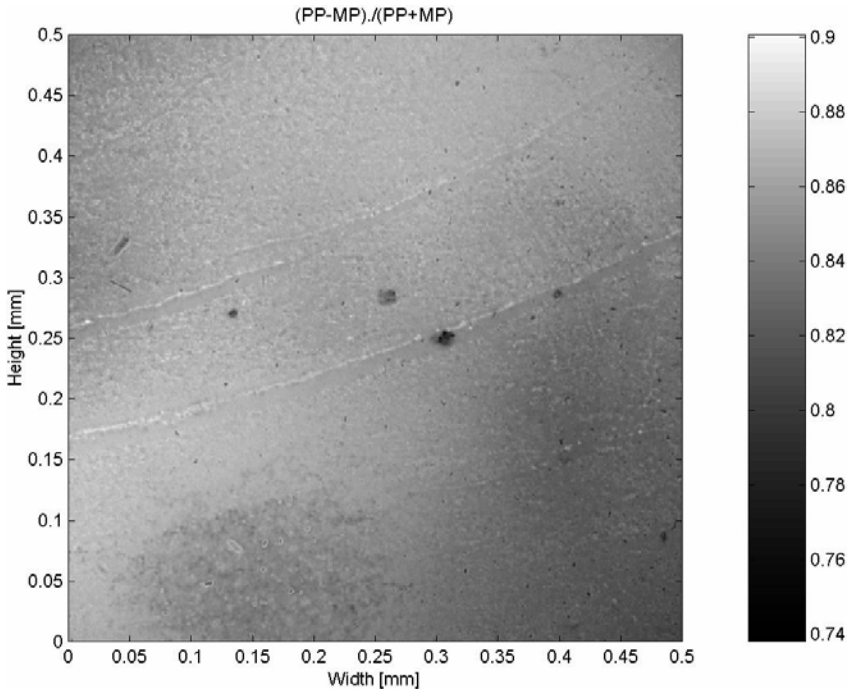

(c)

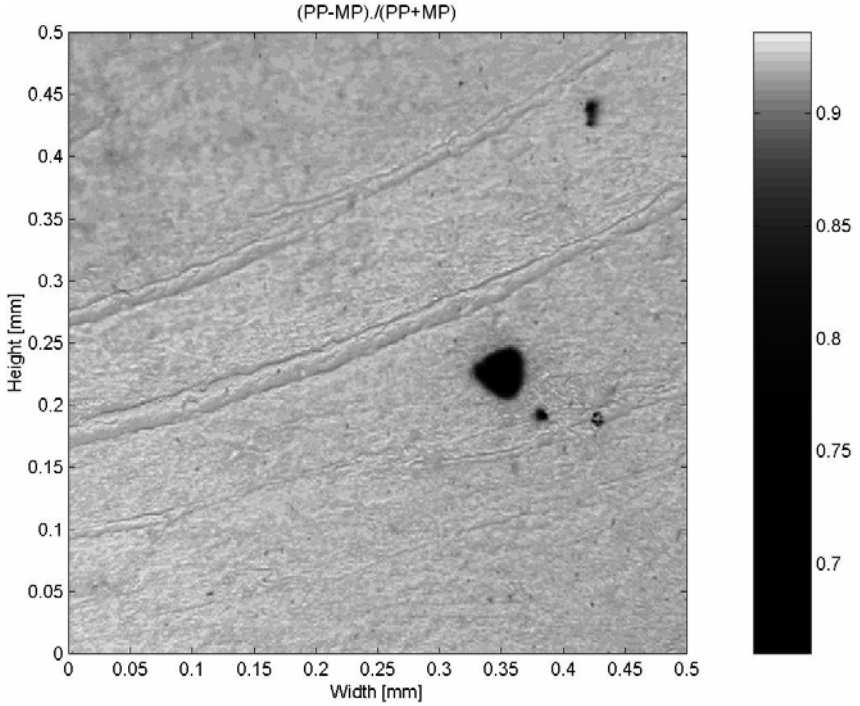

(c′)

Figure 4.6: Continued; (c)-(c′) are the software color contrast enhancements of images (b)-(b′) respectively.

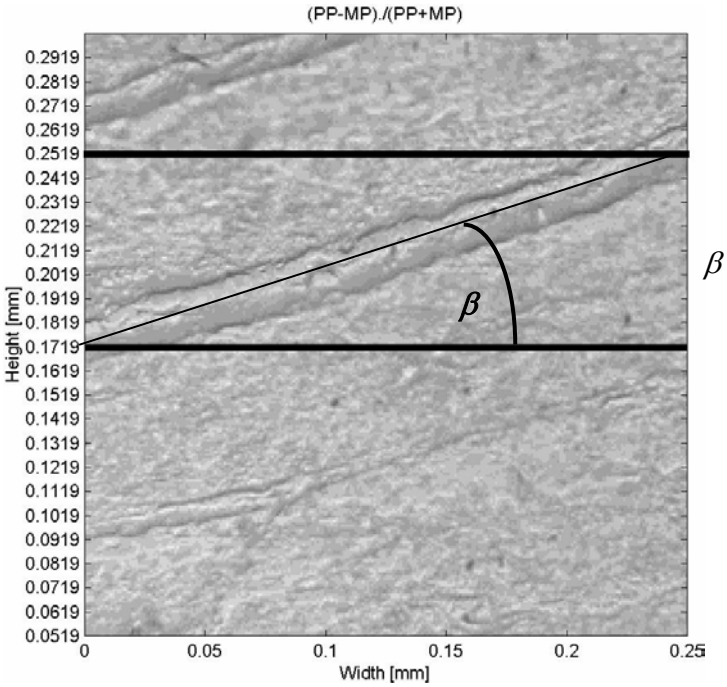

$$\beta = \tan^{-1}\left(\frac{0.2519 - 0.1719}{0.250}\right) = 17.74^{\circ}$$

(d)

Figure 4.6: Continued; (d) shows the method used to compute the myofiber sheet angle, *β*, of the cardiac cleavage planes.

The following discussion is based on the images in Figure 4.6, where the non-primed and the primed cases represent the images collected without and with the red lens filter respectively.

During the sample experiments, there was not much variation noticed in the individual polarization images other than the obvious refractive index mismatch at the cleavage planes, which were introduced by the plastic embedding process as the cleavage plane gaps were widened and filled with plastic, thus, accounting for the refractive index mismatch between the normal tissue and the plastic filling the spaces in between. Both (a)-(a′) images depict the aforementioned refractive index mismatch. A careful review of the polarization images later, revealed that they were very noisy as evidenced by the non-uniformities in the light illumination and the numerous black dots and spots evident in the (a)-(a′) images. Next, a Mueller matrix analysis was performed, which yielded nothing of

significance and is not presented because of the lack of significant contrast in the sample, as evidenced by the small color variations in the (a)-(a′) images.

Next an analysis of linear anisotropies was conducted using Eqns 4.1. This yielded some useful results presented below in images (b)-(b′) and (c)-(c′). The results show that by using the ratio-metric method, indeed surface glare and noise, dots in the images, were removed from the images. For the implementation of the system without a red lens filter, there is no enhancement of the contrast of the underlying structure as would be expected from the theory presented prior in the opening remarks of Section 4.5.3. However, it is apparent by comparing the set of images generated with the filter with those generated without the filter that there is a noticeable enhancement of the underlying tissue structure in the former images. Again this is expected from the aforementioned theory.

The (c)-(c′) images are the MATLAB® software color contrast enhancement images of the (b)-(b′) images respectively. These color contrast enhanced images are supposed to show more color variation in the ratio-metric generated linear anisotropy images. In the case of image (c), i.e. system with no red filter, there is no noticeable improvement in the color contrast as compared to the original image of (b). However, in the case of image (c′), i.e. system with red filter, there is a noticeable improvement in the color contrast as compared to the original image of (b′).

Finally, images (b)-(b′) and (c)-(c′) illustrate the usefulness of the linear anisotropic images, by eliminating system effects and reducing noise in the polarization contrast image, when compared to the normal bright field images (a)-(a′), which contain system noise, non-uniform illumination effects, and surface glare. The myofiber sheet angle, β, of the cardiac cleavage planes is calculated to be 17.74° based on Figure 4.6 (d) presented below which is an exploded view segment of image (c′).

4.5.3.2 *Pig Lymphatic Vessel Results*

Another Cardiovascular sample was imaged, this time a cross-section of a porcine lymphatic vessel. The goal was to enhance the features of the muscular wall, since muscle fibers are known to be optically active and birefringent, to enable a measurement of the wall thickness without having to resort to the usual staining and embedding procedures. The opaque hollow sample was placed on a glass slide that had a black paper cover placed underneath. The sample was imaged in backscatter mode using the setup described in Section 4.3.1 with the red interference filter installed and the results are presented in Figure 4.7.

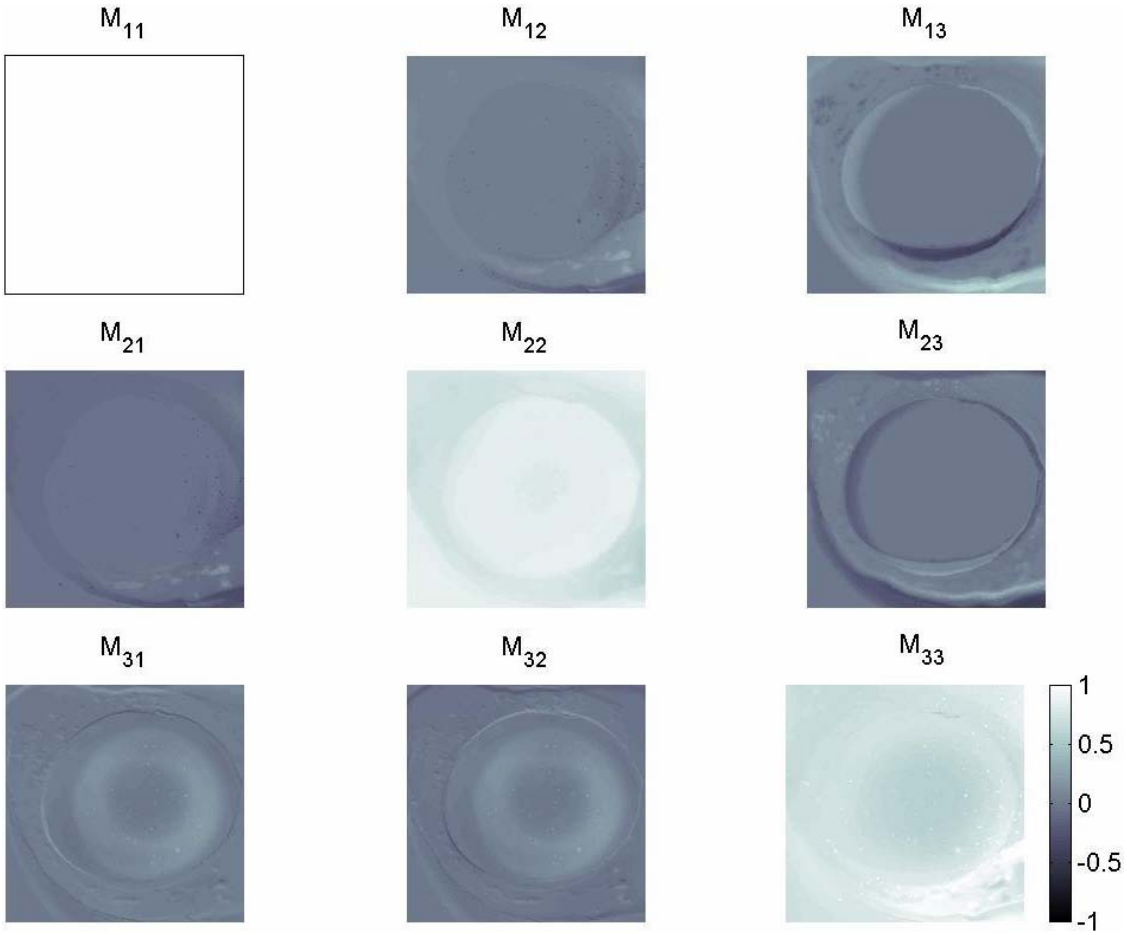

(a)

Figure 4.7: Porcine lymphatic vessel results acquired with a red filter installed in the system, where (a) is the 3×3 Mueller matrix of the vessel.

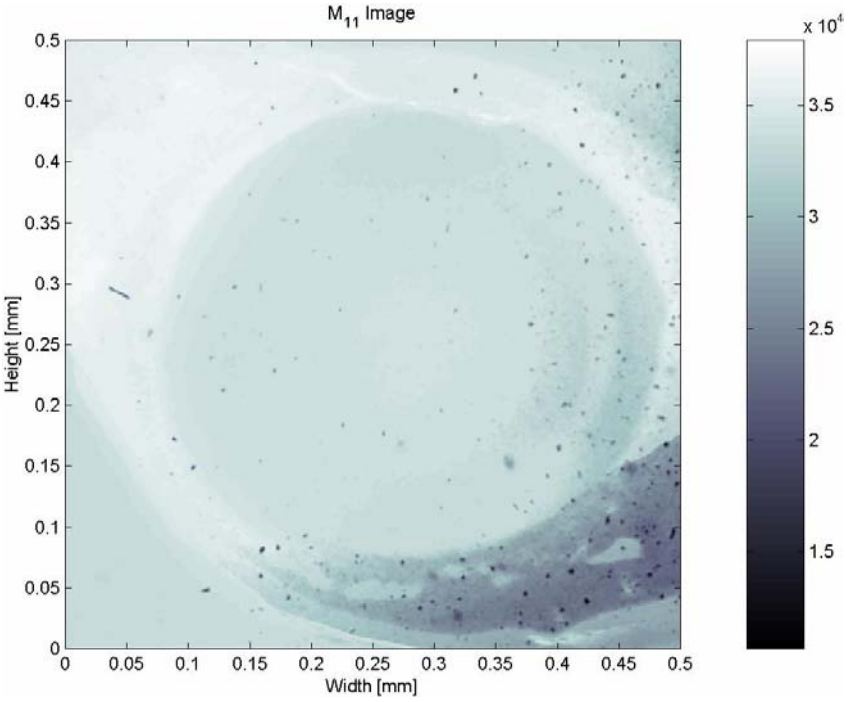

(b)

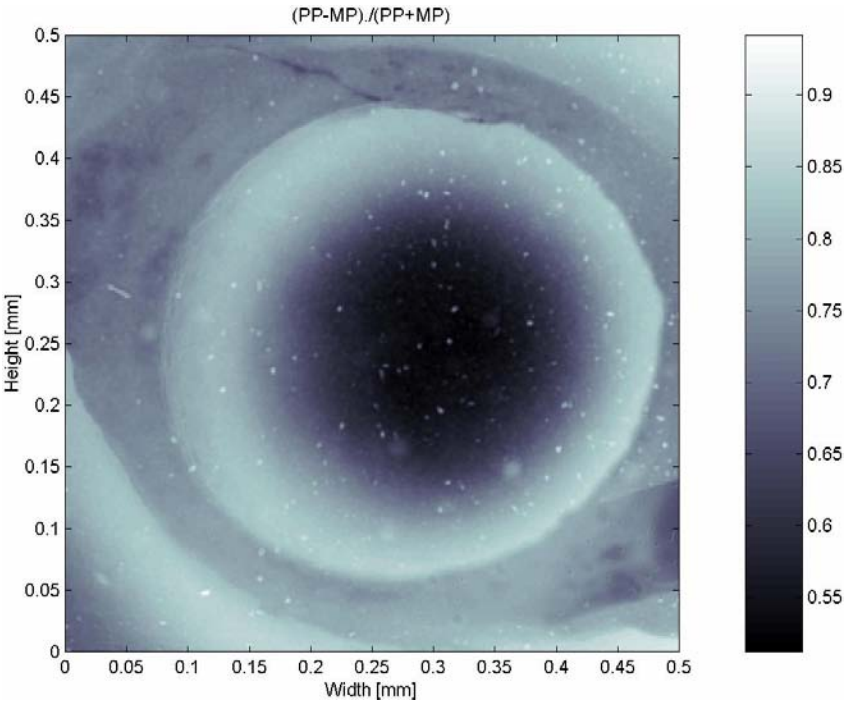

(c)

Figure 4.7: Continued; (b) is the M_{11} image from the Mueller matrix, (c) is the linear anisotropy image using PP and MP polarization images.

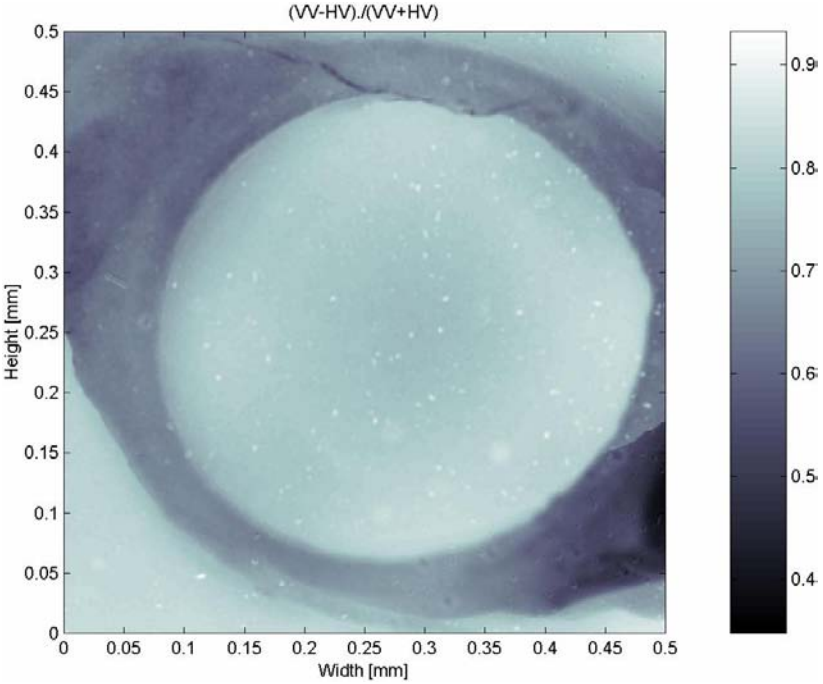

(d)

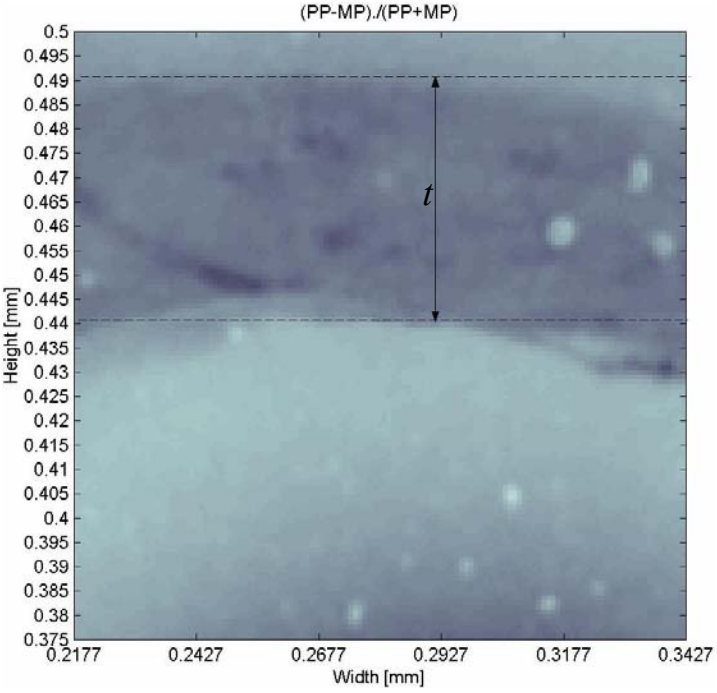

$t = 0.4905 - 0.4405 = 0.05[\text{mm}]$

(e)

Figure 4.7: Continued; (d) is the linear anisotropy image using MM and PM polarization images, (e) shows the method used to compute the thickness of the vessel muscular layer.

Figure 4.7 (a) is the normalized 3×3 sample Mueller matrix, normalized by dividing all of the elements by the M_{11} element. A look at the Mueller matrix indicates that the sample is expressing all of the 3×3 dielectric properties. Image (b) represents the bright field image, which is mostly fuzzy and does not clearly elucidate the vessel wall layers. On the other hand, the linear anisotropy images (c) and (d), which were derived using Eqn. 4.1, clearly reveal the muscular wall. These anisotropy images establish that Eqn 4.1 can also be applied to enhance the polarization contrast of the muscular wall and its features: the anchoring structure is visible in the right bottom edge of the vessel image in both (c) and (d). Image (e) is an exploded view segment from image (c) that is used to calculate the thickness of the vessel muscular layer, which is determined to be 0.05[mm].

4.6 Conclusion

Polarization microscopy combined with the right data analysis technique can be used to successfully determine the lamina divergence angles in myocardium by filtering out unwanted noise from the sample image, even without staining the sample. Likewise, it can be used for the contrast enhancement of protein and muscular structures, therefore, enabling biomechanical measurements without the need for caustic and sophisticated preparation and staining procedures. This finding has the potential to reduce the exposure risk of investigators to caustic chemicals and to further the work in the field of cardiac histology and biomechanics.

Future work includes implementing circular polarizers in the system to investigate other data analysis algorithms involving circularly polarized light. It is speculated, based on the retardance images of the rabbit cornea in the preceding chapter-known to be due to the birefringence of the collagen lamina that make up the cornea, that using the ratio-metric system to derive circular anisotropy images will generate images with greater polarization contrast than was achievable with the linear anisotropy images for the samples reported in this chapter.

CHAPTER V
SUMMARY

5.1 The Application of Polarized Light for Non-Invasive Glucose Detection

The work presented in Chapter III investigated the use of polarized light in the aqueous humor of the eye as a potential means of non-invasively quantifying blood glucose levels. In summary, it has been shown that the time lag between blood and aqueous humor glucose levels is within five minutes, and that a system can be built that has the sensitivity to measure the milli-degree rotations observed for physiologic glucose concentrations. The information that we have garnered from the ORD characterizations of the other primary chiral components in the aqueous humor of the eye has shown that their contributions are potentially negligible. But, if necessary, the prediction errors for glucose can be improved considerably if a multi-wavelength system is utilized. Finally, by modeling and characterizing the effect of changing birefringence on our glucose measurements *in vivo*, this information will enable us to design and implement a closed loop multi-wavelength system that we anticipate will facilitate the accurate and repeatable measurement of glucose *in vivo*. It will be a challenging feat based on the many variations evidenced by the coloration of the figures, which indicates an effect of relative birefringence changes that produce a retardation of greater than 60º, which when factored into Eqn. 3.7, is a considerable glucose measurement artifact.

The retardance and fast axis position are seen to vary significantly as you travel from the corneal apex (at the top) to the lens (at the bottom). In this direction, a light beam would be seen to traverse many retardation and fast axis isochores. From side to side, however, the variations observed are very minimal, as the isochores primarily follow the cornea contour. For glucose monitoring it may make sense to keep the beam within a reasonable contour area or perhaps try different light profiles such as a laser line instead of the typical circular beam. Furthermore, due to expected variations in corneal birefringence between eyeballs,[113] it may be necessary to have a calibration system that takes into account the unique optical properties of the eyeball that is utilized. This can

potentially be done by scanning in the spatial distribution of the corneal birefringence and fast axis location and building a complex calibration model or incorporating a simultaneous imaging system to record the path of the probing light beam through the eye and accounting for this in the glucose measurement. Once, a reasonable sample of human eyeball cornea birefringence and fast axis position data is accumulated, it is possible that the noted variations will necessitate a combination of all of the aforementioned ideas to ensure a robust sensor.

5.2 The Application of Polarized Light for Non-Staining Cardiovascular Histology

In Chapter IV, it was established that polarization microscopy combined with the right data analysis technique could be used to successfully determine the lamina divergence angles in myocardium by filtering out unwanted noise from the sample image, even without staining the sample. Likewise, it can also be used for the contrast enhancement of protein and muscular structures, therefore, enabling biomechanical measurements without the need for caustic and sophisticated preparation and staining procedures. This finding has the potential to reduce the exposure risk of investigators to caustic chemicals and to further the work in the field of cardiac histology and biomechanics.

Future work includes implementing circular polarizers in the system to investigate other data analysis algorithms involving circularly polarized light. It is speculated, based on the retardance images of the rabbit cornea in Chapter III- known to be due to the birefringence of the collagen lamina that make up the cornea, that using the ratio-metric system to derive circular anisotropy images will generate images with greater polarization contrast than was achievable with the linear anisotropy images for the samples reported in Chapter IV.

REFERENCES

[1] J. P. Bantle and W. Thomas, "Glucose measurement in patients with diabetes mellitus with dermal interstitial fluid," *J Lab Clin Med.* **130**(4), 436-441 (1997).

[2] B. D. Cameron, H. W. Gorde, B. Satheesan, and G. L. Cote, "The use of polarized laser light through the eye for non-invasive glucose monitoring," *Diabetes Technol Ther.* **1**(2), 135-143 (1999).

[3] P. G. Steffes, "Laser-based measurement of glucose in the ocular aqueous humor: an efficacious portal for determination of serum glucose levels," *Diabetes Technol Ther.* **1**(2), 129-133 (1999).

[4] M. S. Borchert, M. C. Storrie-Lombardi, and J. L. Lambert, "A non-invasive glucose monitor: preliminary results in rabbits," *Diabetes Technol Ther.* **1**(2), 145-151 (1999).

[5] J. J. Burmeister and M. A. Arnold, "Evaluation of measurement sites for noninvasive blood glucose sensing with near-infrared transmission spectroscopy," *Clin Chem.* **45**(9), 1621-1627 (1999).

[6] J. A. Tamada, S. Garg, L. Jovanovic, K. R. Pitzer, S. Fermi, and R. O. Potts, "Non-invasive glucose monitoring: comprehensive clinical results. Cygnus Research Team," *JAMA* **282**(19), 1839-1844 (1999).

[7] R. J. McNichols and G. L. Cote, "Optical glucose sensing in biological fluids: an overview," *J Biomed Opt*. **5**(1), 5-16 (2000).

[8] P. Zheng, C. E. Kramer, C. W. Barnes, J. R. Braig, and B. B. Sterling, "Non-invasive glucose determination by oscillating thermal gradient spectrometry," *Diabetes Technol Ther.* **2**(1), 17-25 (2000).

[9] C. Chou and P-K. Lin , "Noninvasive glucose monitoring with an optical heterodyne polarimeter," *Diabetes Technol Ther.* **2**, 45-47 (2000).

[10] L. Heinemann, U. Kramer, H. M. Klotzer, M. Hein, D. Volz, M. Hermann, T. Heise, and K. Rave, "Non-invasive glucose measurement by monitoring of scattering co-efficient during oral glucose tolerance tests. Non-invasive task force," *Diabetes Technol Ther.* **2**(2), 211-220 (2000).

[11] J. J. Burmeister, M. A. Arnold, and G. W. Small, "Non-invasive blood glucose measurement by near-infrared transmission spectroscopy across human tongues," *Diabetes Technol Ther.* **2**(1), 5-16 (2000).

[12] A. Samann, C. H. Fischbacher, K. U. Jagemann, K. Danzer, J. Schuler, L. Papenkordt, and U. A. Muller, "Non-invasive blood glucose monitoring by means of near infrared spectroscopy: investigation of long-term accuracy and stability," *Exp Clin Endocrinol Diabetes.* **108**(6), 406-413 (2000).

[13] G. L. Cote, "Non-invasive and minimally-invasive optical monitoring technologies," *J Nutr*. **131**(5), 1596S-1604S (2001).

[14] A. Gowda, R. J. McNichols, T. W. Fossum, S. Rastegar, and G. L. Cote, "Development of an implantable skin port sensor for use as an *in-vivo* optical glucose sensing platform," *Proc. SPIE*. **4263**, 11-19 (2001).

[15] S. E. Fineberg, R. M. Bergenstal, R. M. Bernstein, L. M. Laffel, and S. L. Schwartz, "Use of an automated device for alternative site blood glucose monitoring," *Diabetes Care* **24**(7), 1217-1220 (2001).

[16] B. D. Cameron, J. S. Baba, and G. L. Cote, "Measurement of the glucose transport time delay between the blood and aqueous humor of the eye for the eventual development of a non-invasive glucose sensor," *Diabetes Technol Ther.* **3**(2), 201-207 (2001).

[17] S. Bockle, L. Rovati, and R. R. Ansari, "Development of a novel non-invasive sensor for determination of blood glucose concentration," *Proc. SPIE* **4434** (abstract: 4624-24), 260-262 (2001).

[18] R. O. Potts, J. A. Tamada, and M. J. Tierney, "Glucose monitoring by reverse iontophoresis," *Diabetes Metab Res Rev.* **18**(Suppl. 1), S49-53 (2002).

[19] S. Bockle, L. Rovati, and R. R. Ansari, "Polarimetric glucose sensing using the Brewster-reflection off the eye lens: theoretical analysis," *Proc. SPIE* **4624**, 160-164 (2002).

[20] J. S. Baba, B. D. Cameron, S. Theru, and G. L. Cote, "Effect of temperature, pH, and corneal birefringence on polarimetric glucose monitoring in the eye." *J Biomed Opt.*

7(3), 321-328 (2002).

[21] C. D. Malchoff, K. Shoukri, J. I. Landau, and J. M. Buchert, "A novel non-invasive blood glucose monitor," *Diabetes Care* **25**(12), 2268-2275 (2002).

[22] S. J. Yeh, C. F. Hanna, and O. S. Khalil, "Monitoring blood glucose changes in cutaneous tissue by temperature-modulated localized reflectance measurements," *Clin Chem.* **49**(6), 924-934 (2003).

[23] R. A. White, D. Cavaye, and G. E. Kopchok, "Angioscopy in peripheral vascular disease: current status and future prospective," *Am J Card Imaging.* **7**(2), 92-98 (1993).

[24] B. Maisch, C. Bethge, L. Drude, G. Hufnagel, M. Herzum, and U. Schonian, "Pericardioscopy and epicardial biopsy--new diagnostic tools in pericardial and perimyocardial disease," *Eur Heart J.* **15**(Suppl C), 68-73 (1994).

[25] D. M. Cosgrove 3rd, J. F. Sabik, and J. L. Navia, "Minimally invasive valve operations," *Ann Thorac Surg.* **65**(6), 1535-1538 (1998).

[26] J. V. White, and I. Eid, "Diagnostic and interventional angioscopy," *Surg Clin North Am.* **78**(4), 539-559 (1998).

[27] F. T. Padberg Jr., "Endoscopic subfascial perforating vein ligation: its complementary role in the surgical management of chronic venous insufficiency," *Ann Vasc Surg.* **13**(3), 343-354 (1999).

[28] T. Clerici, and D. Sege, "Perforating veins and venous insufficiency," *Zentralbl Chir.* **124**(6), 525-529 (1999).

[29] W. R. Chitwood Jr, and L. W. Nifong, "Minimally invasive videoscopic mitral valve surgery: the current role of surgical robotics," *J Card Surg.* **15**(1), 61-75 (2000).

[30] R. Kolvenbach , "Hand-assisted laparoscopic abdominal aortic aneurysm repair," *Semin Laparosc Surg*. **8**(2), 168-177 (2001).

[31] P. M. Pego-Fernandes, F. Fernandes, B. M. Ianni, S. S. Rohr, I. M. Bernardelli, F. B. Jatene, and S. A. Oliveira, "Video-assisted pericardioscopy. How to improve diagnostic efficacy in pericardial effusions," *Arq Bras Cardiol*. **77**(5), 399-406 (2001).

[32] C. S. Thompson, V. G. Ramaiah, J. A. Rodriquez-Lopez, M. Vranic, R. Ravi, L.

DiMugno, S. Shafique, D. Olsen, and E. B. Diethrich., "Endoluminal stent graft repair of aortobronchial fistulas," *J Vasc Surg*. **35**(2), 387-391 (2002).

[33] Y. Mishra, M. Sharma, R. Bapna, R. Malhotra, Y. Mehta, K. K. Sharma, S. Shrivastava, and N. Trehan "Minimally invasive mitral valve surgery," *Indian Heart J.* **54**(3), 279-283 (2002).

[34] P. M. Seferovic, A. D. Ristic, R. Maksimovic, V. Tatic, M. Ostojic, and V. Kanjuh., "Diagnostic value of pericardial biopsy: improvement with extensive sampling enabled by pericardioscopy," *Circulation* **107**(7), 978-983 (2003).

[35] G. J. Toratora and S. R. Grabowski, *Principles of Anatomy and Physiology* 8th ed, HarperCollins College Publishers Inc., New York (1996).

[36] A. C. Guyton and J. E. Hall, *Textbook of Medical Physiology* 9th ed., W.B. Saunders Company, Philadelphia, PA (1996).

[37] L. V. Crowley, *Introduction to Human Diseases* 4th ed., Jones and Bartlett Publishers, Sudbury, MA (1997).

[38] National Institute of Diabetes and Kidney Diseases, "Prevalence of Diabetes," NIH Publication No. 02-3892, March (2002), http://www.niddk.nih.gov/health/diabetes/pubs/dmstats/dmstats.htm#7, accessed 06/27/2003.

[39] P. Hogan, T. Dall, and P. Nikolov, "Economic costs of diabetes in the US in 2002," *Diabetes Care*, **26**(3), 917-932 (2003).

[40] National Institute of Diabetes & Digestive & Kidney Diseases, "The diabetes control and complications trial," NIH Publication No. 02-3874**,** October (2001). http://www.niddk.nih.gov/health/diabetes/pubs/dcct1/dcct.htm, accessed 06/27/2003.

[41] American Diabetes Association, "Implications of the diabetes control and complications trial," *Diabetes Care*, **26**(Suppl 1): S25-27 (2003).

[42] B.E.R. Newlands, *Sugar*, Spon & Chamberlain, New York (1909).

[43] C. A. Browne and F. W. Zerban, *Physical and Chemical Methods of Sugar Analysis* 3rd ed., John Wiley & Sons, New York (1941).

[44] G. L. Spencer, *A Handbook for Cane-Sugar Manufacturers* 6th ed., John Wiley &

Sons, New York (1917).

[45] B. Rabinovitch, W. F. March, and R. L. Adams, "Noninvasive glucose monitoring of the aqueous humor of the eye: part I. Measurement of very small optical rotations," *Diabetes Care.* **5**(3), 254-258 (1982).

[46] W. F. March, B. Rabinovitch, and R. L. Adams, "Non-invasive glucose monitoring of the aqueous humor of the eye: part II. Animal studies and the Scleral lens," *Diabetes Care* **5**(3), 259-265 (1982).

[47] S. Pohjola, "The glucose content of aqueous humor in man," *Acta. Ophth*. **88**, 11-80 (1966).

[48] D. A. Gough, "The composition and optical rotatory dispersion of Bovine aqueous humor," *Diabetes Care* **5**, 266-270 (1982).

[49] G. L. Coté, M. D. Fox, and R. B. Northrop, "Non-invasive optical polarimetric glucose sensing using a true phase technique," *IEEE Trans. on Biomed. Eng.* **39**(7), 752-756 (1992).

[50] G. L. Coté, "Non-invasive optical glucose sensing-an overview," *J. Clin. Eng*. **22**(4), 253-259 (1997).

[51] D. C. Kloonoff, "Noninvasive blood glucose monitoring," *Diabetes Care* **20**(3), 433-437 (1997).

[52] M. J. Goetz, Jr., *Microdegree Polarimetry for Glucose Detection,* M.S. Thesis, University of Connecticut, Storrs, CT (1992).

[53] B. D. Cameron and G. L. Coté, "Non-invasive glucose sensing utilizing a digital closed-loop polarimetric approach," *IEEE Trans. Biomed. Eng.* **44**(12), 1221-1227 (1997).

[54] C. Chou, C. Y. Han, W. C. Kuo, Y. C. Huang, C. M. Feng, and J. C. Shyu, "Non-invasive glucose monitoring *in vivo* with an optical heterodyne polarimeter," *Appl Optics* **37**, 3553-3557 (1998).

[55] B. D. Cameron, H. W. Gorde, B. Satheesan, and G. L. Coté, "The use of polarized light through the eye for non-invasive glucose monitoring," *Diabetes Technol Ther.*, **1**(2), 135-143 (1999).

[56] S. Grossman and D. F. M. Brown, "Congestive heart failure and pulmonary edema," http://www.emedicine.com/emerg/topic108.htm, accessed 06/27/2003.

[57] L. Fletcher and D. Thomas, "Congestive heart failure: understanding the patho-physiology and management," *J Am Acad Nurse Pract*. **13**(6), 249-257 (2001).

[58] M. W. Rich, "Epidemiology, pathophysiology, and etiology of congestive heart failure in older adults," *J Am Geriatr Soc.* **45**(8), 968-974 (1997).

[59] American Heart Association, *Heart Disease and Stroke Statistics — 2003 Update*, American Heart Association, Dallas, TX (2002). http://216.185.112.5/downloadable/heart/10461207852142003HDSStatsBook.pdf, accessed 06/27/2003.

[60] C. A. Polanczyk, L. E. P. Rohde, G. W. Dec, and T. DiSalvo, "Ten-year trends in hospital care for congestive heart failure," *Archives of Internal Medicine* **160**, 325-332 (2000).

[61] A. B. Kravitz, R. Bolli, and V. J. Ferrans, "Early degradation of collagen after acute myocardial infarction in the rat," *Am. J. Cardiol*. **52**, 390-395 (1983).

[62] M. Zhao, H. Zhang, T. F. Robinson, S. M. Factor, E. H. Sonnenblick, and C. Eng. "Profound structural alterations of the extracellular collagen matrix in postischemic dysfunctional("stunned") but viable myocardium," *J. Am. Coll. Cardio.* **10**, 1322-1334 (1987).

[63] G. Olivetti, J.M. Capasso, E.H. Sonnenblick, and P. Anversa, "Side-to-side slippage of myocytes participates in ventricular wall remodeling actutely after myocardial infarction in rats," *Cir. Res*. **67**, 23-34 (1990).

[64] L. C. U. Junqueira, G. Bignolas, and R. R. Brentani, "Picrosirius staining plus polarization microscopy, aspecific method for collagen detection in tissue sections," *Histochem. J.* **11,** 447-455 (1979).

[65] P. Whittaker, R. A. Kloner, D. R. Boughner, and J. G. Pickering, "Quantitative assessment of myocardial collagen with picrosirius red staining and circularly polarized light," *Basic Res Cardiol.* **89**(5), 397-410 (1994).

[66] I. J. LeGrice, B. H. Smaill, L. Z. Chai, S. G. Edgar, J. B. Gavin, and P. J. Hunter,

"Laminar structure of the heart: ventricular myocyte arrangement and connective tissue architecture in the dog," *Am. J. Physiol*. **38,** H571-582 (1995).

[67] J. S. Janicki, "Myocardial collagen remodeling and left ventricular diastolic function," *Braz J Med Biol Res.* **25**(10), 975-982 (1992).

[68] K.T. Weber, Y. Sun, S. C. Tyagi, and M. J. Cleutjens, "Collagen network of the myocardium: function, structural remodeling and regulatory mechanisms," *J Mol Cell Cardiol.* **26**, 279-292 (1994).

[69] J. P. Cleutjens, M. J. Verluyten, J. F. Smiths, and M. J. Daemen, "Collagen remodeling after myocardial infarction in the rat heart," *Am J Pathol.* **147**(2), 325-338 (1995).

[70] S. Wei, L. T. Chow, I. O. Shum, L. Qin, and J. E. Sanderson, "Left and right ventricular collagen type I/III ratios and remodeling post-myocardial infarction," *J Card Fail.* **5**(2), 117-126 (1999).

[71] Y. Sun, J. Q. Zhang, J. Zhang, and S. Lamparter, "Cardiac remodeling by fibrous tissue after infarction in rats," *J Lab Clin Med.* **135**(4), 316-323 (2000).

[72] F. Yang, Y. H. Liu, X. P. Yang, J. Xu, A. Kapke, and O. A. Carretero, "Myocardial infarction and cardiac remodelling in mice," *Exp Physiol*. **87**(5), 547-555 (2002).

[73] J. C. Criscione, personal communication, Department of Biomedical Engineering, Texas A&M University, College Station, TX (2003).

[74] D. S. Kilger, J. W. Lewis, and C. E. Randall, *Polarized Light in Optics and Spectroscopy*, Academic Press, San Diego, CA (1990).

[75] G. R. Fowles, *Introduction to Modern Optics.* 2nd ed., Dover Publications, Inc., New York (1989).

[76] E. Charney, *Molecular Basis of Optical Activity*, John Wiley & Sons, New York (1979).

[77] D. J. Griffiths, *Introduction to Electrodynamics* 3rd ed., Prentice Hall, New Jersey (1999).

[78] E. Hecht, *Optics* 3rd ed.., Addison Wesley Longman, Inc., Reading, MA (1998).

[79] D. S. Eisenberg, et al., *Physical Chemistry*, Benjamin/Cummings Publishing

Company, Inc., Menlo Park, CA (1979).

[80] W. Kauzmann, *Quantum Chemistry*, Academic Press Inc., New York (1957).

[81] A. Yariv, *Quantum Electronics*, John Wiley and Sons, Inc., New York (1967).

[82] R. C. Jones, "A new calculus for the treatment of optical systems. VII. Properties of the N-matrices," *J. Opt. Soc. Am.* **38**(8), 671-685 (1948).

[83] R. A. Chipman, "Polarimetry," *Handbook of Optics* 2nd ed., M. Bass, ed., Optical Society of America, Washington, DC. (1995).

[84] H. P. Jensen, J. A. Schellman, and T. Troxell, "Modulation techniques in polarization spectroscopy," *Applied Spectroscopy* **32**(2), 192-200 (1978).

[85] J. Schellman and H. P. Jensen. Optical spectroscopy of oriented molecules. *Chem. Rev.* **87**, 1359-1399 (1986).

[86] R. A. Chipman, "Polarization analysis of optical systems," *Optical Engineering* **28**(2), 90-99 (1989).

[87] D. Pye, *Polarised light in Science and Nature*, Institute of Physics Publishing, Philadelphia, PA (2001).

[88] T. T. Tower and R. T. Tranquillo, "Alignment Maps of Tissues: I. microscopic elliptical polarimetry," *Biophys J.* **81**(5), 2954-2963 (2001).

[89] W. A. Shurcliff, *Polarized Light: Production and Use*, Harvard University Press, Cambridge, MA (1962).

[90] W. A. Shurcliff and S. S. Ballard, *Polarized Light*, D. Van Nostrand Company, Inc, Princeton, NJ (1964).

[91] K. D. Möller, *Optics*, University Science Books, Mill Valley, CA (1988).

[92] T.W. King, G. L. Coté, R. J. McNichols, M. J. Goetz, "Multispectral polarimetric glucose detection using a single Pockels cell," *Opt Eng* **33**, 2746-2753 (1994).

[93] J. S. Baba, A. M. Meledeo, B. D. Cameron, and G. L. Coté, "Investigation of pH and temperature on optical rotatory dispersion for non-invasive glucose monitoring," *Proc. SPIE* **4263**, 25-33 (2001).

[94] A. Stanworth and E. J. Naylor, "The polarization optics of the isolated cornea," *Brit. J. Ophtha.*. **34**, 201-211 (1950).

[95] A. Stanworth and E. J. Naylor, "Polarized light studies of the cornea. I.," *J. Exp Biol.* **30**, 160-163 (1953).

[96] A. Stanworth and E. J. Naylor, "Polarized light studies of the cornea. II.," *J. Exp Biol.* **30**, 164-169 (1953).

[97] D. M. Maurice, "The structure and transparency of the cornea," *J. Physiol*. **136**, 263-286 (1957).

[98] D. Kaplan and F. A. Bettelheim, "On the birefringence of Bovine cornea," *Exp. Eye Res.* **13**, 219-226 (1972).

[99] L. J. Bour and N. J. L. Cardozo, "On the birefringence of the living human eye," *Vision Research* **21**, 1413-1421 (1981).

[100] G. J. van Blokland and S. C. Verhelst, "Corneal polarization in the living human eye explained with a biaxial model," *J. Opt. Soc. Am. A* **4**(1), 82-90 (1987).

[101] D. J. Donohue, B. J. Stoyanov, R. L. McCally, and R. A. Farrell, "Numerical modeling of the cornea's lamellar structure and birefringence properties," *J. Opt. Soc. Am. A* **12**, 1425-1438 (1995).

[102] W. A. Christens-Barry, W. J. Green, P. J. Connolly, R. A. Farrell, and R. L. McCally, "Spatial mapping of polarized light transmission in the central rabbit cornea," *Exp. Eye Res*. **62**, 651-662 (1996).

[103] D. J. Donohue, B. J. Stoyanov, R. L. McCally, and R. A. Farrell, "A numerical test of the normal incidence uniaxial model of corneal birefringence," *Cornea* **15**(3), 278-285 (1996).

[104] J. W. Jaronski, H. T. Kasprzak, and E. B. Jankowska-Kuchta, "Numerical and experimental study of the corneal birefringence," *Proc. SPIE* **3094**, 188-192 (1996).

[105] J. M. Bueno and P. Artal, "Double-pass imaging polarimetry in the human eye," *Optics Letters* **24**, 64-66 (1999).

[106] J. M. Bueno and F. Vargas-Martin, "Measurements of the corneal birefringence with a liquid-crystal imaging polariscope," *Appl Opt*. **41**(1), 116-124 (2002).

[107] R. W. Knighton and X. R.Huang, "Linear birefringence of the central human cornea," *Invest Ophthalmol Vis Sci.* **4**3(1), 82-86 (2002).

[108] J. Y. T. Wang and F. A. Bethtelheim, "Comparitive birefringence of cornea," *Comp. Biochem. Physiol.* **51**(1A), 89-94 (1975).

[109] J. M. Bueno and J. Jaronski, "Spatially resolved polarization properties for *in vitro* corneas," *Ophthalmic Physiol Opt.* **21**(5), 384-392 (2001).

[110] B. D. Cameron, *The Application of Polarized Light to Biomedical Diagnostics and Monitoring*, Ph.D. Dissertation, Texas A&M University, College Station, TX (2000).

[111] R. M. A. Azzam and N.M. Bashara, *Ellipsometry and Polarized Light*, Elsevier Science Publishers B.V., Amsterdam (1994).

[112] J. S. Baba, J. R. Chung, A. H. DeLaughter, B. D. Cameron, and G. L. Coté, "Development and calibration of an automated Mueller matrix polarization imaging system," *J Biomed Opt*. **7**(3), 341-349 (2002).

[113] J. W. Jaronski and H. T. Kasprzak, "Linear birefringence measurements of the *in vitro* human cornea," *Ophthalmic Physiol Opt.* **23**(4), 361-369 (2003).

[114] R. Oldenbourg and T. Ruiz, "Birefringence of macromolecules. Wiener's theory revisited, with applications to DNA and tobacco mosaic virus," *Biophys J.* **56**(1), 195-205 (1989).

[115] R. Arimoto and J. M. Murray., "Orientation-dependent visibility of long thin objects in polarization-based microscopy," *Biophys J.* **70**(6), 2969-2980 (1996).

[116] R. Oldenbourg, E. D. Salmon, and P. T. Tran, "Birefringence of single and bundled microtubules," *Biophys J.* **74**(1), 645-654 (1998).

[117] Z. Pantic-Tanner and D. Eden, "Calculation of protein form birefringence using the finite element method," *Biophys J.* **76**(6), 2943-2950 (1999).

[118] A. A. Young, I. J. Legrice, M. A. Young, and B. H. Smail, "Extended confocal microscopy of myocardial laminae and collagen network," *Journal of Microscopy* **192**(Pt 2), 139-150 (1998).

[119] Chemicon International, "Bouin's fluid (aqueous Bouin's fixative)," http://www.chemicon.com/techsupp/Bouin.asp, accessed 06/29/2003.

[120] L. C. Junqueria, J. Carneiro, and O. R. Kelley, *Basic Histology* 9th ed., Appleton & Lange, Stamford, CT (1998).

[121] US Department of Labor Occupational Safety & Health Administration, "Chemical sampling information: picric acid," http://www.osha.gov/dts/chemicalsampling/data/CH_263300.html, accessed 06/29/2003.

[122] US Department of Labor Occupational Safety & Health Administration, "Chemical sampling information: formaldehyde," http://www.osha.gov/dts/chemicalsampling/data/CH_242600.html, accessed 06/29/2003.

[123] US Department of Labor Occupational Safety & Health Administration, "Safety and health topics: acetic acid," http://www.osha.gov/dts/chemicalsampling/data/CH_216400.html, accessed 06/29/2003.

[124] US Department of Labor Occupational Safety & Health Administration, "Occupational safety and health standards for shipyard employment," Fed Register # 58: 35512 (07/01/1993). http://www.osha.gov/pls/oshaweb/owadisp.show_document?p_table=FEDERAL_REGISTER&p_id=13310&p_search_type=FEDERALTEXTPOLICY&p_search_str=formalin&p_text_version=FALSE#ctx1, accessed 06/29/2003.

[125] T.T. Tower and R.T. Tranquillo, "Alignment maps of tissues:II. Fast harmonic analysis for imaging, *Biophys J.* **81**(5), 2964-2971 (2001).

[126] J. R. Kuhn, Z. Wu, and M. Poenie, "Modulated polarization microscopy: a promising new approach to visualizing cytoskeletal dynamics in living cells," *Biophys J.* **8**0(2), 972-985 (2001).

[127] S. L. Jacques, J. R. Roman, and K. Lee, "Imaging superficial tissues with polarized light," *Lasers Surg Med.* **26**(2):119-129 (2000).

[128] S. L. Jacques, J. C. Ramella-Roman, and K. Lee, "Imaging skin pathology with polarized light," *J Biomed Opt*. **7**(3), 329-340 (2002).

[129] S. P. Morgan and I. M. Stockford, "Surface-reflection elimination in polarization imaging of superficial tissue," *Opt Lett.* **28**(2), 114-116 (2003).

APPENDIX I

ADDITIONAL SYSTEM CALIBRATION RESULTS

Table I-1a: Automated Mueller Matrix Polarization Imaging System (AMMPIS) sample characterization results. These results indicate post-calibration residual system polarization error.

SAMPLE	DEPOLARIZATION INDEX	POLARIZANCE	DIATTENUATION
AIR 10 reps	0.0304	0.0297	0.0090
H-Polarizer 3 reps	0.0245	0.9984	0.9647
V- Polarizer 3 reps	0.0028	0.9981	0.9977
P- Polarizer 3 reps	-0.0115	1.0124	1.0044
M- Polarizer 3 reps	-0.0076	0.9897	1.0289
QWP-V 3 reps	-0.0104	0.1195	0.0088

The theoretical values for a perfect physical realizable Mueller matrix generating system are presented in the following Table.

Table I-1b: Theoretical results for Automated Mueller Matrix Polarization Imaging System (AMMPIS) sample characterization results.

SAMPLE	DEPOLARIZATION INDEX	POLARIZANCE	DIATTENUATION
AIR	0.0000	0.0000	0.0000
H-Polarizer	0.0000	1.0000	1.0000
V- Polarizer	0.0000	1.0000	1.0000
P- Polarizer	0.0000	1.0000	1.0000
M- Polarizer	0.0000	1.0000	1.0000
QWP-V	0.0000	0.0000	0.0000

Table I-2: Calibration results: the standard deviation values for experimental values presented in Table 3.5

SAMPLE	STANDARD DEVIATION OF MATRIX VALUES
AIR 10 reps	$\begin{bmatrix} 0 & 0.0075 & 0.0034 & 0.0062 \\ 0.0076 & 0.0001 & 0.0060 & 0.0025 \\ 0.0050 & 0.0039 & 0.0097 & 0.0049 \\ 0.0040 & 0.0056 & 0.0043 & 0.0141 \end{bmatrix}$
H-Polarizer 3 reps	$\begin{bmatrix} 0 & 0.0006 & 0.0034 & 0.0072 \\ 0.0000 & 0.0006 & 0.0034 & 0.0072 \\ 0.0021 & 0.0022 & 0.0029 & 0.0036 \\ 0.0036 & 0.0036 & 0.0039 & 0.0077 \end{bmatrix}$
V- Polarizer 3 reps	$\begin{bmatrix} 0 & 0.0000 & 0.0013 & 0.0083 \\ 0.0000 & 0.0001 & 0.0014 & 0.0083 \\ 0.0037 & 0.0037 & 0.0046 & 0.0042 \\ 0.0045 & 0.0045 & 0.0012 & 0.0048 \end{bmatrix}$
P- Polarizer 3 reps	$\begin{bmatrix} 0 & 0.0039 & 0.0118 & 0.0055 \\ 0.0038 & 0.0063 & 0.0081 & 0.0019 \\ 0.0108 & 0.0068 & 0.0047 & 0.0060 \\ 0.0012 & 0.0034 & 0.0099 & 0.0017 \end{bmatrix}$
M- Polarizer 3 reps	$\begin{bmatrix} 0 & 0.0053 & 0.0092 & 0.0077 \\ 0.0029 & 0.0097 & 0.0012 & 0.0032 \\ 0.0041 & 0.0109 & 0.0106 & 0.0066 \\ 0.0029 & 0.0024 & 0.0072 & 0.0053 \end{bmatrix}$
QWP-V 3 reps	$\begin{bmatrix} 0 & 0.0060 & 0.0040 & 0.0060 \\ 0.0060 & 0.0000 & 0.0000 & 0.0060 \\ 0.0180 & 0.0090 & 0.0060 & 0.0060 \\ 0.0040 & 0.0050 & 0.0020 & 0.0020 \end{bmatrix}$

Table I-3: Testing analysis program: results for QWP ($\delta = \pi/2$) where ρ = fast axis location with respect to the horizontal x-axis.

Real ρ	Mueller Matrix	$\rho(M_{24})$	$\rho(M_{42})$	$\rho(M_{34})$	$\rho(M_{43})$
0° (H)	$\begin{bmatrix} 1 & 0 & 0 & 0 \\ 0 & 1 & 0 & 0 \\ 0 & 0 & 0 & 1 \\ 0 & 0 & -1 & 0 \end{bmatrix}$	0°	0°	0°	0°
45° (M)	$\begin{bmatrix} 1 & 0 & 0 & 0 \\ 0 & 0 & 0 & 1 \\ 0 & 0 & 1 & 0 \\ 0 & -1 & 0 & 0 \end{bmatrix}$	-45°	-45°	45°	45°
90° (V)	$\begin{bmatrix} 1 & 0 & 0 & 0 \\ 0 & 1 & 0 & 0 \\ 0 & 0 & 0 & -1 \\ 0 & 0 & 1 & 0 \end{bmatrix}$	0°	0°	90°	90°
135° (P)	$\begin{bmatrix} 1 & 0 & 0 & 0 \\ 0 & 0 & 0 & -1 \\ 0 & 0 & 1 & 0 \\ 0 & 1 & 0 & 0 \end{bmatrix}$	45°	45°	45°	45°
180° (H)	$\begin{bmatrix} 1 & 0 & 0 & 0 \\ 0 & 1 & 0 & 0 \\ 0 & 0 & 0 & 1 \\ 0 & 0 & -1 & 0 \end{bmatrix}$	0°	0°	0°	0°

APPENDIX II
NOMENCLATURE FOR THE MUELLER MATRIX OPTICAL DIELECTRIC PROPERTIES

EXTRACTING PHYSICAL PARAMETERS FROM THE MUELLER MATRIX

Clark Jones in his paper on "A New Calculus for the treatment of optical systems VII. Properties of N-Matrices," proposed that the dielectric properties of a thin non-depolarizing sample, contained in its matrix M, are a summation: line integral, of the 8 optical dielectric properties represented as homogeneous matrix elements, m, of equal infinitesimal thickness that are interchangeable in order. Consequently, each of these elements, m, represents a differential matrix element such that:

$$m = \begin{bmatrix} p & -(LD_0) & -(LD_{45}) & (CD) \\ -(LD_0) & p & (CB) & (LB_{45}) \\ -(LD_{45}) & -(CB) & p & -(LB_0) \\ (CD) & -(LB_{45}) & (LB_0) & p \end{bmatrix}$$

and

$$\mathrm{M} = e^{-m}.$$

Here M is the sample matrix and m is the differential matrix containing all of the dielectric properties of the sample. Applying the exponential Taylor series expansion for m<<1, which implies that all other terms greater than 1st order can be ignored, yields:

$$\mathrm{M} = 1 - m \Rightarrow \frac{d\mathrm{M}}{dm} = -1 \Rightarrow d\mathrm{M} = -dm\,.$$

Letting $d\mathrm{M} = \Delta M$ and $dm = m_i$, leads to

$$\mathrm{M} = \sum_{i=1}^{8} \int_0^z \Delta M = \sum_{i=1}^{8} m_i$$

where

$$m_i = \int_0^z \Delta M_i$$

represents the differential matrices that correspond to the 8 measurable optical dielectric properties of matter. These 8 differential matrices obtainable from the Mueller matrix of the sample, based on the Jones matrix requirement that the sample does not depolarize light, are summarized in the following table.

Table II-1: Summary of the Jones-Mueller matrix derivation for the 8 optical dielectric properties based on the requirement that the sample be non-depolarizing.

Measurable Dielectric Property (Symbol)	Differential Polarization Matrix [m_i]
Isotropic refraction	$m_1 = \begin{bmatrix} 0 & 0 & 0 & 0 \\ 0 & 0 & 0 & 0 \\ 0 & 0 & 0 & 0 \\ 0 & 0 & 0 & 0 \end{bmatrix}$
Isotropic absorption	$m_2 = \begin{bmatrix} p & 0 & 0 & 0 \\ 0 & p & 0 & 0 \\ 0 & 0 & p & 0 \\ 0 & 0 & 0 & p \end{bmatrix}$
Circular dichroism (CD)	$m_3 = \begin{bmatrix} 0 & 0 & 0 & (CD) \\ 0 & 0 & 0 & 0 \\ 0 & 0 & 0 & 0 \\ (CD) & 0 & 0 & 0 \end{bmatrix}$
Circular birefringence (CB)	$m_4 = \begin{bmatrix} 0 & 0 & 0 & 0 \\ 0 & 0 & (CB) & 0 \\ 0 & -(CB) & 0 & 0 \\ 0 & 0 & 0 & 0 \end{bmatrix}$
Linear dichroism $(LD)_0$	$m_5 = \begin{bmatrix} 0 & -(LD_0) & 0 & 0 \\ -(LD_0) & 0 & 0 & 0 \\ 0 & 0 & 0 & 0 \\ 0 & 0 & 0 & 0 \end{bmatrix}$
Linear dichroism $(LD)_{45}$	$m_6 = \begin{bmatrix} 0 & 0 & -(LD_{45}) & 0 \\ 0 & 0 & 0 & 0 \\ -(LD_{45}) & 0 & 0 & 0 \\ 0 & 0 & 0 & 0 \end{bmatrix}$
Linear birefringence $(LB)_0$	$m_7 = \begin{bmatrix} 0 & 0 & 0 & 0 \\ 0 & 0 & 0 & 0 \\ 0 & 0 & 0 & -(LB_0) \\ 0 & 0 & (LB_0) & 0 \end{bmatrix}$
Linear birefringence $(LB)_{45}$	$m_8 = \begin{bmatrix} 0 & 0 & 0 & 0 \\ 0 & 0 & 0 & (LB_{45}) \\ 0 & 0 & 0 & 0 \\ 0 & -(LB_{45}) & 0 & 0 \end{bmatrix}$

EXPLANATION OF Table II-1

1. Isotropic Refraction

As indicated in Table II-1, a sample that exhibits only pure isotropic refraction yields no measurable quantities in the Mueller matrix. Practically speaking, pure clear liquids are the media that demonstrate close to pure isotropic refraction even though they also absorb some of the light.

2. Isotropic Absorption

Again pure liquids and or homogeneous suspensions of isotropic particles demonstrate close to near pure isotropic absorption, thus, yielding the m_2 matrix:

$$\begin{bmatrix} p & 0 & 0 & 0 \\ 0 & p & 0 & 0 \\ 0 & 0 & p & 0 \\ 0 & 0 & 0 & p \end{bmatrix}$$

where p^2 is the transmittance, i.e. the M_{11} element of the Mueller matrix = I/I_0.[74]

I = measured output intensity, I_0 = input light intensity; an example of an isotropic absorber is pure water. All other matter exhibits absorption that can be determined from the following matrix for a non-isotropic absorber.

General Non-isotropic Absorbers

$$\frac{1}{2}\begin{bmatrix} p_1 + p_2 & \cos(2\theta)(p_1 - p_2) & 0 & 0 \\ \cos(2\theta)(p_1 - p_2) & \cos^2(2\theta)(p_1 + p_2) + 2\sin^2(2\theta)(p_1 p_2)^{1/2} & \cos(2\theta)\sin(2\theta)[p_1 + p_2 - 2(p_1 p_2)^{1/2}] & 0 \\ \sin(2\theta)(p_1 - p_2) & \cos(2\theta)\sin(2\theta)[p_1 + p_2 - 2(p_1 p_2)^{1/2}] & \sin^2(2\theta)(p_1 + p_2) + 2\cos^2(2\theta)(p_1 p_2)^{1/2} & 0 \\ 0 & 0 & 0 & 2(p_1 p_2)^{1/2} \end{bmatrix}$$

where p_1^2 is the maximum transmittance, p_2^2 is the minimum transmittance, and θ is the angle between the horizontal x-axis and the axis of p_1.

3. Circular Dichroism (CD)

Optically active samples exhibit the asymmetric absorption of Right and Left circularly polarized light, thus demonstrating a differential circular absorption coefficient as presented in Table 2.4, which yields the m_3 matrix.

4. Circular Birefringence (CB)

$$\begin{bmatrix} 1 & 0 & 0 & 0 \\ 0 & 1-2\sin^2(2\omega)\sin^2(\delta/2) & \sin(2\omega)\sin(\delta) & -\sin(4\omega)\sin(\delta/2) \\ 0 & -\sin(2\omega)\sin(\delta) & \cos(\delta) & \cos(2\omega)\sin\delta \\ 0 & -\sin(4\omega)\sin(\delta/2) & -\cos(2\omega)\sin\delta & 1-2\cos^2(2\omega)\sin^2(\delta/2) \end{bmatrix}$$

This represents the general matrix for a sample that exhibits circular birefringence, CB, e.g. a Right or Left Elliptical Retarder (REP or LEP),[74] where ρ is the azimuth angle of the fast eigenvector of the retarder, tan|ω| is the retarder ellipticity, and δ is the retardance $(\eta_R - \eta_L)$; here $\rho = 0°$ and $\delta = \pi$ for a REP or LEP. If tan|ω| = 1, i.e. $\omega = 45°$, you get a circular retarder for any given δ:

$$\begin{bmatrix} 1 & 0 & 0 & 0 \\ 0 & \cos(\delta) & \sin(\delta) & 0 \\ 0 & -\sin(\delta) & \cos(\delta) & 0 \\ 0 & 0 & 0 & 1 \end{bmatrix}$$

$RCR = \text{Right Circular Retarder}$

$$\begin{bmatrix} 1 & 0 & 0 & 0 \\ 0 & \cos(\delta) & -\sin(\delta) & 0 \\ 0 & \sin(\delta) & \cos(\delta) & 0 \\ 0 & 0 & 0 & 1 \end{bmatrix}$$

$LCR = \text{Left Circular Retarder}$

5,6. Linear Dichroism (LD)

The following represent the general matrices for samples that exhibit Linear Dichroism, LD,[74] where θ is the angle between the horizontal x-axis and the axis of maximum transmission, p_1^2 is the maximum transmittance, and p_2^2 is the minimum transmittance.

Case for $\theta = 0°$: Linear Dichroism (LD_H), yields:

$$\frac{1}{2}\begin{bmatrix} p_1+p_2 & p_1-p_2 & 0 & 0 \\ p_1-p_2 & p_1+p_2 & 0 & 0 \\ 0 & 0 & 2(p_1p_2)^{1/2} & 0 \\ 0 & 0 & 0 & 2(p_1p_2)^{1/2} \end{bmatrix}$$

Case for $\theta = 90°$: Linear Dichroism (LD_V), yields:

$$\frac{1}{2}\begin{bmatrix} p_1+p_2 & p_2-p_1 & 0 & 0 \\ p_2-p_1 & p_1+p_2 & 0 & 0 \\ 0 & 0 & 2(p_1p_2)^{1/2} & 0 \\ 0 & 0 & 0 & 2(p_1p_2)^{1/2} \end{bmatrix}$$

Case for $\theta = 45°$: Linear Dichroism (LD_P), yields:

$$\frac{1}{2}\begin{bmatrix} p_1+p_2 & 0 & p_1-p_2 & 0 \\ 0 & 2(p_1p_2)^{1/2} & 0 & 0 \\ p_1-p_2 & 0 & p_1+p_2 & 0 \\ 0 & 0 & 0 & 2(p_1p_2)^{1/2} \end{bmatrix}$$

Case for θ = -45°: Linear Dichroism (LD_M), yields

$$\frac{1}{2}\begin{bmatrix} p_1+p_2 & 0 & p_2-p_1 & 0 \\ 0 & 2(p_1p_2)^{1/2} & 0 & 0 \\ p_2-p_1 & 0 & p_1+p_2 & 0 \\ 0 & 0 & 0 & 2(p_1p_2)^{1/2} \end{bmatrix}$$

7,8. Linear Birefringence (LB)

$$\begin{bmatrix} 1 & 0 & 0 & 0 \\ 0 & \cos(4\rho)\sin^2(\delta/2)+\cos^2(\delta/2) & \sin(4\rho)\sin^2(\delta/2) & -\sin(2\rho)\sin\delta \\ 0 & \sin(4\rho)\sin^2(\delta/2) & -\cos(4\rho)\sin^2(\delta/2)+\cos^2(\delta/2) & \cos(2\rho)\sin\delta \\ 0 & \sin(2\rho)\sin\delta & -\cos(2\rho)\sin\delta & \cos(\delta) \end{bmatrix}$$

This represents the general matrix for a sample that exhibits Linear Birefringence, LB, e.g. a Linear Retarder,[74] where ρ is the fast axis location and δ is the retardance $(\eta_e - \eta_o)$. For an example $\delta = \pi/2$, for a QWP, results in the following matrix general matrix for any fast axis location, ρ:

$$\begin{bmatrix} 1 & 0 & 0 & 0 \\ 0 & \cos^2(2\rho) & \sin(2\rho)\cos(2\rho) & -\sin(2\rho) \\ 0 & \sin(2\rho)\cos(2\rho) & \sin^2(2\rho) & \cos(2\rho) \\ 0 & \sin(2\rho) & -\cos(2\rho) & 0 \end{bmatrix}$$

Furthermore, a QWP with a fast axis position of horizontal where $\rho = 0°$ yields:

Note: clean air is an example of a non-dichroic sample, i.e. $p_1 = p_2$, therefore, it yields the following Mueller matrix when the system is run with air as the sample,

$$\begin{bmatrix} 1 & 0 & 0 & 0 \\ 0 & 1 & 0 & 0 \\ 0 & 0 & 1 & 0 \\ 0 & 0 & 0 & 1 \end{bmatrix},$$

which is the Mueller matrix for an isotropic, non-absorbing, non-reflecting medium collected in transmission.

APPENDIX III
THE JONES AND STOKES VECTORS FOR STANDARD INPUT LIGHT POLARIZATION STATES

INPUT POLARIZATION	STOKES VECTOR	JONES VECTOR
Horizontal $\mathcal{Y}$-state	$\begin{bmatrix} 1 \\ 1 \\ 0 \\ 0 \end{bmatrix}$	$\begin{bmatrix} 1 \\ 0 \end{bmatrix}$
Vertical $\mathcal{Y}$-state	$\begin{bmatrix} 1 \\ -1 \\ 0 \\ 0 \end{bmatrix}$	$\begin{bmatrix} 0 \\ 1 \end{bmatrix}$
$\mathcal{Y}$-state at +45°	$\begin{bmatrix} 1 \\ 0 \\ 1 \\ 0 \end{bmatrix}$	$\frac{1}{\sqrt{2}}\begin{bmatrix} 1 \\ 1 \end{bmatrix}$
$\mathcal{Y}$-state at -45°	$\begin{bmatrix} 1 \\ 0 \\ -1 \\ 0 \end{bmatrix}$	$\frac{1}{\sqrt{2}}\begin{bmatrix} 1 \\ -1 \end{bmatrix}$
$\mathcal{R}$-state	$\begin{bmatrix} 1 \\ 0 \\ 0 \\ 1 \end{bmatrix}$	$\frac{1}{\sqrt{2}}\begin{bmatrix} 1 \\ -i \end{bmatrix}$
$\mathcal{L}$-state	$\begin{bmatrix} 1 \\ 0 \\ 0 \\ -1 \end{bmatrix}$	$\frac{1}{\sqrt{2}}\begin{bmatrix} 1 \\ i \end{bmatrix}$

APPENDIX IV
NOMENCLATURE FOR ABBREVIATED REFERENCE JOURNALS

JOURNAL ABBREVIATION	COMPLETE JOURNAL NAME
Acta. Ophth.	*Acta Ophthalmologica*
Am J Card Imaging.	*American Journal of Cardiac Imaging*
Am J Pathol.	*American Journal of Pathology*
Am. J. Cardiol.	*The American Journal of Cardiology*
Am. J. Physiol.	*The American Journal of Physiology*
Ann Thorac Surg.	*The Annuals of Thoracic Surgery*
Ann Vasc Surg.	*Annals of Vascular Surgery*
Appl Optics	*Applied Optics*
Arq Bras Cardiol.	*Arquivos Brasileiros de Cardiologia*
Basic Res Cardiol.	*Basic Research in Cardiology*
Biophys J.	*Biophysical Journal*
Braz J Med Biol Res.	*Brazilian Journal of Medical and Biological Research*
Brit. J. Ophtha..	*British Journal of Ophthalmology*
Cir Res.	*Circulation Research*
Clin Chem.	*Clinical Chemistry*
Comp. Biochem. Physiol.	*Comparative Biochemistry and Physiology*
Diabetes Metab Res Rev.	*Diabetes/Metabolism Research and Reviews*
Diabetes Technol Ther.	*Diabetes Technology & Therapeutics*
Eur Heart J.	*European Heart Journal*
Exp Clin Endocrinol Diabetes.	*Experimental and Clinical Endocrinology & Diabetes*
Exp Physiol.	*Experimental Physiology*
Exp. Eye Res.	*Experimental Eye Research*
Histochem. J.	*The Histochemical Journal*
IEEE Trans. on Biomed. Eng.	*IEEE Transactions on Bio-Medical Engineering*
Invest Ophthalmol Vis Sci.	*Investigative Ophthalmology & Visual Science*
J Nutr.	*The Journal of Nutrition*
J Am Acad Nurse Pract	*Journal of the American Academy of Nurse Practitioners*
J Am Geriatr Soc.	*Journal of the American Geriatrics Society*
J Biomed Opt.	*Journal of Biomedical Optics*
J Card Fail.	*Journal of Cardiac Failure*
J Card Surg	*Journal of Cardiac Surgery*
J Lab Clin Med.	*Journal of Laboratory and Clinical Medicine*

JOURNAL ABBREVIATION	COMPLETE JOURNAL NAME
J Mol Cell Cardiol	*Journal of Cellular and Molecular Cardiology*
J. Am. Coll. Cardio.	*Journal of the American College of Cardiology*
J. Clin. Eng.	*Journal of Clinical Engineering*
J. Exp Biol.	*The Journal of Experimental Biology*
J. Opt. Soc. Am. A	*Journal of the Optical Society of America*
JAMA	*The Journal of the American Medical Association*
Lasers Surg Med.	*Lasers in Surgery and Medicine*
Ophthalmic Physiol Opt.	*Ophthalmic & Physiological Optics : The Journal of the British College of Ophthalmic Opticians*
Proc. SPIE	*Proceedings of the International Society for Optical Engineering*
Semin Laparosc Surg.	*Seminars in Laparoscopic Surgery*
Surg Clin North Am.	*The Surgical Clinics of North America*
Zentralbl Chir.	*Zentralblatt fur Chirurgie*

APPENDIX V
SIMULATION CODE

CORNEAL BIREFRINGENCE SIMULATION CODE

```
%Written by Justin Baba in MATLAB® 5.3
clear all
%user inputs are the fast axis orientation of the cornea: of the
retarder; wavelength of light used

%%%%%%%%%%%%%%%%%%%%%%%%%%%%%%%%%%%%%%%%%%%%%%%%%%%%%%%%%%%%%%%%%%%%%%%%%%%%
%Creating User Interface
format short e;
prompt = {'Enter fast axis location [degrees]:','Enter wavelength of
             light [nm]; Example: For Red diode laser: 635',};
title  = 'Inputs for computing Changes in detected Intensity with
            sample birefringence';
lines = 1;
def   = {'5','635'};
answer = inputdlg(prompt,title,lines,def);
rho1=sscanf(answer{1},'%f'); %read rho1 as a double precision value
lambda1=sscanf(answer{2},'%f'); %read lambda1 as a double precision
value
%%%%%%%%%%%%%%%%%%%%%%%%%%%%%%%%%%%%%%%%%%%%%%%%%%%%%%%%%%%%%%%%%%%%%%%%%%%%

deltan1=0:1.2:5.8;%stepping through human corneal birefringence range
                  (based on literature values)
                  %(difference in the refractive indices(n1-n2)

for  s=1:1:length(deltan1);
lambda=lambda1*(10^-9);%converting wavelength to meters
deltan=deltan1(s)*(10^-4);%birefringence is of the order of 10^-4
lc=2*.407*(10^-3);% the thickness of the corneal layer of the rabbit
                    eye (multiplied by two as the light traverses the
                    cornea twice on either end of the eye
delta=(2*pi*lc*deltan)/lambda;%calculating the phase difference in
                              degrees
%delta=(delta*pi)/180;%converting the phase difference to radians
rho=(rho1*pi)/180;%converting azimuthal angle to radians

%%%%%%%%%%%%%%%%%%%%%%%%%%%%%%%%%%%%%%%%%%%%%%%%%%%%%%%%%%%%%%%%%%%%%%%%%%%%
%calculating the parameters for the calculation of the mueller matrix
 of the birefringent material (cornea)
c2=cos(2*rho);
s2=sin(2*rho);
c4=cos(4*rho);
s4=sin(4*rho);
c=cos(delta/2)*cos(delta/2);
d=sin(delta/2)*sin(delta/2);
e=cos(delta);
f=sin(delta);
%mueller matrix for the birefringent material (modeled as a linear
retarder)
mc=[1 0 0 0;0((c4*d)+c)(s4*d)(-s2*f);0(s4*d)(-(c4*d)+c)(c2*f);0(s2*f)
```

```
    -(c2*f) e];
%%%%%%%%%%%%%%%%%%%%%%%%%%%%%%%%%%%%%%%%%%%%%%%%%%%%%%%%%%%%%%%%%%%%%%%%%%%%

in=[1;1;0;0];%Input polarization state:Horizontal polarization
%in=[1;-1;0;0];%Input polarization state:Vertical polarization
%in=[1;0;1;0];%Input polarization state:+45 degree polarization
%in=[1;0;-1;0];%Input polarization state:-45 degree polarization

for alpha1=0:5:180; %step through input polarizer angles from o degrees
                    to n degrees in 5 degree increments
   alpha=alpha1*pi/180; % converting alpha to radians
   %Mueller matrix of the polarizer modeled as a rotator
   rotator=[1 0 0 0;0 cos(2*alpha) sin(2*alpha) 0;0 -sin(2*alpha)
            cos(2*alpha) 0;0 0 0 1];
   rotator1=[1 0 0 0;0 cos(2*alpha) -sin(2*alpha) 0;0 sin(2*alpha)
             cos(2*alpha) 0;0 0 0 1];
   input=rotator1*in;%calculating the stokes vector of the input light
   mueller=mc*input;%calculating the stokes vector of the light after
                    it passes through the birefringent media
   Eox=.5*rotator*[1 1 0 0;1 1 0 0;0 0 0 0;0 0 0 0]
   %Mueller matrix of the horizontal analyzer
   Eoy=.5*rotator*[1 -1 0 0;-1 1 0 0;0 0 0 0;0 0 0 0];
   %Mueller matrix of the vertical analyzer
   out_H=Eox*mueller;%Stokes vector of the output of the horizontal
                     analyzer
   out_V=Eoy*mueller;%Stokes vector of the output of the vertical
                     analyzer
   D_H=out_H(1,1);%extracting the intensity information(first element)
   D_V=out_V(1,1);%extracting the intensity information(first element)
   evalc(['D_H' num2str(alpha1) '=D_H']); %Saves D_H as a string with a
                                          suffix of alpha1
   evalc(['D_V' num2str(alpha1) '=D_V']);%Saves D_V as a string with a
                                         suffix of alpha1
   evalc(['alpha' num2str(alpha1) '=alpha']);%Saves alpha1 as a string
                                             with a suffix of alpha1
end;

%%%%%%%%%%%%%%%%%%%%%%%%%%%%%%%%%%%%%%%%%%%%%%%%%%%%%%%%%%%%%%%%%%%%%%%%%%%%
%Combining the results for each analyzer

H=[D_H0,D_H5,D_H10,D_H15,D_H20,D_H25,D_H30,D_H35,D_H40,D_H45,D_H50,D_H5
5,D_H60,D_H65,D_H70,D_H75,D_H80,D_H85,D_H90,D_H95,D_H100,D_H105,D_H110,
D_H115,D_H120,D_H125,D_H130,D_H135,D_H140,D_H145,D_H150,D_H155,D_H160,D
_H165,D_H170,D_H175,D_H180];
V=[D_V0,D_V5,D_V10,D_V15,D_V20,D_V25,D_V30,D_V35,D_V40,D_V45,D_V50,D_V5
5,D_V60,D_V65,D_V70,D_V75,D_V80,D_V85,D_V90,D_V95,D_V100,D_V105,D_V110,
D_V115,D_V120,D_V125,D_V130,D_V135,D_V140,D_V145,D_V150,D_V155,D_V160,D
_V165,D_V170,D_V175,D_V180];
B=[alpha0,alpha5,alpha10,alpha15,alpha20,alpha25,alpha30,alpha35,alpha4
0,alpha45,alpha50,alpha55,alpha60,alpha65,alpha70,alpha75,alpha80,alpha
85,alpha90,alpha95,alpha100,alpha105,alpha110,alpha115,alpha120,alpha12
5,alpha130,alpha135,alpha140,alpha145,alpha150,alpha155,alpha160,alpha1
65,alpha170,alpha175,alpha180];
%%%%%%%%%%%%%%%%%%%%%%%%%%%%%%%%%%%%%%%%%%%%%%%%%%%%%%%%%%%%%%%%%%%%%%%%%%%%
```

```
alpha1=0:5:180; %Redefining the angle of rotation for plotting purposes
figure(1)
hold on
%plot(alpha1,H,'b',alpha1,V,'r')
plotyy(alpha1,H,alpha1,V)%plot with two different y axes on either side

x=cos(B).*cos(B);%theoretical intensity for non-birefringent sample
                  based on Maulus's Law

figure(2)
hold on
%plot(x,H,'b',x,V,'r')
plotyy(x,H,x,V) %plot with two different y axes on either side

clear rho lambda deltan delta H V alpha alpha1 Eox Eoy mueller D_H D_V
      mc out_H out_V input rotator
end;
hold off
hold off

clear all
```

VITA

Justin Shekwoga Baba was born on October 26, 1971 in Jos, Plateau State, Nigeria. He completed all his primary and secondary education in Nigeria at Kent Academy, in Miango, and Baptist High School, in Jos, respectively. He arrived in the U.S. in August of 1990 to attend LeTourneau University, a private non-denominational Christian College located in Longview, Texas. He received his B.S. in aviation with a flight option in 1994 from LeTourneau University, and then worked in the field of aviation for two years before returning to school to fill in the deficiencies for his graduate school candidacy in biomedical engineering. In the process, he acquired an A.S. in Engineering from Kilgore College in 1998, and while there was inducted into the Phi Theta Kappa: the International Honor Society for the Two Year College, and awarded the International Distinguished Chapter Officer Award in 1998. He started graduate work in biomedical engineering at Texas A&M in the Fall of 1998, joined the Optical Biosensing Laboratory (OBSL) in June of 1999, and completed his course work for a M.S. in biomedical engineering in the Fall of 2000 upon which he transitioned directly into the Ph.D. course. He was selected as the Texas A&M University Dwight Look College of Engineering Wilson Graduate Fellow for 2000-2001 and placed First (Oral presentation, Life Sciences IV), in the Texas A&M Graduate Student Research Week 2002 Competition. While in the Department of Biomedical Engineering at Texas A&M University, he worked as a teaching assistant for undergraduate courses in bioinstrumentation and bio-signal processing and served as an assistant lecturer for the department teaching "Signal processing in Biomedical Engineering"(BMEN 309). While a member of OBSL, he served as a graduate and undergraduate mentor and conducted research focusing on a variety of optical sensing, imaging, and diagnostic areas including the development of optical polarization systems; fluorescence, Raman, and infrared absorption spectroscopy systems; digital imaging microscopy systems for cancer detection, fluidic flow, and bio-analyte sensing *in-vitro*, *in-vivo*, *ex-vivo*, and -*situ*. He is a current member of SPIE, IEEE, SBME, and OSA. His permanent address is 2909 Braeburn, Bryan, TX 77802.